Title

Spatial and Temporal Characterization of a Pulsed Inductively Coupled Plasma Etch Device with Argon/Oxygen Gas

Author

Qian, Yuchen

Publication Date

2024

Peer reviewed|Thesis/dissertation

UNIVERSITY OF CALIFORNIA

Los Angeles

Spatial and Temporal Characterization of a Pulsed Inductively Coupled Plasma Etch Device with Argon/Oxygen Gas

A dissertation submitted in partial satisfaction of the
requirements for the degree Doctor of Philosophy
in Physics

by

Yuchen Qian

2024

ABSTRACT OF THE THESIS

Spatial and Temporal Characterization of a Pulsed Inductively Coupled Plasma Etch Device with Argon/Oxygen Gas

by

Yuchen Qian
Doctor of Philosophy in Physics
University of California, Los Angeles, 2024
Professor Walter N. Gekelman, Chair

Low temperature radio frequency (RF) inductively coupled plasma (ICP) is widely used in semiconductor industry for surface etching and processing. The plasma needs to be highly controllable and uniform. Electronegative gases are often used for their high reactivity, which adds to the complexity. Various measurements were performed in an effort to characterize a pulsed ICP in an industrial etch tool driven by a 2 MHz planar coil, with improved temporal and spatial resolution from previous literature. The operating gas was Ar/O_2. The wafer on the bottom electrode can be biased at 1 MHz independently.

The decoupling of the driving RF and the bias RF enables separate control over the plasma parameters in the sheath and the bulk region. In the sheath region in contact with the wafer, laser induced fluoresence experiment was conducted. Ar ion angle and energy distributions, drift velocity and sheath dynamics were investigated for different cases of wafer bias. The results showed an instantaneous sheath motion in response to the wafer bias. The ion energy distribution showed a continuous tail extending close to the bias voltage when the bias was turned on during the plasma glow, and a bimodal shape with a high energy peak when the bias was turned on in the afterglow.

In the bulk region, RF compensated Langmuir probe, hairpin probe, Bdot probe and photodetachment were used to obtain essential plasma parameters. The electron

and negative ions spatial distribution showed significantly different structures in Ar and Ar/O_2. Different propagation patterns of the fields and inductive power deposition were also observed.

The dissertation of Yuchen Qian is approved.

Eduardo Paulo Jorge da Costa Alves

Troy A. Carter

Christoph Niemann

Walter N. Gekelman, Committee Chair

University of California, Los Angeles

2024

Contents

1 Introduction **1**

1.1 Fundamentals of Plasma Etch 1

1.2 Etch in Electronegative Plasma 5

1.3 Motivation and Outline 8

2 Laboratory Setup **10**

2.1 Plasma Chamber 10

2.2 Data Acquisition 13

2.3 Diagnostics 14

2.3.1 Langmuir Probe 14

2.3.2 Hairpin Probe 19

2.3.3 Magnetic Probe 22

2.3.4 Laser Diagnostics 24

2.3.5 Michelson Interferometer 25

3 Positive Ion Motion Above A Biased Wafer **31**

3.1 RF sheath near a biased surface 31

3.2 Laser Induced Fluorescence Method on Ar^+ 35

3.3 Experimental Setup 37

3.4 Data Acquisition and Image Processing 41

3.5 Results 42

3.5.1 Self-bias and Ion Energy 42

3.5.2 Sheath Variation 52

3.5.3 Bulk Drift and Ion Angles 55

4 Electrons and Negative Ions **63**

4.1 Electrons and Negative Ions 63

4.2 Measurement Techniques on Electronegativity 64

4.3 Experimental Setup 67

4.4 Results 69

5 Fields and Energy in Electronegative Plasma **75**

5.1 EM Field and Heating Mechanism in ICP 75

5.2 Power Absorption in Electronegative Plasma 78

5.3 Experimental Setup 79

5.4 Results 82

5.4.1 Field and Current 82

5.4.2 Inductive Power Deposition 88

6 Conclusion **97**

List of Figures

1 Schematics of plasma etching. Feature size are not drawn to true proportion. 2

2 Schematics of the plasma chamber. (a) Side view. (b) Top view. The semi-transparent blue rectangle shows the typical data collection plane that the probes scan through. The x and z axis is defined as the radial and axial axis of the cylinder, with the origin at the center of the wafer. . 10

3 Several cycles of the 1 MHz antenna current (orange, left axis) and voltage (blue, right axis), measured at the terminal of the coil. The power is 400 W. 11

4 Photos of the ICP chamber. (a) A side view of the ICP tool. The gas inlet is on the other side and not shown. (b) Details of the custom ball valve. (c) The 3-axis motor drive system. The tricolor arrows indicates the movement direction of each slide track (blue for in/out, green for sideways, red for up/down), and the stepper motor that motorizes each track is circled with the corresponding color. 12

5 An example workflow diagram of the Python based DAQ. 14

6 Idealized I-V curve. The current is plotted upside-down by convention. The ion saturation region is magnified 10 times for better visual effect. Figures from F. F. Chen [62]. 15

7 Equivalent circuit of the RF compensation Langmuir probe in RF plasma. 17

8 Impedance response of the RF compensation circuit. 18

9 Photo of a Langmuir probe tip with the compensation circuit and AC coupling ring, taken before epoxy was applied to cover the circuit board. 18

10 Magnitude of the transmitted power s-parameter S12 of the hairpin probe, obtained from a frequency scan on a vector network analyzer. The S12 magnitude is plotted on linear scale with arbitrary unit. 21

11 Schematic diagram of the hairpin probe circuit. 22

12 Probe tip of the three-axis 3.4 mm diameter Bdot probe, shielded with epoxy. Distance between the center of each loop is 5 mm 23

13 Block diagram of calibration setup for Bdot probe. 24

14 Spectrum of Sirah CSTR-D-532 dye laser obtained using a Fabry-Perot interferometer. The laser is tuned to the maximum efficiency for the dye mixture (Rhodamine 610 / 640 in methanol). From B. Jacobs' thesis [80]. 25
15 Photo of the homodyne Michelson interferometer. 26
16 Schematic of the Michelson interferometer setup. (a) The circuit diagram. (b) The input ramp voltage to the Gunn diode. (c) The mixer output, raw (blue) and Gaussian smoothed (orange). 29
17 Diagram of a biased electrode in ICP. The DC component (time-averaged value) of the potential inside the plasma is plotted on the right. The sizes of the sheath and the bulk are not plotted in scale. 32
18 Diagram of specie density in the sheath region near a biased electrode. From Lieberman and Lichtenberg [84]. 33
19 Diagram of the Ar^+ LIF scheme. Metastable state 0 is 19.2 eV above the ground state of the ion with the Ar ionization energy being 15.6 eV. In a plasma with $T_e = 4$ eV less than 3 % of the electrons are at this energy for multi-step ionization. This results in few ions in state 0 and weak resultant optical signals. 35
20 Diagram of the experimental setup illustrating the optical path. Here the beam is shown to enter the plasma chamber horizontally. A group of mirrors can be inserted in the beam path to make the beam enters vertically towards the wafer. 38
21 Side view of the plasma chamber (not to scale). The reader's perspective is the same as the fast camera's. The laser sheet can enter the chamber horizontally above the wafer, or vertically towards the wafer by placing two 45° mirrors in front of the horizontal beam. 38
22 Photo of the experimental setup (a) on the side of the incoming laser beam and (b) on the side of the camera. 39
23 Timing chart of the data acquisition during one plasma pulse, for case (1) and (3). 40

24 Detailed timing of case (3) in afterglow, showing the ICP coil voltage amplitude (red), peak-to-peak applied bias voltage (blue) and photodiode signal (green). 41
25 Sample images to show the image processing procedure. (a) The direct output from the CCD camera taken during the laser firing at 611.661 nm. (b) The background photo taken 200 ns after (a). (c) The post-processed image, obtained by subtracting pixel by pixel the 7(b) from that in 7(a) and applying a Butterworth filter and Gaussian smoothing over 5 pixels. 43
26 The equivalent circuit of a biased electrode and sheath in ICP. 45
27 The bias voltage measured on the wafer during the active glow for case (1) (solid orange), during the afterglow for case (3) (dashed dotted green), and the applied voltage (dashed blue). The wafer waveform practically corresponds to the sheath voltage. 46
28 Normalized IEDs of horizontal velocity (along the wafer), plotted on a logarithmic scale. The wafer was not biased. The semi-transparent blue rectangle indicates the noise level. 49
29 Normalized IEDs of vertical velocity (negative energy means downwards to the wafer), plotted on a logarithmic scale. The wafer was not biased. The semi-transparent blue rectangle indicates the noise level. 49
30 Normalized IEDs of vertical velocity plotted on a logarithmic scale. The wafer was biased at V_{pp} = -1200 V. LIF was taken at the most cathodic phase of the applied RF bias. The semi-transparent blue rectangle indicates the noise level. 50
31 The log of $f_V(E)$ as a function of height z, at x = 3.39 cm and V_{pp} = -1200 V. A yellow double arrow indicates the approximate sheath width. This data is taken at the phase of the RF bias when the applied RF voltage was most negative. 51
32 The log of $f_V(E)$ in afterglow as a function of height z,at x = 4.6 cm and V_{pp} = -1200 V. Normalized color bar is shown at left. 52

33 LIF signal at 611.6547 nm ($v_{ion} \approx c_B$) at 11 time steps, each 100 ns apart, covering one wafer bias cycle. t = 0 corresponds to the most cathodic phase of the applied bias. The top left panel shows the original photo, with a green box indicating the zoomed in field-of-view of the other panels. Arrows in panels t=0 and t=600 ns highlight the sheath thickness variation. 53

34 Sheath thickness as function of time (brown solid line) in one RF bias cycle from Figure 33. The applied bias voltage measured outside the chamber (blue dashed line) and the voltage on the wafer (green dashed line) are also plotted, with axis of values on the right. The red dots mark the instantaneous voltages when the laser fired. 54

35 $f_V(E)$ at z = 11.3 mm, zoomed in on the peak that has a blue shift of 2.3 eV. The wafer is biased at -1200 V. 56

36 Ar ion drifts near and at the edge of the wafer (x = 0 cm) when it is unbiased (a) and (b) with a -1200V bias. The ICP antenna is at high state. The drifts are in energy (eV). The largest arrows correspond to 6 eV in both cases. The position of the wafer is indicated by the grey rectangles at the bottom. 57

37 Ar ion drifts near and at the center of the wafer (x = 15 cm) when it is (a) unbiased and (b) with a -1000V bias. The ICP power is on high state. The drifts are in eV. The largest arrows correspond to 5 eV in both cases. Note the kilovolt ions in the sheath above the wafer are not included. . . 58

38 a) Ar ion drifts in the afterglow, (a) near the edge of the wafer (x = 0 cm) when it is unbiased, (b) at the center of the wafer (x = 15 cm) and with a -1200 V bias. The drifts are in eV. A small arrow on the side of each figure shows the magnitude of the largest drift. In (b) the ion drift near the wafer due to the wafer bias is included. 59

39 Contour map of downward (to the wafer) angles for ions as a function of x, the distance parallel to the wafer surface, a) for case (3) in the afterglow and b) for case (1). The wafer edge is at z = 0, x = 0. The angle displayed is respect to the normal to the wafer surface. 61

40 The cycle averaged (over 1 MHz) ion energy and angle distributions onto the wafer surface (z = 0 cm). (a) IEADs for pressures: 0.5, 1, and 5 mTorr. The plots are log-scaled over 3 decades. (b) IEDs, angle integrated from (a). From Qian et al [104]. 62

41 Photo of the equipment setup for photodetachment experiment. The beam path, shown as the dotted green arrows, goes across two room through a hole drilled on the wall. The reflective mirrors are circled in red. 68

42 Schematics of the ICP chamber and photodetachment experiment (not to scale). The laser beam enters from the left window and exit the right window to a beam dump. 69

43 Temporal evolution of electron density ($\times 10^{10}\mathrm{cm}^{-3}$) obtained by a hairpin probe at the onset of the pulse. 1(a-d): Ar; 2(a-d): 20% O_2 + 80% Ar; 3(a-d): 80% O_2 + 20% Ar. Row a-c are synchronized, and the timings are marked on the right. Row d is in quasi-steady state, which takes longer to reach in Ar. The timings for column 1, 2, 3 are t=1213 μs, 914 μs, 914 μs, respectively. Measurement is partly saturated in 1(a). 70

44 n_e as a function of z (top row) or r (bottom row), normalized to the maximum value on the trace. In clockwise direction: $n_e(z)$ at r = 0 cm (axial center), $n_e(z)$ at r = 18 cm (under the coil), $n_e(r)$ at z = 9 cm, $n_e(r)$ at z = 14 cm. 73

45 Electronegativity $\alpha_{-/e} = n_-/n_e$ in two ratios of gas. (a) Ar:O_2 = 8:2 (b) Ar:O_2 = 2:8. 74

46 Negative ion density ($\times 10^{9}\mathrm{cm}^{-3}$) calculated from measured n_e and $\alpha_{-/e}$, assuming quasi-neutrality. (a) Ar:O_2 = 8:2 (b) Ar:O_2 = 2:8. 74

47 (a) Electron-neutral collisional frequency and (b) mean free path as a function of electron temperature, at four different gas pressure. The driving frequency 2 MHz is highlighted in (a) as the black dashed line. Data is calculated from COP database. The plot is adapted from Han's thesis [60]. 80

48 Normalized magnitude of the induced magnetic field (a) as a function of radial position, at z = 15 cm (closest data acquisition point to the coil) (b) as a function of axial position, at r = 18 cm (under the coil). 84

49 Magnitude of the induced magnetic field in Ar (upper left), 20% O_2 (upper right) and 80% O_2 (lower left). The 2/e and 1/e contour lines are also plotted. 85

50 Induced J_θ (A/cm^2) during one RF cycle in quasi-steady state, in pure Ar (left) and 20% O_2 (right). RF phase proceeds from top (+0) to bottom (+2π). 86

51 Induced J_θ (A/cm^2) during one RF cycle in quasi-steady state, in 60% O_2 (left) and 80% O_2 (right). RF phase proceeds from top (+0) to bottom (+2π). 87

52 Time sequence of induced J_θ (color coded solid lines, left axis) during one RF cycles, summed over the whole data acquisition plane. The coil current synchronous to the probe measurement is plotted in black dashed line (right axis). 88

53 Averaged Power density (W/cm^3) over one RF cycle, (a) in pure argon plasma and (b) in pure oxygen plasma. 89

54 Electron temperature (eV) in Ar plasma (left) and O_2 plasma. 90

55 Time progression of instantaneous power density (W/cm^3) during half of an RF cycle, (a) in pure argon plasma and (b) in pure oxygen plasma. Note that the panels are chosen so that they cover the whole process of deposition. Due to the different phase lag in Ar and O_2, the panels in (a) and (b) are not synchronized. The timings of the panels are chosen for the best visual comparison. 91

56 Negative power absorption region in O_2, sampled at the phase where the effect is the most prominent. The positive power contour is also plotted for reference. 92
57 Power density in Ar plasma during one RF cycle (a) at different axial position and (b) at different radial position. In panel (a) the power density is averaged over all radial position for each axial position. Vice versa in panel (b). In both panels, t=0 corresponds to the maximum of coil current. 94
58 Power density in Ar plasma during one RF cycle (a) at different axial position (b) at different radial position. The plots were obtained similarly to Figure 57. 95
59 Power density in 80% Ar 20% O_2 plasma during one RF cycle at different radial position, averaged over z. 96

List of Tables

1 Typical operating conditions and parameters of plasma used in etching. . 2
2 Energy levels for the photodetachment experiment in oxygen plasma. . . 68

ACKNOWLEDGEMENTS

I would like to express my most sincere gratitude to:

My advisor Professor Walter Gekelman, who provided immense guidance and support in every way he could. His experience and motivation has inspired me to grow both as an experimentalist and as a person.

Dr. Patrick Pribyl, without whom this thesis would not have been possible. I received tremendous support in every aspect of my research work, and incredible knowledge that would surely benefit me for a long time to come.

Lam Research Corporation, for the valuable donation of lab equipment. I would also like to thank Alex Paterson for his great support and insightful comments on my work.

Tai Ly, Zoltan Lucky, Marvin Drandell, Avdit Kohli, and all the other staff and technicians at Basic Plasma Science Facility for their excellent technical support.

Professor Paulo Alves, who taught the graduate plasma courses in the most inspiring and helpful way and kindly agreed to serve on my committee.

Professors Troy Carter, for being an amazing resource of scientific insights, research support, good IPA and coffees, and serving on my committee.

Professor Christopher Niemann, for his kind support on my laser experiments and serving on my committee.

And last but not least, Professor Mark Kushner and Dr. Tugba Piskin from University of Michigan, Ann Arbor. It was my great honor and pleasure to collaborate with them.

CURRICULUM VITAE

2014 – 2018	B.S. in Physics, University of California, Los Angeles, CA.
2019 – 2024	Graduate student researcher, Department of Physics and Astronomy, University of California, Los Angeles, CA.

PUBLICATIONS

1. **Yuchen Qian**, Walter Gekelman, Patrick Pribyl, Tugba Piskin, Alex Paterson. "Ion motion above a biased wafer in a plasma etching reactor". Phys. Plasmas 31 (6), 063507 (2024)

2. Tugba Piskin, **Yuchen Qian**, Patrick Pribyl, Walter Gekelman, Mark J. Kushner. "E–H transitions in Ar/O2 and Ar/Cl2 inductively coupled plasmas: Antenna geometry and operating conditions". J. Appl. Phys. 133 (17), 173302 (2023)

3. **Yuchen Qian**, Walter Gekelman, Patrick Pribyl, Tom Sketchley, Shreekrishna Tripathi, Zoltan Lucky, Marvin Drandell, Stephen Vincena, Thomas Look, Phil Travis, Troy Carter, Gary Wan, Mattia Cattelan, Graeme Sabiston, Angelica Ottaviano, Richard Wirz. "Design of the Lanthanum hexaboride based plasma source for the large plasma device at UCLA". Rev. Sci. Instrum. 94 (8), 085104 (2023)

1 Introduction

1.1 Fundamentals of Plasma Etch

Semiconductor device manufacturing is one of the fastest growing industry since the invention of integrated circuits in 1960s. It wouldn't be an exaggeration to say that consumer products nowadays have universal dependence on microelectronics, typically made of semiconductor materials. The famous Moore's law observed and predicted that the number of components in an integrated circuit doubles every two years. As the industry keeps pushing the limit of compactness and complexity of the microchips, innovative research on improving efficiency and stability of semiconductor fabrication becomes important.

During the typical steps of wafer manufacturing, a wafer is first deposited with a film of materials, which is then covered by a layer of photoresist pattern mask through lithography. Materials not covered by the photoresist are removed in the etching process, and thus the desired pattern is transferred to the film. The photoresist is then cleaned from the wafer, and the next film is deposited. The steps repeat layer by layer until all the layers are stacked and the chip is completed. Many of the above steps happen with the aid of plasma, or in plasma-filled environment. Understanding of the fundamental properties of processing plasma is therefore key to the development of semiconductor industry. Plasma processing is primarily used in etching, deposition and surface cleaning. The early etching method utilized chemical solutions to dissolve the materials and is therefore called "wet etching", as opposed to the plasma-based "dry etching", developed later in 1970s. Compared to wet etching, plasma etching has the advantage of being anisotropic, controllable, having higher resolution and leaving no chemical waste in the system. It is now the generally preferred method for pattern-transfer [1]. Plasma etching is usually conducted in low pressure partially ionized non-equilibrium plasma. The typical operating conditions and plasma parameters are listed in Table 1.

The mechanism of plasma etching includes the directional but non-selective physical process such as sputtering, and the selective but isotropic chemical process. Depending

Pressure	0.1 mTorr - 1 Torr
Density	$10^{8} - 10^{13}$ cm^{-3}
Electron temperature	1 - 10 eV
Ion temperature	< 0.1 eV
Degree of ionization	$10^{-6} - 10^{-1}$

Table 1: Typical operating conditions and parameters of plasma used in etching.

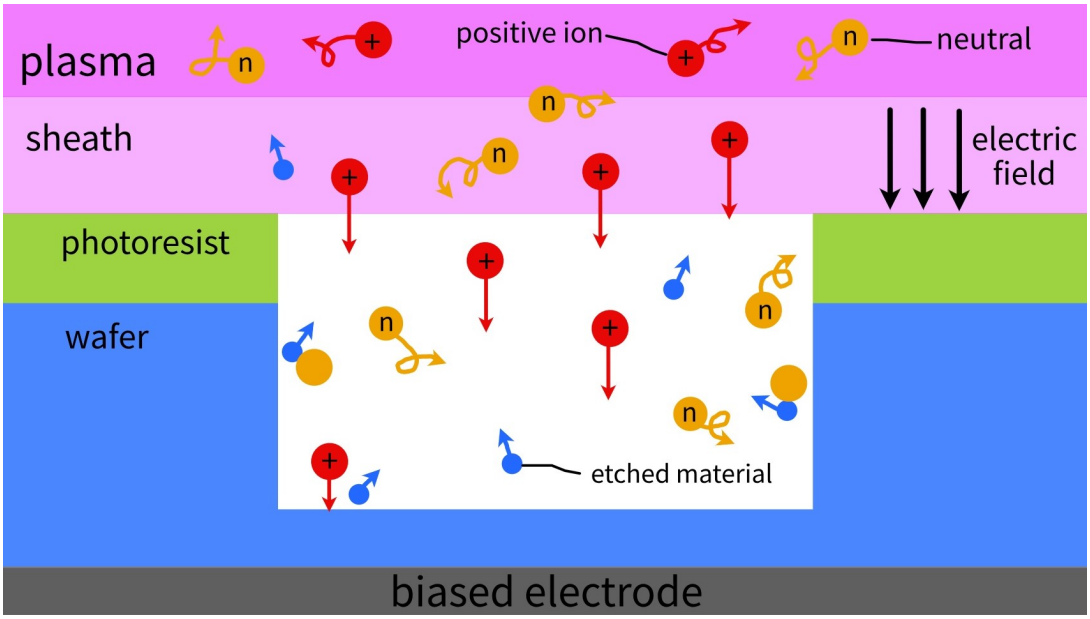

Figure 1: Schematics of plasma etching. Feature size are not drawn to true proportion.

on the material, the etching can be purely physical, purely chemical or a combined process (ion enhanced etching). Figure 1 shows the microscopic picture of such a process. As electrons are far more mobile than ions, they tend to escape from the plasma boundary, creating an electron devoid sheath with a voltage drop with respect to the grounded surface. The wafer is usually placed on an AC biased electrode with blocking capacitor, which self-generate a negative DC bias from the impinging electrons [2]. The DC self-bias further enhances the sheath potential. Positive ions accelerated by the sheath potential bombard the wafer and sputter atoms from the surface. The sputtered atoms combine with the chemically reactive neutrals in the plasma into volatile gas, and are evacuate from the chamber through the pumping system.

The neutrals also directly remove materials, especially from the sidewall of the trench. They move in isotropic direction through diffusion and thermal motion, and form chemical bonds with atoms on wafer upon contact [3, 4]. In practice, the etching process of one

wafer often involves a sequence of different feed gases and discrete steps to achieve the desired etch rate and selectivity [5].

Plasma used for etching is often generated capacitively by a pair of parallel electrodes, or inductively by an RF electromagnetic coil. In a capacitively coupled plasma (CCP) device, the wafer is positioned on the biased plate, or less commonly on the ground plate. This geometry is ideal for etching the dielectric and insulating materials which tend to have stronger bond energy and require very high energy ions. In an inductively coupled plasma (ICP) device, the wafer is usually placed on a chuck connected to a bias power source. Due to strong power coupling of electromagnetic field to the plasma, ICP generally can have higher plasma density than that of CCP at the same operating pressure and input power. ICP is often used to etch conducting materials such as metals and silicon that requires less ion energy but can be more efficient with large ion population. It plays important roles in the latest development of high aspect ratio (HAR) etching and atomic layer etching (ALE) [5–7].

Enormous efforts have been made on optimizing the plasma so that the etch profile can be precise and uniform. Key plasma properties that are essential to the precision, uniformity and efficiency of the etch include Key plasma properties that are essential to the result include species densities, ion and neutral fluxes, energy distributions, plasma temperature and power coupling to the plasma, etc [8].

The decoupling of the plasma power source and the bias power source and the utilization of multi-frequency system greatly expand the parameter space of the device. The source power usually runs at a higher frequency and controls the plasma density. The bias power controls the ion energy and usually runs at a lower frequency. The effects of the source frequency and the bias frequency are largely independent and can be studied separately as long as the frequencies are widely separated. Nonlinear interactions may happen when the frequencies are close. The influence on plasma density and potential is significant in CCP but not in ICP. For ICP, the DC bias and sheath voltage are sensitive to nonlinear effects [9].

While the dual-frequency system is the most commonly seen in etch devices, more

complicated mechanisms such as dual-frequency/dual-antenna with power splitting, superimposed multi-frequency antenna etc. have also been proposed and shown to improve discharge uniformity over the wafer [10, 11].

To further expand the "control knob" of the plasma parameter, industry is developing pulse-power modulation etch tools in which the source power and the bias power can be rapidly pulsed. The most common power modulation for pulsed etch device is square wave, although novel waveform is also being researched and developed. The plasma source power switches from "on" or "high", during which plasma is generated and sustained, to "off" or "low", during which the plasma cools down to afterglow. The bias power can be continuous, or pulsed in synchronization with the source power. The repetition rate, duty cycle and the time shift between the source pulse and bias pulse are all optimizable parameters to control the etch result [4].

Pulsing the plasma provides additional control on customizing fluxes to the wafer [8, 12]. It is particular important for aspect-ratio dependent etching, where neutral and ion fluxes are not uniform at the etch front that has different trench sizes and uneven pattern density [13]. This issue can be effectively addressed through pulsed operation. The pulse-off phase increases neutral coverage, and pulse-on phase enhances ion bombardment [14].

Other chamber conditions such as the asymmetry of gas flow and pumping may also cause nonconformity on the etch result. While continuous operation keeps reinforcing the asymmetry, pulsed operation recoup the symmetry through inter-pulse diffusion in plasma afterglow [15]. Pulsing also reduces damage to the wafer due to electron shading effects (electrons at oblique incidence cause local charging and damaging current), which is a common problem in continuous plasma [16, 17].

Recently, further bias power modulation has been investigated for enhanced control over energy distribution. Various tailored voltage waveform has been proposed. Its effect on the ion energy distribution was experimentally computationally compared to the case of conventional sinusoidal waveform, showing favorable results [18–20].

Experiments described in this thesis were conducted in an ICP device with a planar coil placed on top of the chamber. The source power and the bias power operate at

decoupled dual-frequency, and can be simultaneously pulsed with adjustable time shift with respect to each other. The pulsed operation and the separate tuning of bulk plasma and sheath necessitate measurement on the time evolution and spatial distribution.

1.2 Etch in Electronegative Plasma

Plasma processing often uses a combination of noble gases such as hydrogen and argon, and chemically reactive gases such as oxygen and halogen gases. For example, SiO_2 is often etched in high polymerizing fluorocarbon gases (CF_4, CHF_3, CH_2F_2, etc.) with argon and oxygen. The argon ion bombardment and CF_x radical flux incident on SiO_2 form a polymer layer on the surface. Highly energetic ions penetrating the polymer and fluorine diffusing through the polymer remove Si as SiF_4, SiF_2 and $SiOF_2$. Oxygen can remove carbon buildup on the surface, consume polymer layer by forming the volatile CO and CO_2, and therefore control the etch rate and selectivity. Selectivity can also be optimized through F/C ratio or addition of hydrogen that scavenges fluorine [21]. Apart from F-based gases, Cl- and Br-based gases are also commonly used to etch Si-based materials. [22–24].

This thesis reports on measurement done in Ar/O_2 plasma. Regardless of the choice of halogen species, argon and oxygen are frequently added to the process gas for reasons described above. Oxygen easily forms volatile species with carbon or hydrogen based atoms on the wafer surface, making it ideal for surface activation and cleaning. Argon is widely used for ion bombardment because of its low price among the inert gases. Almost all materials can be removed by argon plasma etching with sufficient energy. It also prevents oxidation of metals when oxygen gas is in use. Therefore, Ar/O_2 plasma has great research importance.

A key feature of plasma containing oxygen or halogen is the presence of negative ions which complicate the dynamics of species and plasma stability. In low pressure plasmas, negative ions are mainly formed by dissociative attachment such as in chlorine ($e + Cl_2 \rightarrow Cl + Cl^-$) and carbon tetrafluoride ($e + CF_4 \rightarrow F^-, CF_3^-, F_2^-$), or three-body attachment as in oxygen.

Negative ion species found in oxygen plasma are mostly O^-, O_2^-, O_3^-. The major loss mechanisms include positive ion-negative ion neutralization and electron detachment [25, 26]. In the regime relevant to plasma processing, negative ions are largely contained in the bulk plasma by potential barrier of ambipolar fields, and do not interact with the surface during the active-glow phase. The resulting plasma is therefore an electronegative core surrounded by an electropositive boundary region. Properties of low pressure RF oxygen plasma have been experimentally studied by many. Earlier investigations were mainly conducted in 13.56 MHz continuous oxygen plasma [27–30], where Langmuir probe, photodetachment, mass spectroscopy and microwave resonance were used to identify the ion species and measure negative ion parameters. A parabolic density profile across the chamber was observed by Vender *et al.*, with O^- being the most abundant specie [28]. Amemiya found that the negative ion density ratio (negative ion density / electron density) increases then decreases with the input feed power, and increases with gas pressure until saturates [29]. Corr *et al.* systematically studied the neutral and charged particle dynamics in oxygen ICP at both capacitive and inductive modes, and compared to a global analytical model [30].

As growing attention has been paid to pulsed operation and multi-frequency system, measurement and modeling on time-varying electronegative plasma became important. Plasma parameters as a function of RF phase has been extensively measured. For example, Schulze *et al.* measured electron dynamics and energy distribution functions within the RF cycle in a dual-frequency He/O_2 CCP with one-dimensional spatial resolution, using phase-resolved optical emission spectroscopy [31]. Similar investigation was conducted in an oxygen containing ICP by O'Connell et al, focusing on power scanned mode transitions [32].

Temporal evolution of the key parameters during different phases of the pulse has also been extensively studied. Particular time frames to be considered are onset of the pulse, where mode transitions and multiple nonlinear effects may happen, the quasi-equilibrium active-glow, and the afterglow. For example, Mishra *et al.* identified three distinguishable features in the plasma potential and electron temperature profile during a single pulse

cycle [33]. Mitsui and Makabe gave a complete review on the 2D/3D emission tomography on each phase of the E-H and H-E transition electronegative in ICP [34].

Ion motion at the vicinity of the wafer is another important and ongoing research topic. Retarding field energy analyzer, modified to be used in the presence of high voltage RF bias, has been a popular way to measure the ion energy distribution function. Specie-resolved measurement can be obtained by further combining the energy analyzer with a mass filter or mass spectrometer [35–41]. Laser based non-intrusive diagnostics, such as cavity ringdown spectroscopy [42, 43] and laser induced fluorescence (LIF) [44–50], captures velocity information of a single ion species through Doppler shift and broadening.

A comprehensive measurement focusing on both volumetric resolution and temporal resolution was previously by Han *et al.* [51], who systematically studied the argon plasma in the same ICP device and laid the groundwork for this thesis.

The progress on diagnostics in low temperature electronegative plasma greatly benefits the research on plasma modelling. This is important to the industry as etching devices are monitored and improved with the aid of computer models [52]. Common simulation approaches include fluid, particle-in-cell (PIC) or hybrid method. The fluid models describe plasma by solving the continuity and the energy equations for each species in the plasma, with appropriate coupling to RF electromagnetic fields. They are useful to obtain multi-dimensional global model efficiently, when non-local effects are less important. PIC models solve kinetic equations for sampled individual particles, and are often used in low density plasma when an accurate local description is needed. Hybrid models combine the fluid and PIC approaches. Development and challenges of the three methods are reviewed by Kim et al [53]. In recent years, Kushner developed a Hybrid Plasma Equipment Model (HPEM) in which a large variety of physics is compartmentalized into different modules and module calculations on different timescales are iteratively combined using time-slicing techniques. Abundant results using HPEM to address various issue in pulsed electronegative plasma has been published [20, 54–56]. This thesis will also present comparison of some of the experimental results with the HPEM calculations.

1.3 Motivation and Outline

Plasma etching has been constantly challenged by the fast advancement of 3-dimensional geometries of microelectronics. Recent development on 3D NAND and 3D DRAM has push the aspect ratios to exceed 100. The etching must be as precise as possible on a nanometer scale, and at the same time highly uniform such that the chips produced are of the same quality across the wafer. This requires that ions arrive with near normal angles with narrow angular spread ($<$ a few degrees) and high energy ($>$ several keV) [57–59]. Ion energy distribution and motion is therefore key to semiconductor device fabrication and needs thorough study with the most advanced methods. To ensure quality among all wafers, the plasma itself should also be stable, controllable and reproducible. Power delivery from the source to the plasma should be efficient and repeatable. The electronegativity of the plasma further complicate these challenges. This necessitates scientific research to fully characterize the plasma in etched devices with high spatial and temporal resolution.

This thesis focuses on characterizations of pulsed ICP with an improvement on spatial and temporal resolution that has not been achieved in previous research. The operating gas is Ar/O_2 at varying mixing ratio, which is commonly used in etch process. Features essential to industrial application such as positive ion motions, negative ion concentrations, induced field distribution and power deposition will be studied. Experiments are designed to explore various time regime of the pulsed operation (onset of the pulse, steady state, afterglow), and access different region in the plasma (under the coil, bulk plasma region, above the wafer).

Chapter 1 introduces readers to the concept and development of ICP plasmas for industrial applications. Chapter 2 describes the specifics of our ICP chamber and plasma source. Following that are explanations on our built-in-house data acquisition system and various diagnostics with which we obtained the results shown in Chapter 3, 4 and 5. Chapter 3 presents our laser induced fluorescence experiments on studying positive ion motions above the wafer. Chapter 4 discusses our measurement on negative species, i.e. electrons and negative ions, in varying mixing ratios of argon and oxygen gases. Chapter 5

discusses the induced electromagnetic fields and power deposition in these gases. Chapter 6 concludes the key results from this thesis and discuss on further possibilities of the lab.

2 Laboratory Setup

2.1 Plasma Chamber

The experiments are conducted in a cylindrical vacuum chamber donated by LAM Research Corporation. The chamber is constructed of anodized aluminum with an internal diameter of 52 cm. A flat ceramic lid seals the top. The chamber is modified to have multiple Pyrex view ports and one probe access port, as shown in Figure 2.

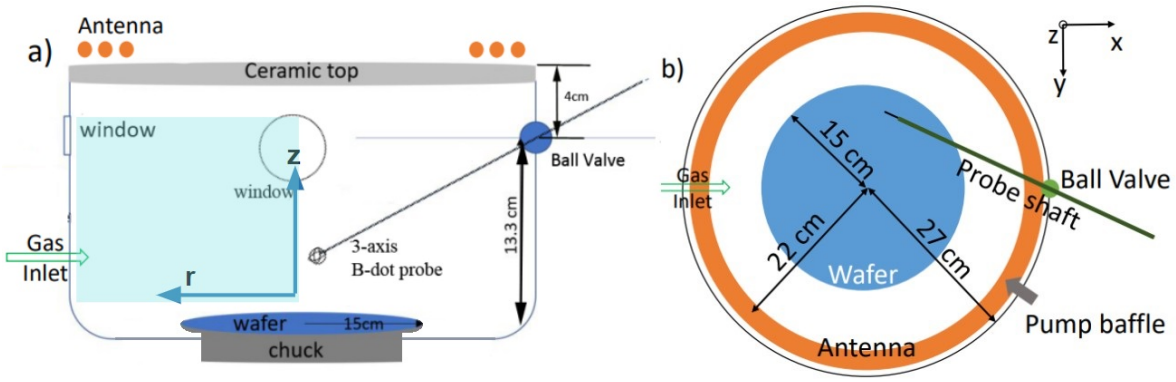

Figure 2: Schematics of the plasma chamber. (a) Side view. (b) Top view. The semi-transparent blue rectangle shows the typical data collection plane that the probes scan through. The x and z axis is defined as the radial and axial axis of the cylinder, with the origin at the center of the wafer.

A roughing pump and a turbo pump (Adixen ATH2303M) attached to the bottom of the chamber keep the vacuum pressure level at 2×10^{-6} torr. Feed gas is premixed in the pipe system before entering the chamber from an inlet on the side wall. Each specie of gas is controlled by a mass flow controller. The pressure in the chamber is conditioned by the turbo pump setpoint and mass flow controllers. The majority of the experiments are conducted at 0.5 - 50 mTorr.

A 30 cm diameter Si wafer is positioned on a 45.5 cm diameter RF chuck assembly at the bottom of the chamber, 17.2 cm away from the ceramic lid. The wafer is electrostatically clamped on the chuck which has backside helium inflows for cooling. The which can be biased with respect to the chamber ground.

The plasma is generated by a double-wound 1.5 turns planar spiral coils, situated 1 cm above the surface of the lid. The RF power in the coil i s delivered to the plasma

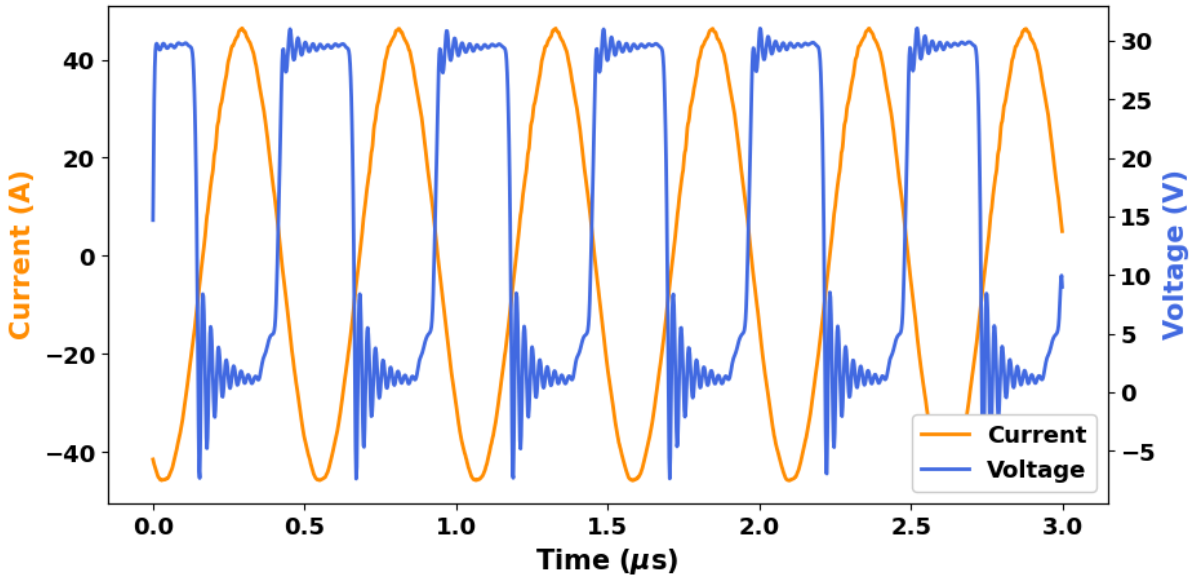

Figure 3: Several cycles of the 1 MHz antenna current (orange, left axis) and voltage (blue, right axis), measured at the terminal of the coil. The power is 400 W.

mainly through induction, although in cases of low density plasma conduction mode can dominate and E-H transition is always present in the pulsed operation of this machine [51].

The coil antenna and the chuck are powered by separate power sources at adjustable duty cycle and RF frequency. For the work presented here, the antenna current is 2 MHz and the chuck bias is 1 MHz. The antenna is typically pulsed at 10 Hz between on/off, or high power/low power. 10 Hz matches the pulsing rate of our Nd:YAG laser. The rise-time of the pulse is 50 µs and the maximum power is set between 300 W to 1 kW. Although the pulse waveform can be tailored to any shape that's allowed by the function generator, it is largely limited by the rise-time and maximum power. The presence of plasma also complicates the circuit response. In this thesis the antenna is always on square pulse. The antenna power is calculated by the multiplication and taking the root mean square of the measured voltage and current at the terminal of the coil. Power lost between the terminal and the plasma is only a few percent, confirmed experimentally by Han [60] using a single turn loop inductively coupled test circuit just above the antenna. A exemplary RF current and voltage profile operating at 400 W is plotted in Figure 3.

The chuck bias can be continuous or pulsed between on/off synchronously with the

antenna pulse with adjustable time shift and duty cycle.

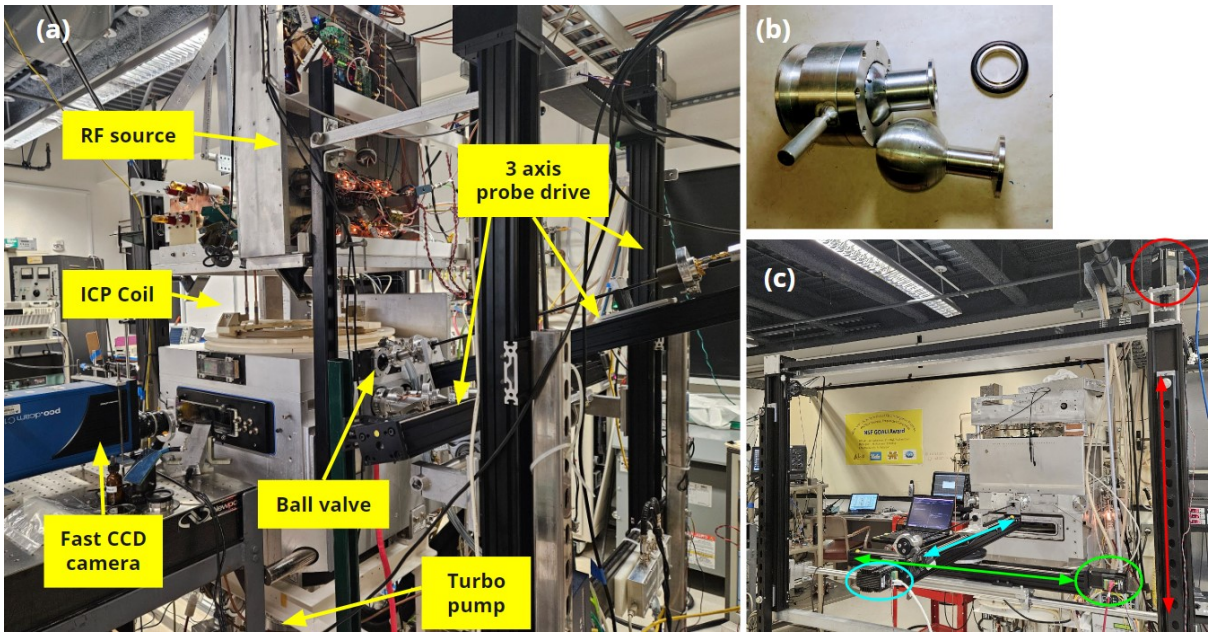

Figure 4: Photos of the ICP chamber. (a) A side view of the ICP tool. The gas inlet is on the other side and not shown. (b) Details of the custom ball valve. (c) The 3-axis motor drive system. The tricolor arrows indicates the movement direction of each slide track (blue for in/out, green for sideways, red for up/down), and the stepper motor that motorizes each track is circled with the corresponding color.

The chamber has two rectangular view ports near the top, facing the area under the coil, and one rectangular and one circular view port at the bottom, facing the area above the wafer. These allow access of interferometer and laser. All view ports are sealed with pyrex. A photodiode is mounted next to the bottom rectangular view port to monitor visible plasma breakdown.

Probes can access the chamber through a custom made ball valve (Figure 4(b)) which allows free rotation [61]. A three axis motor system can move the probe tip to access most places inside the chamber, except a small fan-shaped volume right below the ball valve. In practice, we usually assume cylindrical symmetry and collect data on a half plane, shown as the semi-transparent blue region in Figure 2, to protect the probe tip and save time. The motor system is consisted with three slide tracks motorized by Applied Motion integrated stepper motors and linear actuators (Figure 4(c)). The motors can be controlled by remote command through Ethernet connection. The coordinate in the chamber, defined as shown in Figure 2(a), is mapped to the coordinate of the motor

system and translated to motor rotation by a computer program developed in house.

2.2 Data Acquisition

Data collected by probes are digitized by oscilloscopes and recorded to a computer. In most cases, the oscilloscope is triggered with respect to the rising edge of the RF antenna current pulse.

The experiment procedure is largely automated through a python based data acquisition (DAQ) program. After the initial physical set up is completed, the data collection is routined by the program. This includes moving the probes, changing the operating parameters / oscilloscope settings, organize and save the data, etc.

The DAQ program incorporates individual python scripts that communicate with the lab devices, and a main function that setup and execute the data acquisition loop. Each script can be executed as standalone program to individually control the devices. The lab is equipped with several Teledyne LeCroy oscilloscopes, all of which can read from and write to the host computer through Ethernet connection and National Instrument driver NI-VISA. The commands use Standard Commands for Programmable Instruments (SCPI) syntax. The function generators and delay generators are also remotely controlled through SCPI over Ethernet.

The RF power supply of the stovetop coil plasma source is remotely controlled through USB connection. Essential parameters such as mode of operation, RF frequency, current/voltage phase can be adjusted.

The stepper motor communicates with the host computer through Structured Control Language (SCL) over Ethernet. The program automatically translates the user input position in Cartesian coordinate to motor encoder position.

Figure 5 shows the workflow of a typical experiment designed to obtain volumetric data by moving a probe to multiple locations inside the chamber. The program generates an indexed DAQ array from the user input. Each array entry contains information on the probe location and other parameters (i.e. trigger time, probe bias, laser wavelength, etc.) at that position. After initializing the connections to all the devices, the program

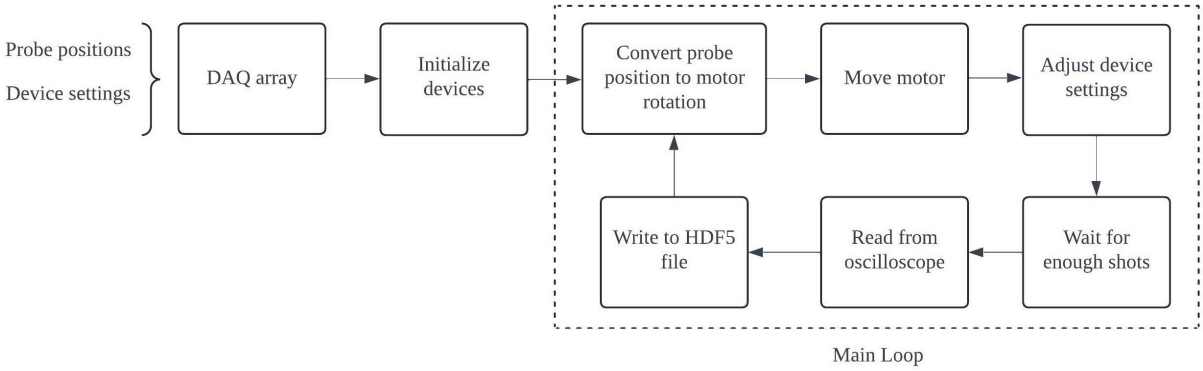

Figure 5: An example workflow diagram of the Python based DAQ.

loops through the DAQ array and records the data. This typically includes moving the probe, changing device settings, saving the scope traces, and then moving to the next array entry. The data, as well as other experiment information, are packed into a single HDF5 file. The program is highly customizable to include new apparatus and procedures, and easily transferable between labs.

2.3 Diagnostics

2.3.1 Langmuir Probe

Langmuir probes are one of the most common diagnostics in plasma physics due to their simple constructions. A basic Langmuir probe contains a conducting probe tip exposed to the plasma. In most Langmuir probe diagnostics, a bias voltage is supplied to the probe tip, and the current flowing through the probe is measured. With proper choice of biasing condition and careful treatment of data analysis, a variety of information can be extracted.

A common application is to sweep through a range of bias voltage to obtain the current-voltage characteristic (I-V curve). When inside the plasma, the probe surface will be shielded by a layer of Debye sheath whose properties determine the current flowing through the probe. The total current I collected by the probe is the sum of the electron current I_e and the ion current I_i. Figure 6 shows an idealized I-V trace, plotted upside-down (I_e positive and I_i negative) by convention.

In analysis, Langmuir I-V curve is typically divided into three parts. When the probe

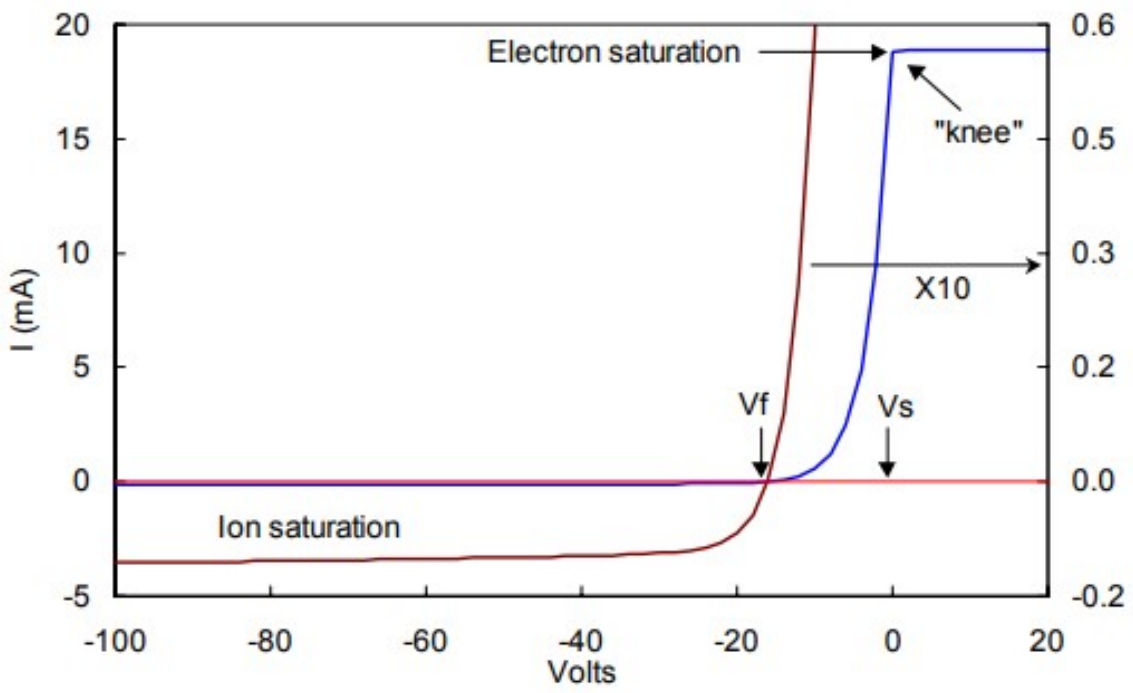

Figure 6: Idealized I-V curve. The current is plotted upside-down by convention. The ion saturation region is magnified 10 times for better visual effect. Figures from F. F. Chen [62].

tip is extremely negatively biased, it repels all the electrons and only collects I_i. This is called ion saturation current I_{sat}. The Bohm sheath criterion requires that ions entering the sheath travel at least at the ion sound speed $c_s = \sqrt{k_B(ZT_e + \gamma_i T_i)/m_i}$, where k_B is the Boltaman constant, T_e and T_i are the electron and ion temperature, Z is the ion charge number and γ_i is the ion adiabatic coefficient. $\gamma_i T_i$ is often ignored in cases of cold ions, and the equation is shortened to $c_s = \sqrt{k_B Z T_e/m_i}$. If most ions in the sheath are at the sound speed, the value of the saturation current is then $I_{sat} = qn_e c_s$, where q is the electron charge, n_e is the electron density. Therefore, information on n_e can be extracted from I_{sat} if T_e is known.

When the probe tip is biased at the floating potential V_f, I_e and I_i balances and net current becomes zero. Passing the floating potential, I_e keeps growing until the probe bias is equal to the plasma potential V_{pl}, at which the electron collection saturates and the I-V curve turns flat. Since electrons are much lighter in weight and more mobile than ions, electron saturation current has much larger magnitude than ion saturation current. In practice, the turning point at V_{pl} is usually smooth. Directly pinpointing the location

of V_{pl} is often difficult, especially when the sheath dynamics is complicated or the plasma density is small.

If the electron distribution is Maxwellian, I_e grows exponentially in the transition region between V_f and V_{pl}:

$$I_e = I_{es} e^{q(V_{pr}-V_{pl})/kT_e} \tag{1}$$

where I_{es} is the electron saturation current and V_{pr} is the probe bias potential. The slope of $\ln I$ against V_{pr} is q/kT_e, providing direct measurement on the electron temperature. To obtain I_e in the transition and electron saturation region, I_i can be extrapolated from the ion saturation region and subtracted from the total current. This method of separating I_e and I_i usually provides good enough estimation.

Another common way to obtain information on T_e and n_e is by taking the second derivative of the electron current. For cylindrical probe in isotropic plasma, I_e'' is related to the electron energy probability distribution function (EEPF) by the Druyvesteyn formula [63]:

$$\frac{dI_e^2}{dV_{pr}^2} = -\frac{e^2 A_p \varepsilon_e}{4}\sqrt{\frac{2e}{m_e V_{pr}}} EEPF(\varepsilon_e) \tag{2}$$

where ε_e is the electron energy and A_p is the probe electrode area. T_e and n_e can then be calculated by taking the appropriate integral of I_e'' over the energy space:

$$N = \frac{2\sqrt{2m_e}}{eA_p}\int_0^{-\infty} I_e''(V_{pr})\left(\frac{V_{pr}}{e}\right)^{1/2} dV_{pr} \tag{3}$$

$$T_e = \frac{4\sqrt{2m_e}}{3NA_p}\int_0^{-\infty} I_e''(V_{pr})\left(\frac{V_{pr}}{e}\right)^{3/2} dV_{pr} \tag{4}$$

The Druyvesteyn method of taking the second derivative is easy to implement without assuming Maxwellian distribution and very straightforward to interpret. However, it requires high signal-to-noise ratio and is extremely sensitive to any small distortion on the I-V curve.

There are several difficulties when a Langmuir probe are used in an ICP device [64].

Since the ICP device is electrode-less, it lacks an obvious reference point for the probe. The connections to bias source and oscilloscope should be carefully planned out. In our setup, equipment are isolated from the wall outlet ground through cheater plugs, and the chamber wall serves as a common reference ground. More importantly, the plasma potential V_{pl} oscillates with the background RF from the coil and biased electrode. In such an environment, signal picked up by an uncompensated Langmuir probe is averaged over the fluctuating V_{pl}, and the I-V curve is distorted from its true shape. This leads to an overestimated T_e and underestimated n_e [65, 66].

The influence of RF background can be removed by making the probe to ground impedance Z_p much larger than the probe to plasma (sheath) impedance Z_s at RF frequency. This is usually achieved by a passive choke chain consisted of self-resonating inductors. In low density plasma where Z_s is so high that it becomes impractical to achieve $Z_p \gg Z_s$ simply through a choke chain, an auxiliary coupling electrode is often used to let the tip float with RF and therefore reduce the required value for Z_p [67–70].

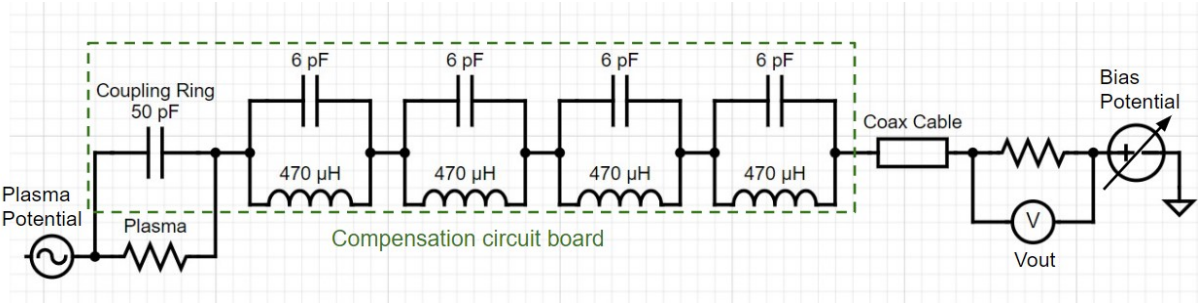

Figure 7: Equivalent circuit of the RF compensation Langmuir probe in RF plasma.

Frequencies of our concern are 2 MHz from the RF source, 1 MHz from the wafer bias, and their higher harmonics. Since the system is dual-frequency, it is simpler to design a circuit that has high enough Z_p over a broad range of frequencies, rather than multiple Z_p peaks at selective frequencies. We based our circuit on Sudit and Chen's design [69, 70]. Figure 7 shows the equivalent circuit of the compensated probe immersed in the plasma. The compensation circuit has four 470 µH inductors (Bournes Inc. SRR4028-471Y, 3 MHz self-resonant frequency) in series with the probe tip, and a platinum wire as the coupling ring.

The circuit was evaluated by a Keysight E5100A network analyzer with a setting that

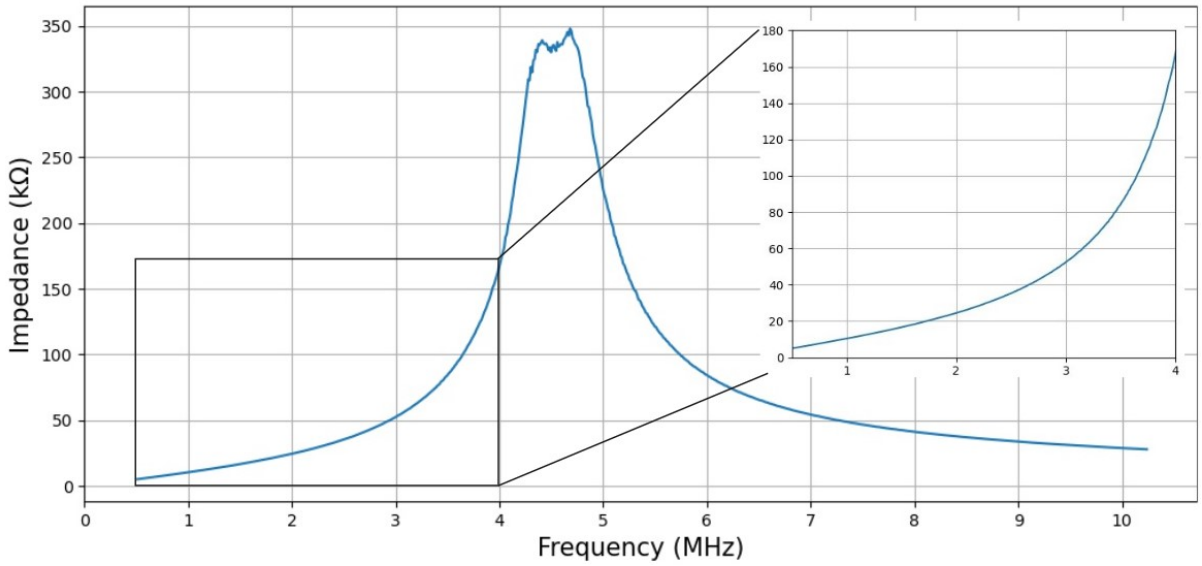

Figure 8: Impedance response of the RF compensation circuit.

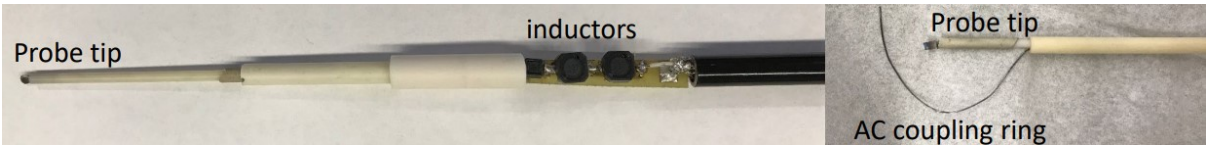

Figure 9: Photo of a Langmuir probe tip with the compensation circuit and AC coupling ring, taken before epoxy was applied to cover the circuit board.

imitated Figure 7. A metal sheet combined with a resistor was used to model the plasma environment. The impedance response is plotted in Figure 8. Z_p is 10 kΩ at 1 MHz and 25 kΩ at 2 MHz. Both are large compared to the plasma resistivity measured to be around 1 kΩ at the center of the chamber. Z_p reaches 350 kΩ at 4.5 MHz, and maintains well above 10 kΩ at higher frequencies.

The circuit is placed as close to the probe tip as possible to avoid extra capacitance, as shown in Figure 9. When in use, the circuit board is covered by epoxy to be shielded from direct contact with the plasma, and the coupling ring is wrapped around the ceramic tube exposed to the plasma.

In addition to the RF background, effect of negative ions should also be considered when using Langmuir probe in processing plasma. It changes the effective sheath size and ion velocity at the sheath edge. The difference in mobility of negative ions and electrons causes the formation of a negative ions free sheath around the probe. This makes negative specie measurement very prone to error [71]. Amemiya [72] and Bredin

et al. [73] thoroughly discussed the challenge and limitations of using Langmuir probe in electronegative environment. In general, saturation current analysis is favorable in plasma with lower negative ion concentration, with the appropriate sheath correction and model. EEDF analysis is favorable in plasma with higher pressure as distinctive energy peaks of electrons and negative ions maybe observed.

2.3.2 Hairpin Probe

A hairpin probe provides measurements on local electron density. Compared to a Langmuir probe, it has the advantage of being relatively immune to surface contamination and fluctuating plasma potential V_{pl}. The tip of a hairpin probe is a U-shaped resonator ('hairpin') whose resonance frequency is [74]

$$f_r = \frac{c}{2(2L+w)\sqrt{\epsilon_r}} \tag{5}$$

where L is the length of the hairpin leg, w is the width between two legs, ϵ_r is the relative permittivity surrounding the probe and c is the speed of light.

In vacuum, $\epsilon_r = 1$ and the resonance frequency is $f_0 = c/2(2L+w)$. In an unmagnetized plasma, ϵ_r is shifted from the unity:

$$\epsilon_r = 1 - \frac{f_p^2}{f^2} \tag{6}$$

$$f_p^2 = \frac{e^2 n_e}{\epsilon_0 m_e} \tag{7}$$

where f_p is the plasma frequency, e is the electron charge, m_e is the electron mass, ϵ_0 is the vacuum permittivity and n_e is the electron density. For $f = f_r$, it can be derived from Equation 5 that $f_r^2 = f_0^2 + f_p^2$. Therefore n_e in the surrounding of the probe surface is related to f_r by a simple relation:

$$n_e = \frac{\epsilon_0 m_e}{e^2}\left(f_r^2 - f_0^2\right) \tag{8}$$

Corrections can be included to account for the sheath effect around the cylindrical

hairpin. At higher pressure, collisions should also be considered. Sands *et al.* [75] suggested on a correction factor $1/\zeta_s\zeta_c$ in front of Equation8, where ζ_s is the sheath correction and ζ_c is the collision correction

$$\zeta_s = 1 - \frac{f_0^2}{f_r^2}\left[\frac{\ln\left(\frac{w-a}{w-b}\right) + \ln\left(\frac{b}{a}\right)}{\ln\left(\frac{w-a}{a}\right)}\right] \tag{9}$$

$$\zeta_c = \frac{1}{1 + \left(\nu_{en}/2\pi f_0\right)^2} \tag{10}$$

Here a is the hairpin radius, b is the sheath radius that can be calculated from an appropriately chosen sheath model, and ν_{en} is the electron-neutral collision frequency.

f_r can be found by scanning through a range of frequencies and locate the maximum transmission or minimum reflection. In a transmission type probe, the hairpin tip is sandwiched between two electrically isolated loop antennas, one for sending the microwave signal to the resonator, and the other for receiving the transmitted signal from the resonator. In a reflection type probe, only one loop is used and the reflected power is measured.

We decided that the transmission type hairpin probe has better performance in our machine. The two loop antennas are made from copper coaxial cables. It was observed that the bending of the cable may disturb the signal, so we chose the semi-rigid coaxial cable UT-034M from Amawave19 with OD = 0.034 in. (0.87 mm)

The tip of the cable is stripped and wrapped around a cylindrical tool to form a loop. The loop is closed by soldering the inner conductor to the outer conductor. We keep the insulator layer of the coaxial cable on the loop except for the solder point to ensure that the loops and hairpin are electrically isolated.

The remaining cables are shielded in a cylindrical stainless probe shaft with free opening on one end and limo connections on the other end. A short ceramic tube is fitted into the open end to support the coax cables and loops that stick out from the shaft.

The hairpin was made by bending the wire into a U-shape and then trimming it into the desired length according to Equation 5. The position of the hairpin with respect to the two loops were tested out experimentally. We used a network analyzer to measure

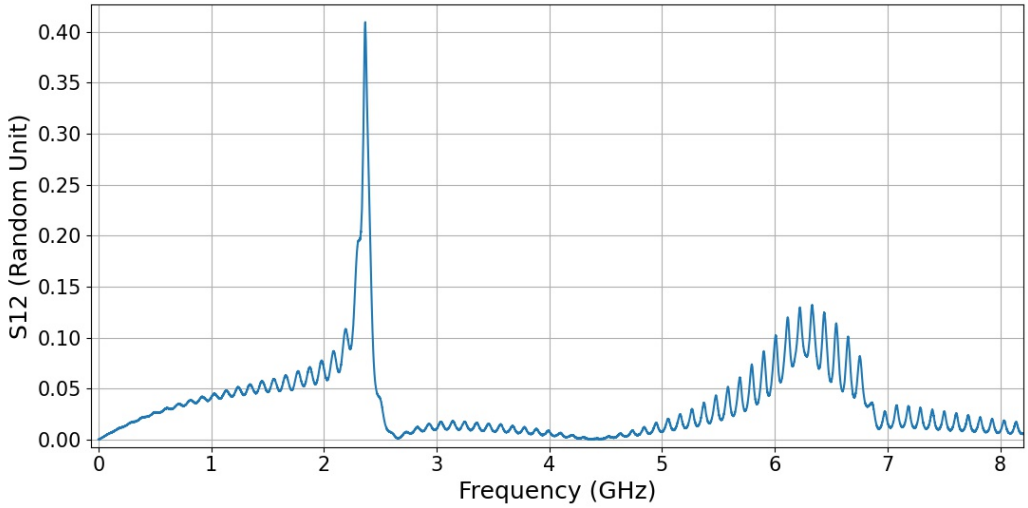

Figure 10: Magnitude of the transmitted power s-parameter S12 of the hairpin probe, obtained from a frequency scan on a vector network analyzer. The S12 magnitude is plotted on linear scale with arbitrary unit.

the transferred power s-parameter S12 (with input cable on port 1 and pick-up cable on port 2) over a range of relevant frequencies. The shape and position of the hairpin were optimized so that the peak of S12 was as sharp as possible.

Figure 10 shows the measured S12 magnitude of one of the hairpin probe in air. The transmitted power has the strongest peak at 2.367 GHz, and a weaker peak at the harmonics around 6 GHz. The full width of half maximum (FWHM) of the resonance peak is 0.08 GHz, which is the resolution of our measurement ($\sim 2 \times 10^9 \mathrm{cm}^{-3}$ at f_0). The quality factor (Q factor) of the probe in air is around 29.

f_0 measured in the pumped-down plasma chamber is consistent with the resonant frequency in Figure 10. Therefore we decided that network analyzer measurement in air can be used to assess probe performance in vacuum as well.

The probe circuit was designed and made in-house for affordability. Figure 11 explains the basic workflow of our circuit. A voltage controlled oscillator (Analog Devices HMC586LC4B) converts 0 - 18 V control voltage into 4 - 8 GHz microwave signal, which is divided by 2 through a static divider (Analog Devices HMC432ETR) and coupled to the input loop. Signals picked up by the other loop is amplified and then down-converted by an IQ mixer (Marki Microwave MMIQ-0205HSM), with the picked up signal on RF

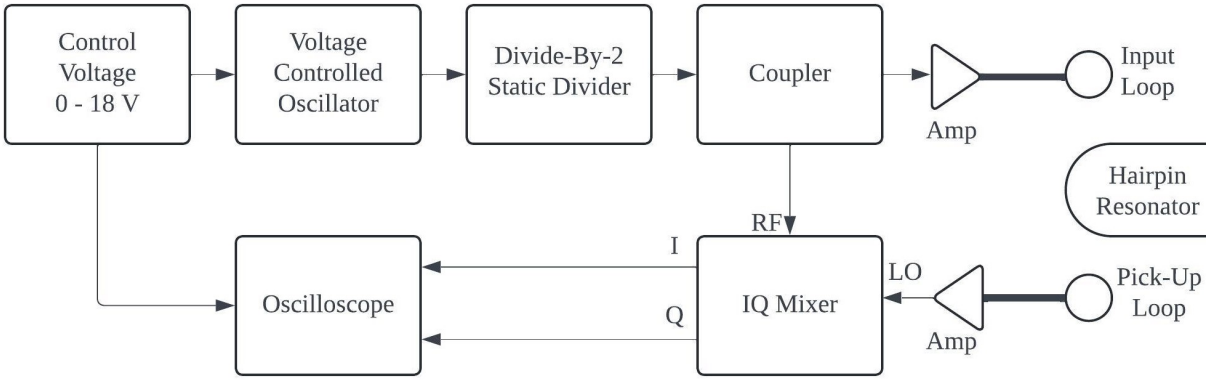

Figure 11: Schematic diagram of the hairpin probe circuit.

port and transmitted signal on LO port. The I and Q output from the mixer, along with the monitored control voltage, are recorded on the oscilloscope. Depending on the plasma condition, combinations of amplifiers were used to improve signal-to-noise ratio.

The time resolution of the probe is mainly limited by the mixer circuit, which has an overall response time of approximately 10 µs. The hairpin leg is 2 cm long and thus confines the spatial resolution.

Applications of hairpin probe, when combined with other techniques, can be extended beyond electron density measurement. Probe assisted photo-detachment method measures negative ion density n_- by detaching the electrons from the negative species using laser energy, and then tracking the local increase in n_e using a hairpin probe [76, 77]. When the photo-detachment process is saturated, the change in n_e is an absolute measurement of n_-. By coupling the hairpin to dc voltage and comparing the varying sheath width to the appropriate model, various parameters including the electron temperature, plasma potential and electronegativity parameter $\alpha = n_-/n_e$ can be obtained [78].

2.3.3 Magnetic Probe

The magnetic probes, also called Bdot probes, measure the induced magnetic field using Faraday's Law. The probe tips consist of n turns of conducting loops that develop electric potential in a changing magnetic field:

$$\oint \vec{E} \cdot d\vec{l} = -\int \frac{\partial \vec{B}}{\partial t} \cdot n d\vec{A} \tag{11}$$

where $\vec{E}$ is the induced electric field, $\vec{B}$ is the background magnetic field and $\vec{A}$ is the area of the loop.

The voltage picked up by the Bdot probe is then a direct measurement on the time derivative of the magnetic field, as the probe name suggests. $\vec{B}$ can be reconstructed from integrating a time series measurement over time, and $\vec{E}$ can be calculated by integrating a multi-dimensional measurement over space.

Using Ampere's law

$$\nabla \times \vec{B} = \mu_0 \vec{J} \tag{12}$$

the induced current $\vec{J}$ can also be calculated by taking the curl of a multi-dimensional measurement.

Figure 12: Probe tip of the three-axis 3.4 mm diameter Bdot probe, shielded with epoxy. Distance between the center of each loop is 5 mm

In this lab we use a three-axis Bdot probe which consists three 3.4 mm diameter single turn coaxial cable loops, facing orthogonal directions with respect to each other (Figure 12). The probe tip is made as compact as possible. The offset distance between each loop is 5 mm.

A small part of the outer conductor of each loop is carefully scrapped off, so that the inner conductor detects the changing field and the outer layer is open at the loop and connected to the circuit common on the other side of the probe shaft. The signals go through a three channels 100 gain 150 MHz differential amplifier before being digitized.

Before use, the probe is calibrated on a network analyzer (HP E5100A, 10kHz to

180 MHz), as shown in Figure 13. A Helmholtz coil was used to generate a reference magnetic field. The frequency response of the probe was obtained by comparing the probe output V_{pr} to the Helmholtz coil input V_{ref}. In the relevant frequency range (<60 MHz), the V_{pr}/V_{ref} shows positive linear relationship with the scanning frequency. The linear regression coefficient is taken as the calibration constant.

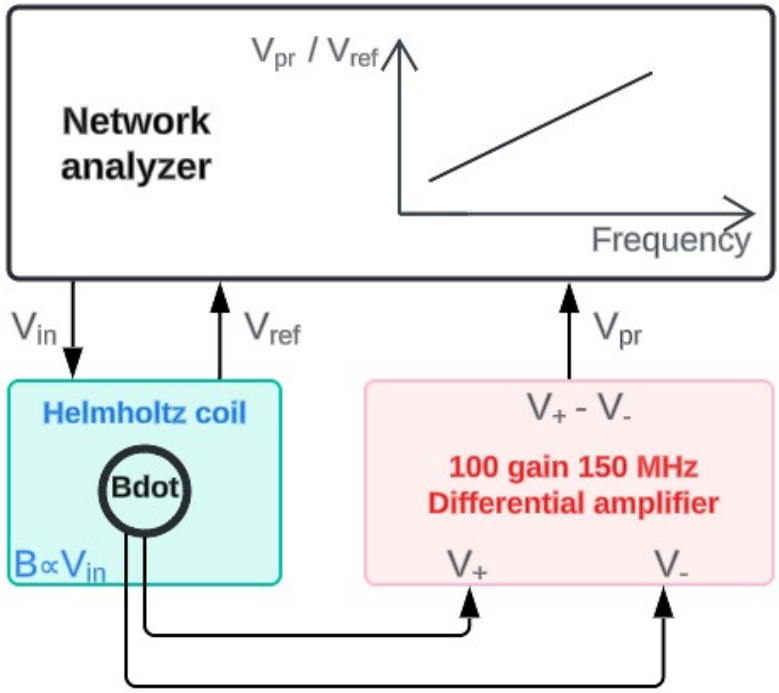

Figure 13: Block diagram of calibration setup for Bdot probe.

2.3.4 Laser Diagnostics

The lab is equipped with a frequency-doubled (532 nm) Nd:YAG laser (Spectra Physics Pro-230) which pulses at 10 Hz, and a tunable dye laser (Sirah CSTR-D-532) pumped by the Nd:YAG laser. Both lasers are set up on an optical table in a separate laser room. The laser light can be transmitted to the adjacent ICP room through an optical fiber, or directly through a hole drilled on the wall. Experiments conducted with laser diagnostics in this lab include photo-detachment using the direct output from the Nd:YAG laser, and laser-induced fluorescence (LIF) using dye laser output tuned around 611.661 nm.

The dyes used for the tunable laser are mixed in house, with primarily Rhodamine dyes dissolved in high purity methanol or 200 proof ethanol. Figure 14 shows the emission

spectrum of the dye laser using a mixture of Rhodamine 610 and Rhodamine 640 [79]. The laser has a narrow line width of 0.00136 nm when tuned to the maximum efficiency.

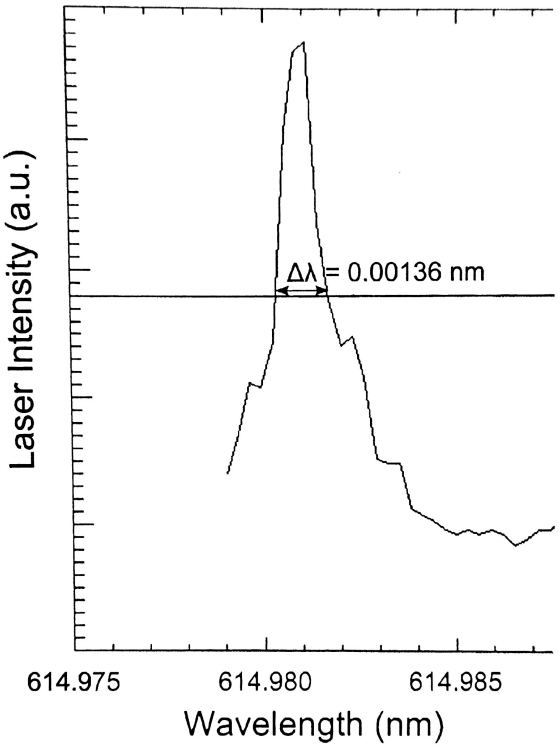

Figure 14: Spectrum of Sirah CSTR-D-532 dye laser obtained using a Fabry-Perot interferometer. The laser is tuned to the maximum efficiency for the dye mixture (Rhodamine 610 / 640 in methanol). From B. Jacobs' thesis [80].

The Nd:YAG laser accepts external trigger which can be synchronized with ICP source/bias and remotely controlled through Ethernet connection. The tuning of the dye laser is motorized and can be remotely controlled through serial communication. A wavelength meter (HighFinesse Wavemeter WS-6), regularly calibrated by HeNe laser, is used to read laser output wavelength and monitor its quality.

2.3.5 Michelson Interferometer

Microwave inteferometry provides non-intrusive measurements on the plasma properties. Signals travelling through different mediums undergo changes, and therefore the comparison between the initial signal and the detected signal exiting a plasma volume provide information on the plasma. A common diagnostics is to measure the plasma-induced phase change which is directly related to the line-integrated electron density along the

beam path: [81]

$$\phi_p = \frac{\omega}{c} \int_0^L \left(1 - \sqrt{1 - \omega_p^2/\omega^2}\right) dl \tag{13}$$

where ϕ_p is the phase shift in plasma, ω is the vacuum frequency of the probing microwave signal, c is the speed of the light, e and m_e is the electron charge and mass, L is the length of the beam path inside the plasma, and ω_p is the plasma frequency which is a function of electron density.

For low density plasma and high interferometer frequency, $\omega_p \ll \omega$. The equation is then simplified to

$$\phi_p = \frac{e^2}{2c\varepsilon_0 m_e \omega} \int_0^L n_e(l) dl \tag{14}$$

where $n_e(l)$ is the electron density as a function of the position l along the beam path.

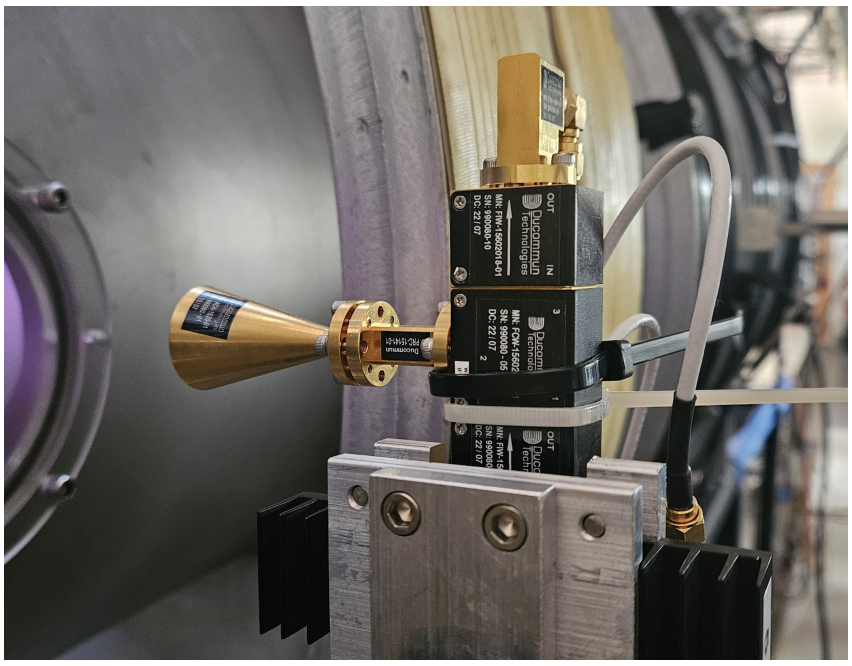

Figure 15: Photo of the homodyne Michelson interferometer.

Common types of interferometers used for plasma diagnostics include Michelson and Mach Zender, etc. The main difference lie in the configuration of the source, detector and beam path. In this lab we use a swept frequency Michelson interferometer as shown in Figure 15. A homodyne horn acts as both the source and the detector. The signal

enters through one of the pyrex view port on the side of the chamber and gets reflected by the chamber wall, travelling through the beam path twice.

Swept frequency interferometer was developed by Scime *et al.* for density measurement in steady state plasma, modified from the classic design of a zebra-stripe interferometer developed in the 1950's [82]. For $\omega_p \ll \omega$, the group delay of frequency swept signal is directly proportional to the line-integrated density. For typical processing plasma density (10^{12}cm^{-3}), the plasma frequency is around 9 GHz. The frequency of our interferometer is 60 GHz.

Figure 16 explains the circuitry setup. A 1 MHz voltage sweep (Figure 16(b)) is supplied to a Gunn diode, which put out a microwave signal in the range of 60 GHz to slightly above 60 GHz. The signal is transmitted to the horn through an isolator and a directional coupler. The use of a homodyne horn is made possible by taking advantage of directional coupler's defect. The superposition of a intentionally leaked signal (plasma leg) and the passed signal (reference leg) is [82]:

$$\begin{aligned} M(t) =& 2A \sin\left(\omega t + \frac{\phi_1 + \phi_p + \phi_2}{2}\right) \cos\left(\omega t + \frac{\phi_1 - \phi_p - \phi_2}{2}\right) \\ &+ 2(B - A) \sin\left(\omega t + \phi_p + \phi_2\right) \end{aligned} \tag{15}$$

where A is the amplitude of the plasma leg signal, B is the amplitude of the reference leg signal, ω is the operating frequency of the Gunn diode, ϕ_1 is the phase shift due to dispersion in reference leg, ϕ_2 is the phase shift due to dispersion in plasma leg, and ϕ_p is the phase shift due to dispersion in the plasma. If the rate of change in the phase shift (i.e. sweep ramp frequency) is much slower than the operating frequency and $B = A$, the time-averaged signal to be detected is

$$S(t) = \langle |M(t)|^2 \rangle \propto 2A^2 \cos^2\left(\frac{\phi_1 - \phi_p - \phi_2}{2}\right) \tag{16}$$

The mixer output is tuned by changing the voltage range of Gunn diode sweep, until the output signal has a desired shape, as shown in Figure 16(c), such that the time-

dependent phase shift $\Delta\phi(t)$ can be described with a constant beat frequency:

$$S(t) \propto \cos^2(\omega_{beat} t)$$

$$\omega_{beat} = \frac{\partial \Delta\phi(t)}{\partial t} = \frac{\partial \omega}{\partial t}\frac{\partial \Delta\phi(t)}{\partial \omega} = \frac{\partial \omega}{\partial t}\left(D\frac{\partial k_g}{\partial \omega} + \frac{\partial \phi_p}{\partial \omega}\right) \tag{17}$$

Here k_g is the wavenumber in the interferometer waveguide, D is the path length difference between the reference leg and plasma leg.

Note that $\frac{\partial \Delta\phi(t)}{\partial \omega}$ is the definition of group delay τ_g, which can be measured by comparing the ramp signal and the interferometer output.

The Gunn diode frequency has linear relation with the input voltage in the range that we are operating. Therefore $\partial\omega/\partial t$ is a constant. By adjusting the Gunn diode sweep and proper calibration in vacuum, $(\partial\omega/\partial t)(D\partial k_g/\partial\omega)$ is set to a constant as well.

The group delay is therefore only due to the phase shift in plasma [83]:

$$\tau_g \propto \frac{\partial \phi_p}{\partial \omega} \tag{18}$$

Using Equation 14, we obtain a linear relation between the time delay and the line-integrated plasma density:

$$\tau_g \propto \frac{e^2}{2c\varepsilon_0 m_e \omega^2}\int_0^L n_e(l)dl \tag{19}$$

To measure τ_g, the mixer output and the Gunn sweep are filtered by a bandpass filter with 1 MHz central frequency, before sent to a phase detector. The detector calculates the time delay between the Gunn sweep peaks and the mixer output peaks.

While the interferometric measurement only provide line-integrated data, it is non-intrusive and the analysis require little assumptions. It can be used to calibrate more spatially resolved probe such as Langmuir probe and hairpin probe, whose density measurement needs sheath correction. In our experiments, we compare the interferometry data to the probe data summed over corresponding locations to determine correction

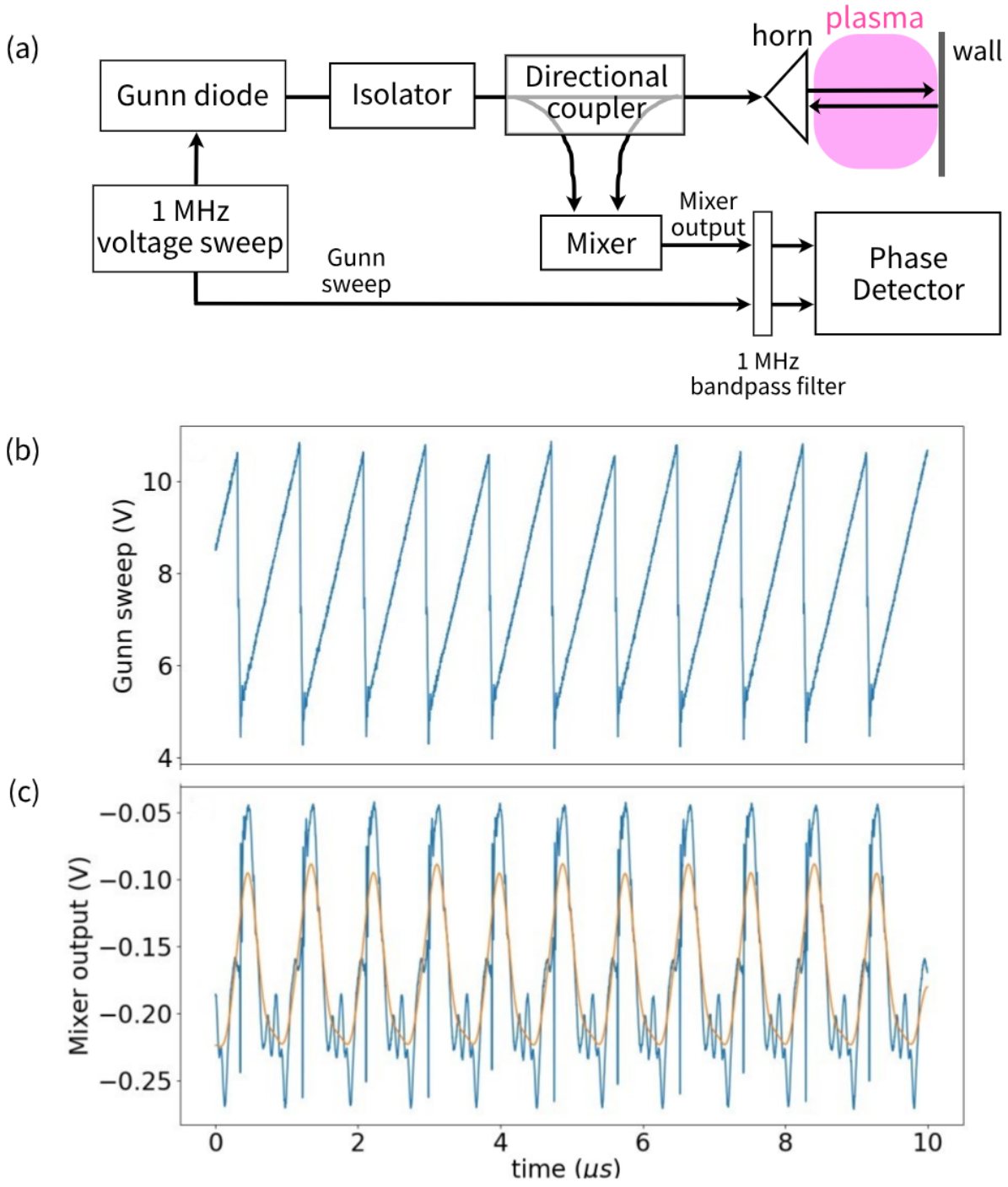

Figure 16: Schematic of the Michelson interferometer setup. (a) The circuit diagram. (b) The input ramp voltage to the Gunn diode. (c) The mixer output, raw (blue) and Gaussian smoothed (orange).

terms (Equation 9), and thus calibrate the probes.

3 Positive Ion Motion Above A Biased Wafer

3.1 RF sheath near a biased surface

In ion bombardment process, positive ions are accelerated from the bulk plasma through the presheath and sheath produced by the RF bias on the wafer [84]. The geometry of a biased electrode in a ICP device is shown in Figure 17, with the time-averaged potential in the plasma plotted on the right. In our device, the electrode is biased with a sinusoidal waveform at 1 MHz. A blocking capacitor prevents DC current and charging on the wafer. The plasma potential in the bulk plasma is slightly positive. The substantial potential drop across the sheath accelerates the ions to vertically bombard the wafer.

As shown in Figure 17, in most chamber geometry the RF bias generates a negative DC bias V_{dc} on the wafer [2]. The presence of V_{dc} is one of the major reason RF is used for surface processing. It provides net ion acceleration towards the surface, while the RF skin effect prevents excessive damage to the surface.

The value of V_{dc} depends on several plasma parameters as well as chamber geometry. In general, a higher pressure and consequently smaller electron mean free path result in lower $|V_{dc}|$. Similarly, higher RF source power and plasma density also lead to lower $|V_{dc}|$, as the blocking capacitor does not have sufficient time to charge up and deforms the bias waveform. [85, 86]. Chamber geometry, such as the ratio of electrode area to wall area also plays important role in forming the self-bias. A larger electrode to wall area result in lower $|V_{dc}|$ [87].

For ideal plasma processing, the ion energy distributions (IEDs) and angle distributions (IADs) should be as narrow as possible, concentrating at the desired energy and normal incidence. The angular distribution can be broadened by elastic collisions along the path, as these momentum transfers create transverse components of the ion velocity at the sheath edge. The thermal energy from the ion creation process may also introduce transverse component to the velocity. Charge-exchange inelastic collisions near the sheath can reduce the ion energy, in addition to broadening the angular distribution. In spite of the importance of the ion trajectory from bulk plasma to wafer, there have been

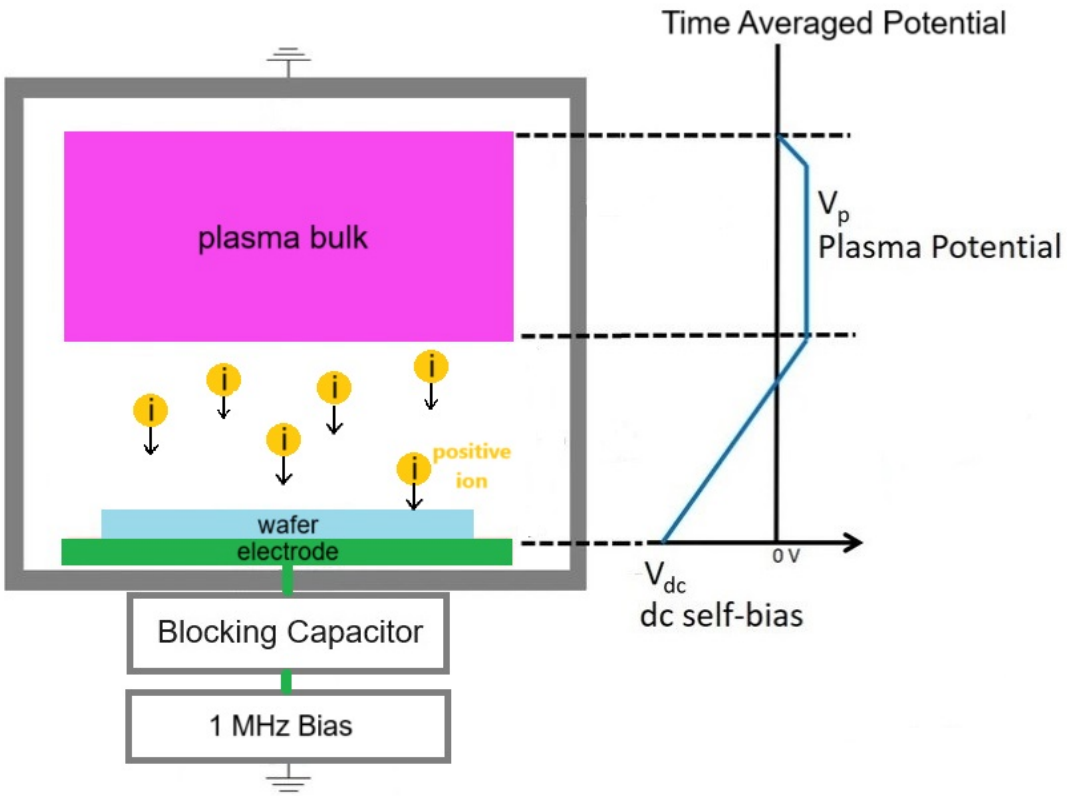

Figure 17: Diagram of a biased electrode in ICP. The DC component (time-averaged value) of the potential inside the plasma is plotted on the right. The sizes of the sheath and the bulk are not plotted in scale.

few direct measurements of the ion velocity and angle on this path.

Figure 18 shows the one dimensional electron and ion density in a collisionless sheath near a biased electrode. Quasi-neutrality ($n_i = n_e = n_0$) holds in the main plasma region and the presheath. At the sheath edge, ions that satisfy Bohm criterion are accelerated to the electrode. The ion density decay from the sheath edge to the electrode surface follows the energy conservation and continuity of ion flux, and has the form $n_i = n_0\sqrt{1 - \frac{2e\Phi}{m_i u_s^2}}$ (Φ is the potential in sheath region, m_i is the ion mass, u_s is the ion velocity at the sheath edge). The electron density n_e decays by the Boltzman relation: $n_e = n_0 e^{e\Phi/kT_e}$, where kT_e is the electron temperature. The Poisson equation for Φ, n_i and n_e has a solution only if u_s is greater than the Bohm velocity $c_B = \sqrt{kT_e/m_i}$, which necessitate the existence of a presheath [84].

The dynamics of the sheath is sensitive to various parameters such as surface bias and ion species to satisfy the boundary conditions. The boundary between sheath and

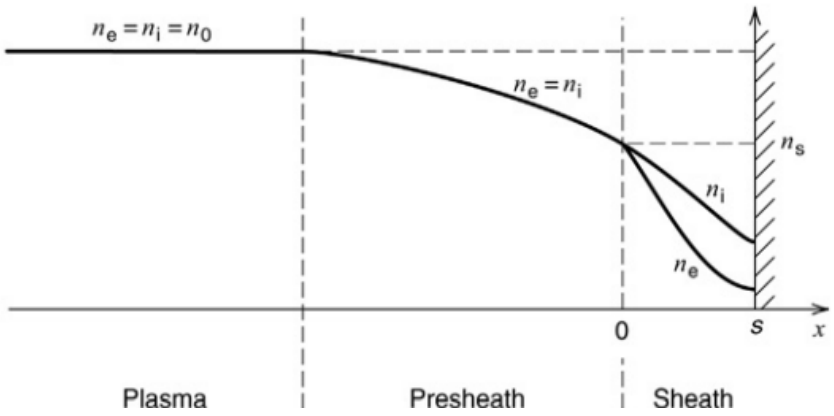

Figure 18: Diagram of specie density in the sheath region near a biased electrode. From Lieberman and Lichtenberg [84].

presheath can be ambiguous in low temperature plasma. Conventionally, it can be defined (1) by particle composition, as the edge of the electron free region as shown in Figure 18, (2) by potential profile, as the edge of the plasma potential as shown in Figure 17, or (3) by ion energy, as the edge where the positive ion velocity towards the surface is equal to the Bohm velocity [88].

In ideal situation, these three definitions mathematically agree with each other. Our experiment directly measured ion energy, and naturally we used the last definition to find our sheath boundary.

In the simpler case of a DC bias, Child-Langmuir law predicts the sheath size s to have a 3/4 power dependence on the bias sheath voltage V_{sh} [89]:

$$s = \frac{\sqrt{2}}{3} \left(-2V_{sh}\right)^{3/4} \tag{20}$$

The Child-Langmuir law are derived under the assumptions that (1) the ions are cold ($T_i \ll T_e$), (2) the sheath is electron-free and collisionless ($\upsilon_i \tau_i \ll 1$, υ_i is the ion collision frequency and τ_i is the ion transit time through the sheath), (3) energy at the sheath boundary is negligible compared to the energy gained in sheath ($kT_e/e \ll V$), (4) electric field is zero at the sheath edge, and (5) the plasma has quasi-neutrality in the bulk and the presheath. These are generally true for low density low temperature plasma in touch with a high bias voltage. The Child-Langmuir law can be used as an lower limit of the sheath size, as analytical approach often shows a thicker sheath [84, 89].

When the bias is oscillating at RF, the sheath geometry and the shape of IEDs depend on the bias frequency f. The low and high RF regime is usually set apart by comparing f to the ion transit time τ_i. In an unbiased sheath, τ_i is simply the inverse of ion plasma frequency. In a biased sheath, τ_i can be estimated from the Child-Langmuir law [90]:

$$\tau_i = 3s\sqrt{m_i/(2eV_{sh})} \tag{21}$$

where s is the sheath thickness, m_i is the ion mass and V_{sh} is the sheath voltage. When the bias RF period is large compared to τ_i ($\tau_i \ll \tau_{rf}$), the bias voltage oscillation is slow compared to the ion motion in the sheath, and therefore ion energy is able to vary with the bias voltage in time. The sheath dynamics is able to keep up with the bias waveform, and therefore the thickness should also varies at the same frequency, as shown by various numerical models [88, 91]. The resulting IED is a bimodal distribution with a low energy peak and a high energy peak. The width of the energy split corresponds to the maximum potential drop across the sheath.

For $\tau_i \gg \tau_{rf}$, ions experience multiple cycles of bias oscillation when traversing the sheath, therefore the energy dispersion in IED decreases and the peaks converge to reflect the time-averaged sheath potential $\overline{V_{sh}}$. The width of the split is proportional to $\overline{V_{sh}}$ and inversely proportional to tau_i [92]. Experiments presented here are conducted in low frequency regime, with $\tau_i/\tau_{rf} \approx 0.13$.

In experiments, ion incident angles can be directly inferred from the etch profile, usually obtained by cutting the etched wafer and taking scanning electron microscope (SEM) image of the cross section [93, 94]. Probes sensitive to ion flux and energy better parameterize the plasmas, but often find difficulty in isolating the signal from the background RF. Retarding field energy analyzer, modified to be used in the presence of high voltage RF bias, has been a popular way to measure the ion energy distribution function [35–41]. Specie-resolved measurement can be obtained by further combining the energy analyzer with a mass filter or mass spectrometer [39–41]. Laser based non-intrusive diagnostics, such as cavity ringdown spectroscopy [42, 43] and laser induced fluorescence (LIF) [44–50], captures velocity information of a single ion species through Doppler shift

and broadening.

LIF has the advantage of providing good spatial resolution with the use of a high resolution camera, and temporal resolution with the use of a short-pulsed laser. Direct images of the ion motions can be obtained, making LIF an ideal tool for studying ion transport in small regions. However, LIF measurement is only effective in low density plasma that has enough population of metastable ions.

3.2 Laser Induced Fluorescence Method on Ar^+

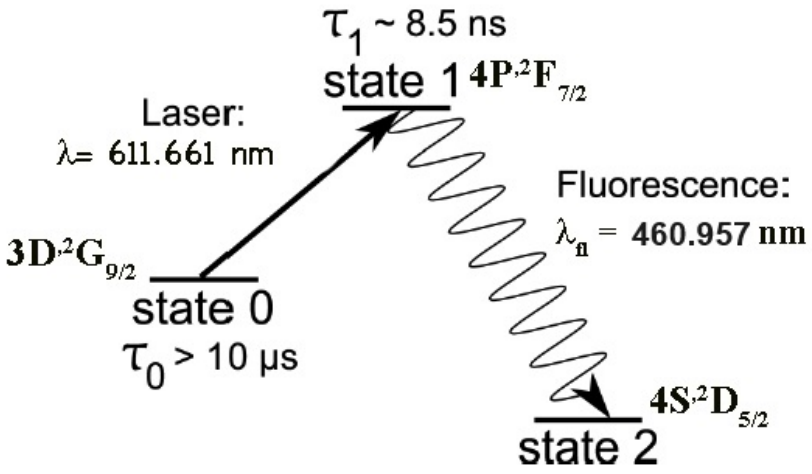

Figure 19: Diagram of the Ar^+ LIF scheme. Metastable state 0 is 19.2 eV above the ground state of the ion with the Ar ionization energy being 15.6 eV. In a plasma with T_e = 4 eV less than 3 % of the electrons are at this energy for multi-step ionization. This results in few ions in state 0 and weak resultant optical signals.

Laser induced fluorescence (LIF) technique makes use of line transition and Doppler shift to study ion movement. In an LIF event, an ion at some metastable state absorbs a incident photon and jumps to a higher state. Then it quickly decays to a stable state and emits a fluorescence photon. Since the incident photon and the fluorescence photon have different wavelengths, fluorescence light can be easily distinguished and recorded with the help of a narrowband optical filter. When an ion has a velocity component with respect to the laser propagation, it experiences a Doppler shifted incident laser, and its LIF event happens at a correspondingly shifted incident wavelength. By scanning a narrowband tunable laser across a range of wavelengths, ion velocity can be resolved. Ion

velocity distribution, which is proportional to the line shape of the fluorescence emission, can thus be measured [44, 46].

With the probability of absorption scaling with $|\vec{k} \cdot \vec{v}|$ ($\vec{k}$ is the photon wavevector, $\vec{v}$ is the ion velocity), the LIF line shape mainly corresponds to the 1D velocity component parallel with the interrogating laser. Multi-dimentional spatially resolved measurement can be achieved with the use of multiple laser entry angles and a fast, high resolution camera.

To observe Argon ion motion, we chose an incident laser center at $\lambda_0 = 611.661$ nm [46, 48]. In the rest frame, it pumps Ar^+ from the metastable state 0 ($3d^2G_{9/2}$) to the metastable state 1 ($4p^2F_{7/2}$), which then optically radiates at 460.957 nm to state 2 ($4s^2D_{5/2}$), as shown in Figure 19. State 0 is 19.2 eV above the ion ground state and is populated by electrons in the tail of the distribution function directly impacting ground state ions. After being pumped by the laser, state 1 ions have a 67% branching probability of decaying to state 2 and emitting a photon at 460.957 nm, easily distinguishable from the pumping laser. A laser tuned to $\lambda = 611.661$ nm excites metastable ions at rest, while the moving ions are excited by the appropriate Doppler shifted wavelength. During our experiment, the tunable laser was shifted in increments of 0.001 nm, typically across a range of $\lambda_0 \pm 0.15$ nm which corresponds to an ion energy range of roughly $\pm$ 1600 eV.

The laser excited state 1 ($4p^2F_{7/2}$) has a measured lifetime of 8.5 ns [95], and stays relatively free from collisional loses in the low temperature background plasma ($T_e = 4$ eV). On the other hand, the lifetime of state 0 ($3d^2G_{9/2}$) was measured to be greater than 17 μs in comparable experiment conditions [96], and so can be quenched by collisions, dominantly charge exchange, at frequencies greater than 6×10^4 s^{-1}. Goeckner *et al.* [50] experimentally found that significant quenching occurs at pressures above about 0.7 mTorr. We observed a significant drop in the LIF signal above a neutral pressure of 1 mTorr, and chose to perform the experiments at around 0.5 mTorr.

IED is constructed from the LIF signal corresponding to the absorbing laser wavelength. The ion velocity $v_\parallel$ parallel to the laser propagation is related to the Doppler shifted absorbing wavelength by $\lambda - \lambda_0 = v_\parallel / c$.

In energy space, the conversion is

$$E_{\parallel} = \frac{mc^2}{2}\left(\frac{\lambda - \lambda_0}{\lambda_0}\right)^2 (J) = 1.86 \times 10^{10}\left(\frac{\lambda - \lambda_0}{\lambda_0}\right)^2 (eV) \tag{22}$$

where m is the mass of an argon atom, $E_{\parallel}$ is the ion energy parallel to the absorbing laser wavelength, c is the speed of light in SI units and $\lambda_0 = 611.661$ nm.

3.3 Experimental Setup

The chamber pressure was kept at 0.5 mTorr. The feed gas was a mixture of (purity 99.999% Ar and O_2 at a ratio of 95:5. The small amount of O_2 was needed because the Ar ion bombardment produces sputtered Si, which would coat the window. O_2 is able to react with Si atoms and remove them as volatile gas through the pumping system. The amount of negative ions do not affect the sheath-wafer interaction [86].

The plasma reproducibly reignited when the ICP was pulsed on and off at pressures greater than 5 mTorr, but had difficulty igniting for the first time at 0.5 mTorr. To overcome this, we started at a higher pressure to ease breakdown, and then decreased the pressure to the desired value. The ICP was pulsed between high and low powers (550 W and 125 W) so that the plasma was never completely extinguished. There was no visible breakdown during the low power interval, which we treated as plasma afterglow. Measurements were performed with the wafer bias either on or off, when ICP was at high power or in the afterglow.

The optical setup and triggering scheme are shown in Figure 20. The laser light was produced by a dye laser (Sirah CSTR-D-532) pumped by a Nd:YAG laser (Spectra Physics Pro-230) with a center wavelength of 611.661 nm, linewidth of 0.000136 nm and pulse length of 8 ns. It was transmitted via an optical fiber from the laser room to the adjacent ICP reactor room, and made into a sheet of light through a combination of cylindrical lenses. A 461 $\pm$ 0.5 nm narrow bandpass filter and a CCD fast camera (PCO Dicam C1) are used to capture the LIF signal from a window on the side of the chamber transverse to the beam path.

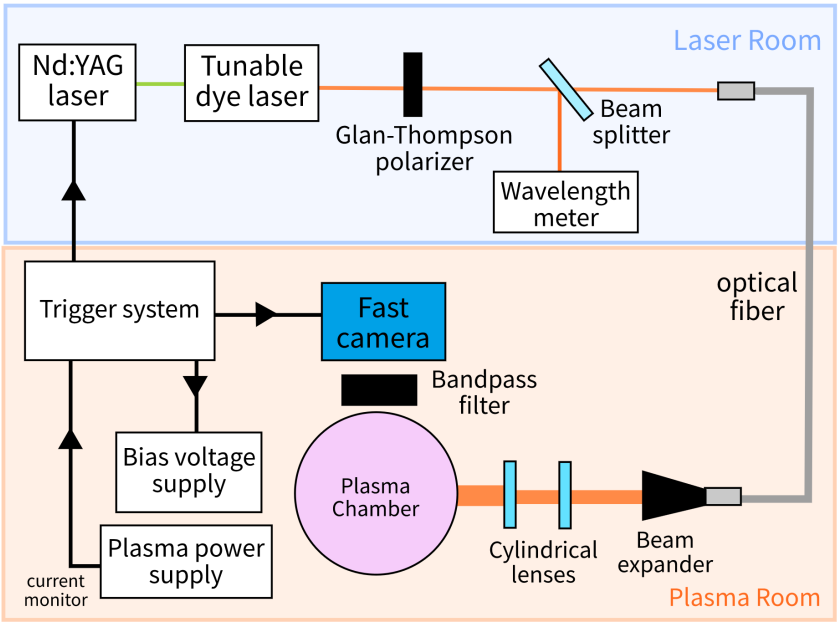

Figure 20: Diagram of the experimental setup illustrating the optical path. Here the beam is shown to enter the plasma chamber horizontally. A group of mirrors can be inserted in the beam path to make the beam enters vertically towards the wafer.

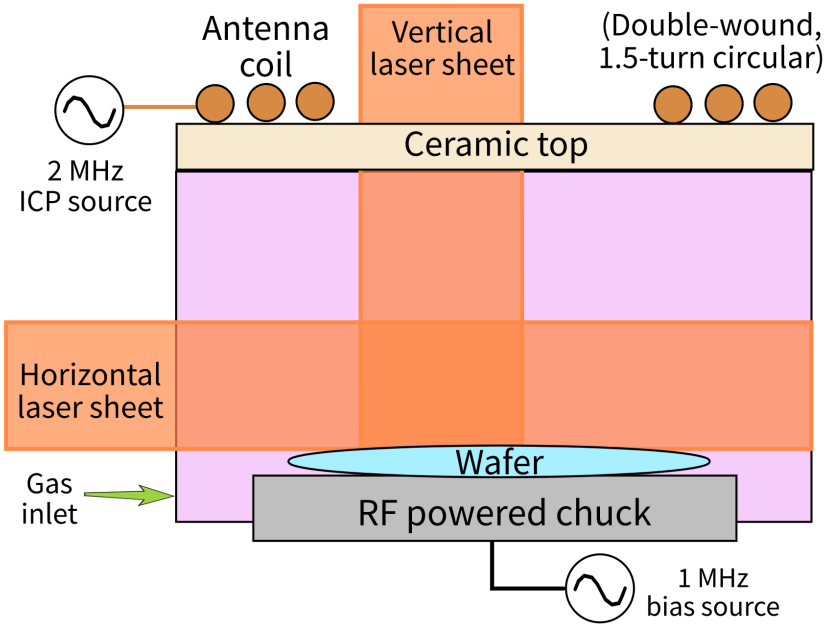

Figure 21: Side view of the plasma chamber (not to scale). The reader's perspective is the same as the fast camera's. The laser sheet can enter the chamber horizontally above the wafer, or vertically towards the wafer by placing two 45° mirrors in front of the horizontal beam.

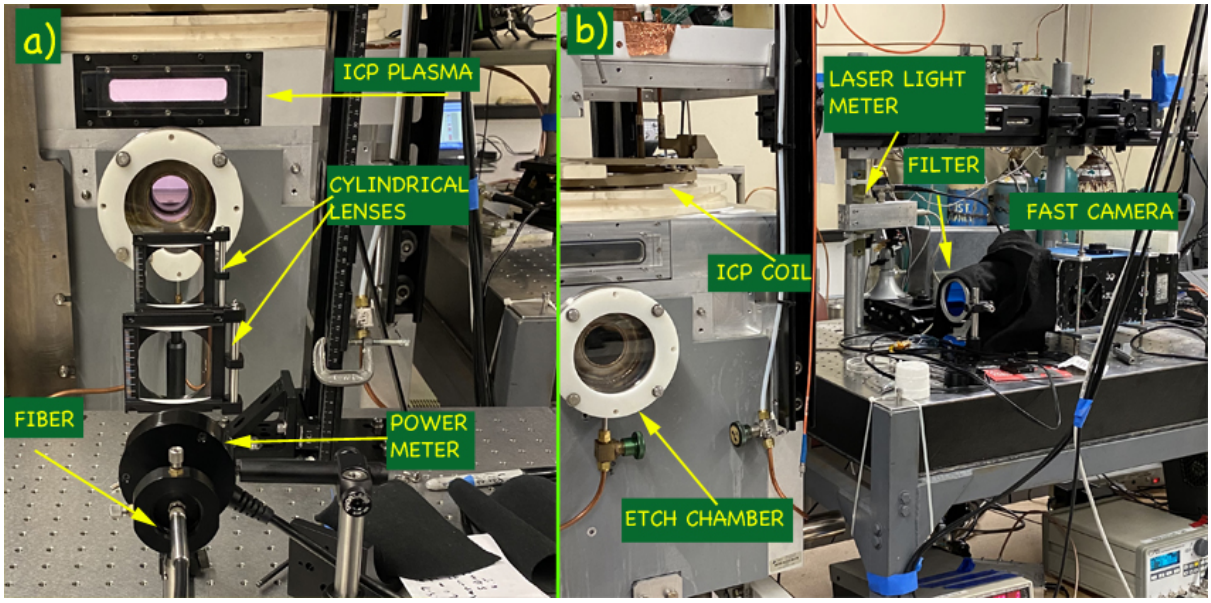

Figure 22: Photo of the experimental setup (a) on the side of the incoming laser beam and (b) on the side of the camera.

Figure 21 details the entry of the laser into the chamber, horizontally (parallel to the wafer) or vertically (towards the wafer). A photograph of the setup is shown in Figure 22. The data were recorded alternatively with horizontal and then vertical beams under the same condition. Thus ion transport and ion flow patterns in two dimensions were measured and calculated. Optical access limited the field of view to a maximum of 2.5 cm vertically $\times$ 5 cm horizontally. To capture LIF data above both the edge and the center of the wafer, separate data runs were conducted and the camera was re-positioned accordingly.

LIF data were acquired at three different setup conditions:

(1) when the 2 MHz ICP was on high power (i.e. in the plasma glow) and the 1 MHz wafer bias was switched on;

(2) when the ICP was on high power and wafer bias was off;

(3) when the bias was switched on after the ICP switched to low power, i.e. in the plasma afterglow.

Figure 23 illustrates the timing of case (1) and (3), while (2) is just (1) without bias. Each ICP high power pulse had a duration of 12 ms, at a 10 Hz repetition rate. The bias voltage on the wafer plate turned on at 7 ms after the start of the ICP high power and

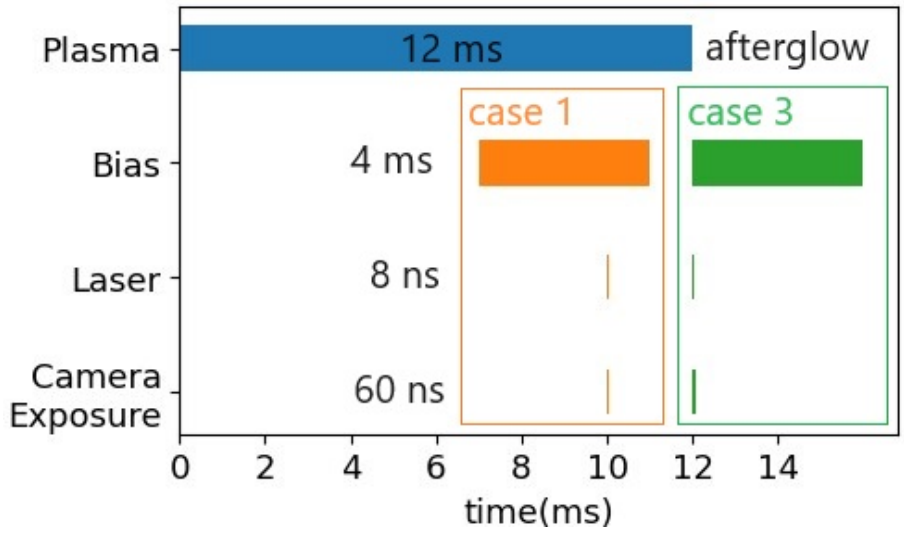

Figure 23: Timing chart of the data acquisition during one plasma pulse, for case (1) and (3).

continued for 4 ms in case (1). For both case (1) and (2), the 8 ns laser pulse fired at 10 ms.

Figure 24 is a timing diagram for the afterglow experiment. For case (3) in the afterglow, the bias turns on 10 μs after the ICP high power pulse, and the laser fires 30 μs after the high power pulse. The time axis is relative to the laser firing. The photodiode integrates the incident laser light, and its derivative gives the laser intensity in arbitrary units. On the time scale of the laser pulse, the photodiode signal immediately rises, allowing us to determine the exact timing of the laser firing. The coil voltage is measured across the RF coil situated outside the chamber. The photodiode captures light from both plasma and laser. As the coil voltage switches to the low state (1/4 of the high state), the plasma density starts to decay, as indicated by the dropping photodiode signal. The laser gives a sudden rise to the signal.

On top of the main trigger, the laser firing time can be fine-tuned with respect to the bias voltage, and therefore the LIF measurement can be phase resolved with a resolution of 8 ns out of the 1 μs RF bias period. The camera exposure lasted 60 ns and was triggered in such a way that the LIF emission resulting from the entire laser pulse was captured.

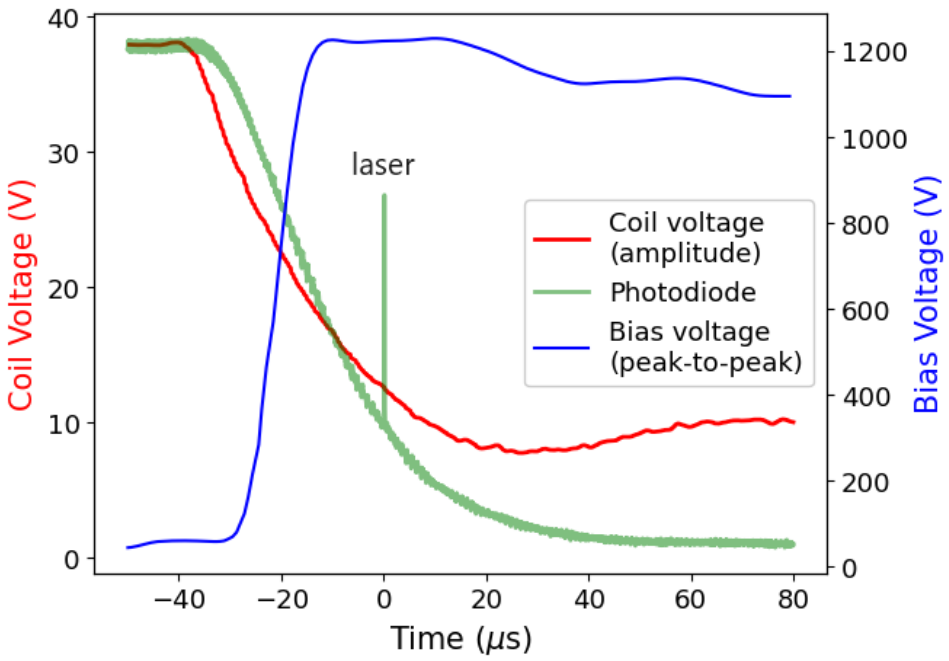

Figure 24: Detailed timing of case (3) in afterglow, showing the ICP coil voltage amplitude (red), peak-to-peak applied bias voltage (blue) and photodiode signal (green).

3.4 Data Acquisition and Image Processing

The raw camera data was automatically binned over 4 adjacent pixels that were then averaged into a single pixel. A typical image has 752 pixels along the wafer and 551 pixels above the wafer. Each pixel contains a 12 bit number. At each scanned wavelength, data consisting of about 2.0×10^5 photons per acquired image at the peak wavelength was collected and averaged over 500 to 1000 acquired images. All the raw camera images were stored in HDF5 files as groups of 2D arrays, then read into Python for further image processing using NumPy with SciPy image processing.

The view of the camera is calibrated with a 2D graticule placed at the location of the laser sheet path. The camera is adjusted until the graticule is on focus, and a photograph was taken to determine that each (x, y) square pixel was 0.018 cm wide in the image plane.

There were substantial background lights despite the narrow band filter set in front of the camera. The sources include photons from the metastable state due to population of state 1 by electron impact, camera heat noise, and plasma emission that entered the bandpass filter at an angle. These are carefully subtracted at every laser wavelength as

illustrated in Figure 25.

The images in Figure 25 document the processing of a raw LIF signal taken with a horizontal laser beam at the line center wavelength (corresponding to zero parallel velocity) in one representative case. After acquiring the averaged LIF signal (Figure 25(a)), the camera was triggered 200 ns later to capture an averaged background image(Figure 25(b)). 200 ns is well beyond the laser pulse (8 ns) and the lifetime of the excited state (8.5 ns). Note that Figure 25 uses different color scales for better visual effect. (b) is much dimmer than (a) on an absolute scale. The background was acquired at every wavelength, and subtracted pixel-by-pixel from the LIF signal during the data analysis.

A typical data run spanned 450 wavelengths taking approximately 10 hours. The background subtracted LIF images were smoothed with a Gaussian filter over 4 pixels and then a Butterworth filter was applied to remove high frequency noise.

3.5 Results

3.5.1 Self-bias and Ion Energy

The bias RF voltage is a sinusoidal waveform

$$\frac{1}{2}V_{pp}\sin(2\pi ft) + V_{dc} \tag{23}$$

where V_{pp} is the peak-to-peak voltage, f is 1 MHz and V_{dc} is the DC self-bias developed on the electrode surface, as depicted in Figure 17.

Before the LIF experiment, the exact voltage on the wafer was investigated. A metal plate was placed at the center of the wafer and its voltage was measured by a high voltage probe attached to a coaxial feed-through. Assuming the setup does not affect the sheath potential and the capacitance of the metal plate is negligible, this is practically a measurement on the sheath voltage $V_{sh} = V_T - V_p$, where V_p is the plasma potential, and V_T is the voltage on the electrode ("target" voltage).

The time-averaged V_p was previously measured by an emissive probe. Close to the wafer, time-averaged V_p is less than 10 V. Significant oscillations from the source RF power

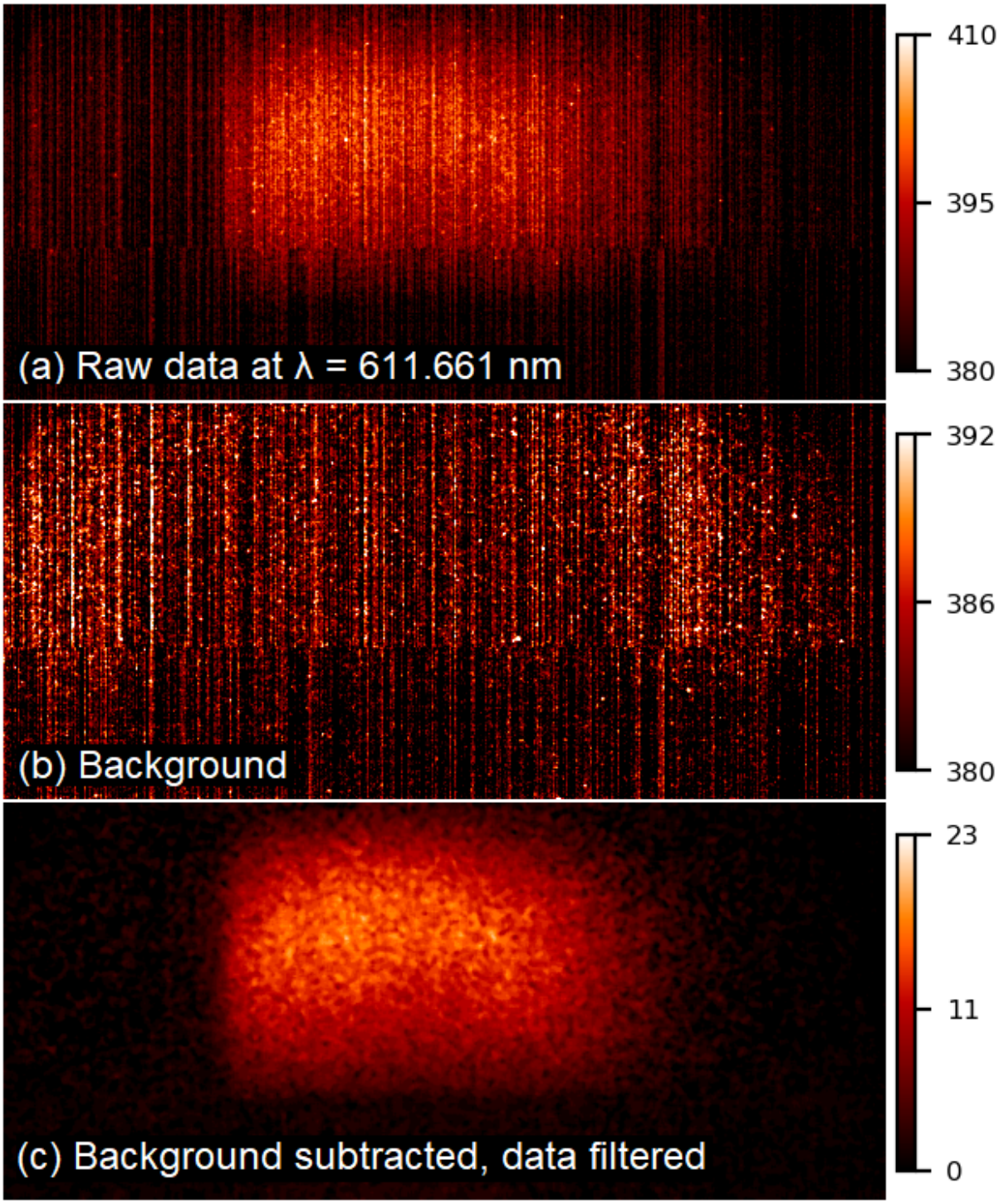

Figure 25: Sample images to show the image processing procedure. (a) The direct output from the CCD camera taken during the laser firing at 611.661 nm. (b) The background photo taken 200 ns after (a). (c) The post-processed image, obtained by subtracting pixel by pixel the 7(b) from that in 7(a) and applying a Butterworth filter and Gaussian smoothing over 5 pixels.

(2 MHz) is confined to only a few centimeters below the antenna by plasma shielding. Therefore in this experiment V_p can be viewed as a constant [60]. It will be shown later that during most part of the bias RF cycle, the measured amplitude of V_T is much larger than V_p, so the instantaneous potential drop across the sheath can be approximated by $V_{sh} = V_T$ for most period of time. The largest energy gained by ions traversing the sheath is then eV_T.

In general and rigorous terms, ions react to a "damped" sheath potential V_d damped by the ion transit time. The relation to the instantaneous sheath potential is [97]:

$$2\pi f\tau_i \frac{\mathrm{d}V_d}{\mathrm{d}(ft)} + V_d(ft) = V_{sh} \tag{24}$$

For small $2\pi f\tau_i$, the damping effect is minimal and $V_d \approx V_{sh}$. Ions react to the instantaneous change in the sheath potential. It is safe to say that measurement on V_T is a direct assessment on ion energy gain.

The exact value of $V_{sh} = V_T - V_p$ can be calculated analytically from the external applied bias voltage and the geometry of the chamber using equivalent circuit model [90, 98]. The simplest equivalent circuit for RF sheath near a biased electrode in ICP typically looks like Figure 26 [98]. C_b is the blocking capacitor, C_{sh} is the sheath capacitance, V_{rf} is the applied RF bias voltage and V_p is the plasma potential in the bulk. The ion current I_i is modeled as a steady current flow to the wafer at the Bohm velocity: $I_i = eAu_Bn$, where A is the electrode surface area and n is the ion density at the edge of the sheath. The resistive flow of electron current I_e through the sheath is modeled as a diode with $I_e \propto \exp\left[(eV_{sh}(t)) \,/\, (kT_e)\right]$. A displacement current I_d flows through C_{sh} balances I_e and I_i so that the net bias effect is sinusoidal.

Some equivalent circuits include further details and components, such as the complete RLC circuit for the blocking capacitor, matching network circuits, separate calculation for sheath-wall capacitance and sheath-wall capacitance, etc. These details are important for fine tuning of the wafer waveform and IEDs.

Figure 27 compares the measured wafer waveform V_T during active glow in case (1) and during the afterglow in case (3) to the applied waveform. The applied waveform was

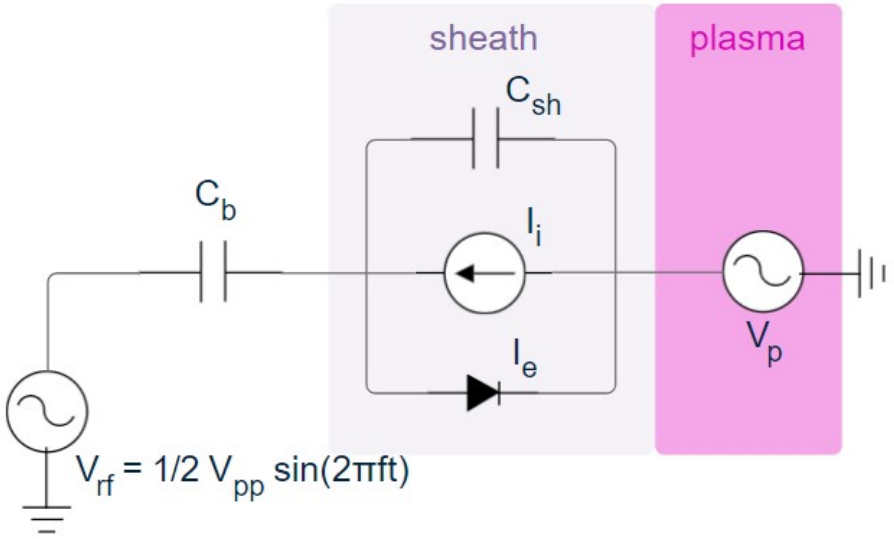

Figure 26: The equivalent circuit of a biased electrode and sheath in ICP.

measured at the external terminal of the bias power supply. In both cases, the wafer waveforms almost exactly follows the sinusoidal shape of the applied waveform, albeit a slight phase change. This is commonly observed [86, 99] due to the blocking capacitor unable to fully catch up with bias frequency. A temporal investigation at the onset of the bias shows bigger distortion and and phase delay on wafer waveform, but the waveform is quickly stabilized to Figure 27 by the tuning network of the blocking capacitor.

The measured V_{dc} in plasma active glow phase is approximately 90% of the RF amplitude: $V_{dc} \approx -0.9(\frac{1}{2}V_{pp})$. The maximum potential during the peak of the cathodic portion of the RF cycle reaches $-0.82V_{pp}$. The positive peak of the waveform shows some small amplitude oscillation due to the thinning sheath which causes changes in sheath capacitance.

According to Equation 21, the ion transit time across the sheath is $\tau_i \approx 0.13\mu$s. Our system is in the low RF regime and therefore ions entering the sheath are largely able to follow the instantaneous voltage waveform, as opposed to responding to the time averaged potential. The most energetic ions are expected to strike the wafer with an energy approaching $0.82V_{pp} \approx 980$ eV.

In afterglow, the plasma density is substantially lower. The bias waveform seems smoother during the positive voltage part, presenting less oscillations. The maximum ion

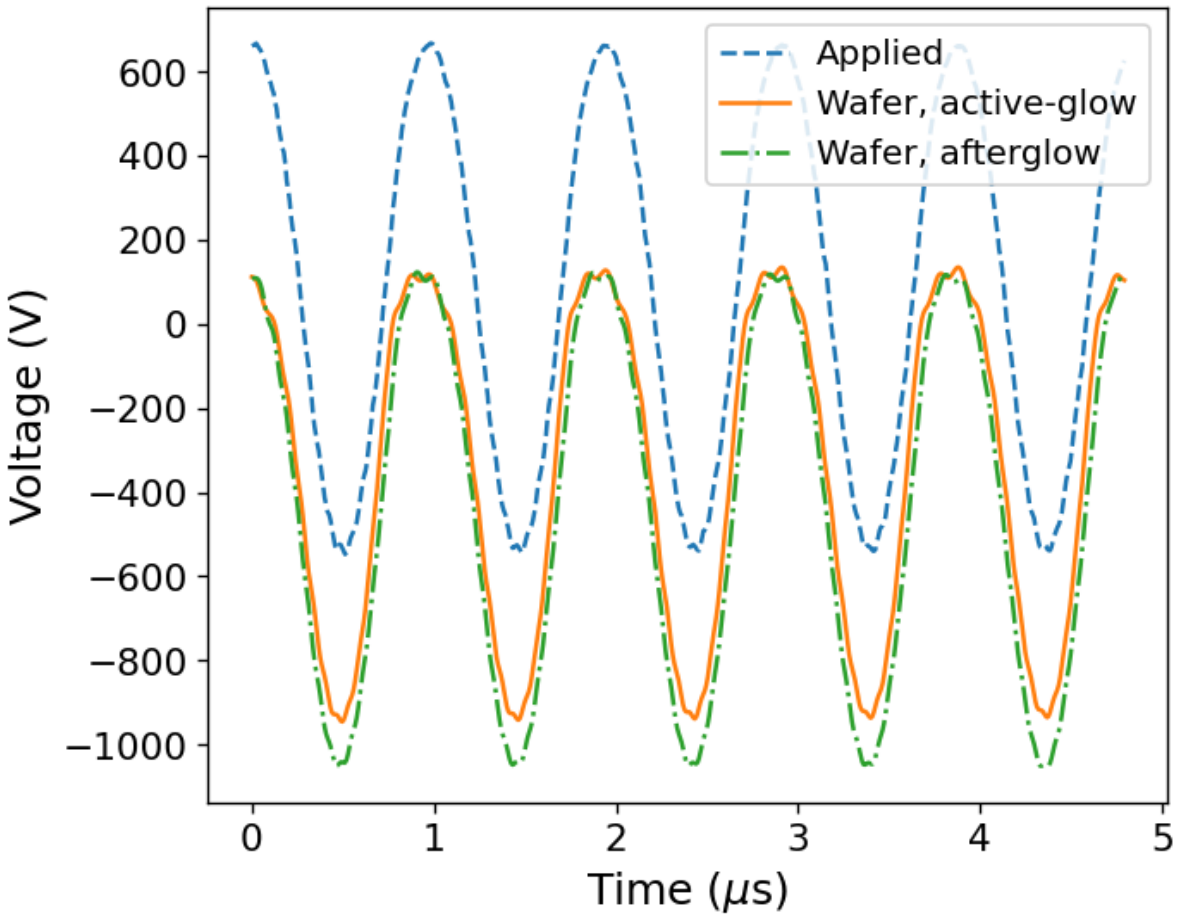

Figure 27: The bias voltage measured on the wafer during the active glow for case (1) (solid orange), during the afterglow for case (3) (dashed dotted green), and the applied voltage (dashed blue). The wafer waveform practically corresponds to the sheath voltage.

energy in afterglow approaches -1050 eV.

After the measurement, the metal plate was taken out from the chamber during the LIF experiment to avoid interfering with the LIF signal and boundary conditions. Since V_T couldn't be monitored simultaneously with the LIF event, the experiments discussed below were all designed and triggered according to the applied voltage V_{pp}.

Ar^+ ions undergo charge exchange collisions with O_2 having a cross section for energies of a few eV of $2-4\times10^{-16}$ cm^2 with rate coefficients of 10^{-10} cm^{3}s^{-1} [100]. For a gas pressure of 0.5 mTorr, the mean free path between charge exchange collisions of Ar^+ with O_2 for a gas temperature of 600 K is above 10 m. Given the size of the chamber, Ar^+ ions are likely not being depleted by charge exchange collisions with O_2. The symmetric charge exchange collision of Ar^+ with Ar at a few eV is about 20×10^{-16} cm^2 which produces a mean free path of about 70 cm [101], increasing to about 150 cm at 100 eV. One might then expect some mild amount of charge exchange that would contribute to thermalizing the low energy part of the velocity distribution.

Representative IEDs for setup case (1) and (2), i.e. with or without bias during the plasma glow, are plotted in Figure 28, 29 and 30. The side of the function corresponding to ions moving towards the wafer is highlighted. The other side of the IEDs are either symmetric or flat.

The positions z = 0 and x = 0 correspond to the surface of the wafer and the edge of the wafer. The x positions are chosen to be far enough from the wafer edge that the plasma is generally uniform along the wafer surface and the distributions don't show significant difference with a change of x.

The distribution functions of ion velocity parallel (horizontal) to the wafer, $f_H(E)$, are shown at a height of z = 0.69 cm (at the edge of the sheath) and z = 4.03 cm (in the bulk plasma) in Figure 28. $f_H(E)$ at both heights are essentially the same with and without a wafer bias. This is as expected since the bias mainly effects vertical ion motion. We only show the no bias case here. Beyond -40 eV, $f_H(E)$ falls completely below noise level (blue region), indicating an absence of high energy ions.

$f_H(E)$ entering the sheath sets a lower limit on the angular spread of ions striking the

substrate. The minimum angle is $\theta = \sqrt{E_T/qV_s}$ where E_T is the transverse energy and V_s is the substrate bias voltage. $f_H(E)$ is symmetric in both negative (inward moving) and positive (outward) moving directions, implying an isotropic distribution. The FWHM (full width half maximum) of $f_H(E)$ is 0.3 eV, which is commensurate with the computed ion temperature for similar conditions.

The vertical IEDs, $f_V(E)$, without a bias at z = 0.67 cm and z = 4.09 cm are shown in Figure 29. The FWHM of the no bias $f_V(E)$ is 0.3 eV, similar to that of $f_H(E)$, which again implies a largely isotropic distribution. Unlike $f_H(E)$, however, $f_V(E)$s show an asymmetry with a velocity component commensurate with the sheath voltage drop directed downwards towards the wafer.

When the bias is applied, $f_V(E)$ broadens, and shows distinct feature near the sheath region. Figure 30 shows a case of $f_V(E)$ with a V_{pp} = -1200 V bias for heights of z = 0.345 cm (sheath), 1.38 cm (sheath edge) and 3.11 cm (bulk plasma), acquired when the applied bias is at the most cathodic phase. At the height of z = 3.11 cm, which is well above the sheath edge, $f_V(E)$ contains ions that are accelerated down the plasma potential towards the sheath. In this reactor, the plasma potential is at its most positive value near the middle of the chamber (z = 9.5 cm) [51]. Close to the sheath edge, $f_V(E)$ extends to higher energies. At z = 0.345 cm, the maximum ion energy (above noise) directed towards the wafer is up to 660 eV.

To further illustrate the effect of RF bias, a 3d contour map of $f_V(E)$ with V_{pp} = -1200 V at all z is plotted in Figure 31, from which Figure 30 can be viewed as cross-sectional slices at selected z values. The presence of the high energy ions is visualized as a "ridge" extending to negative energy (directed towards the wafer) as high as 820 eV. The thickness of the "ridge" in z is 0.3 cm, indicated by the yellow double arrow on the axis, which we approximate as the sheath thickness.

Figure 27 shows that the maximum ion energy for acceleration from the sheath edge is 980 eV. In our experiment no significant LIF signal was obtained beyond 820 eV at the most cathodic phase of the applied bias. This is likely due to the low plasma density very close to the wafer (1 to 2 mm) and ion density scales inversely with ion speed for

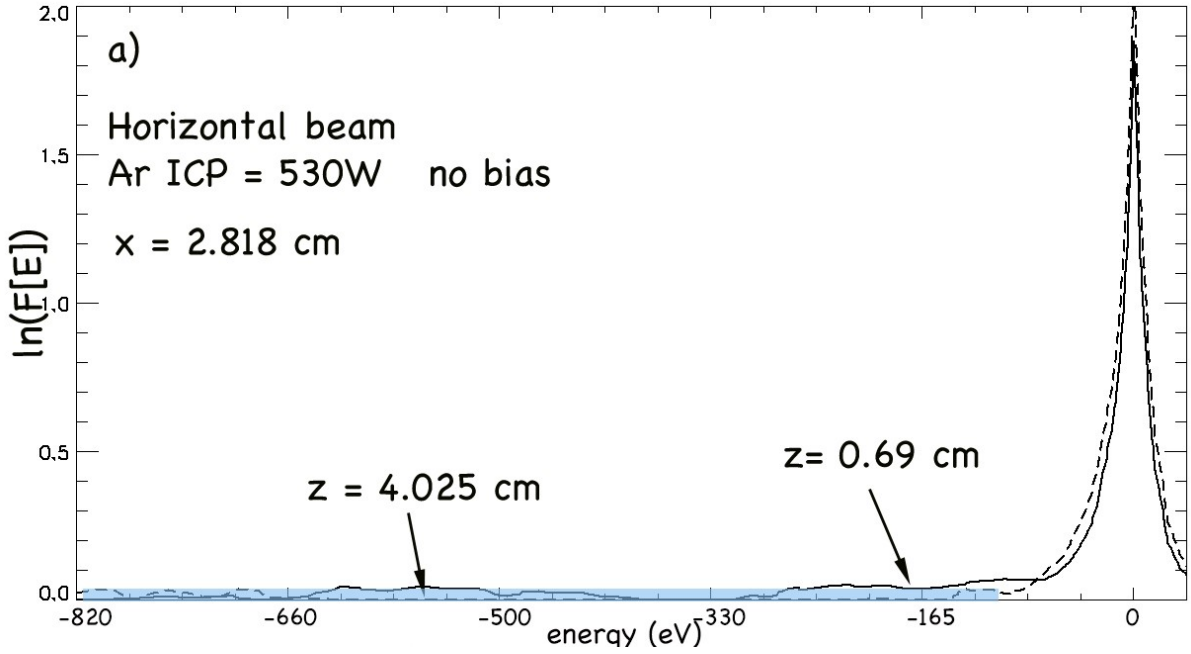

Figure 28: Normalized IEDs of horizontal velocity (along the wafer), plotted on a logarithmic scale. The wafer was not biased. The semi-transparent blue rectangle indicates the noise level.

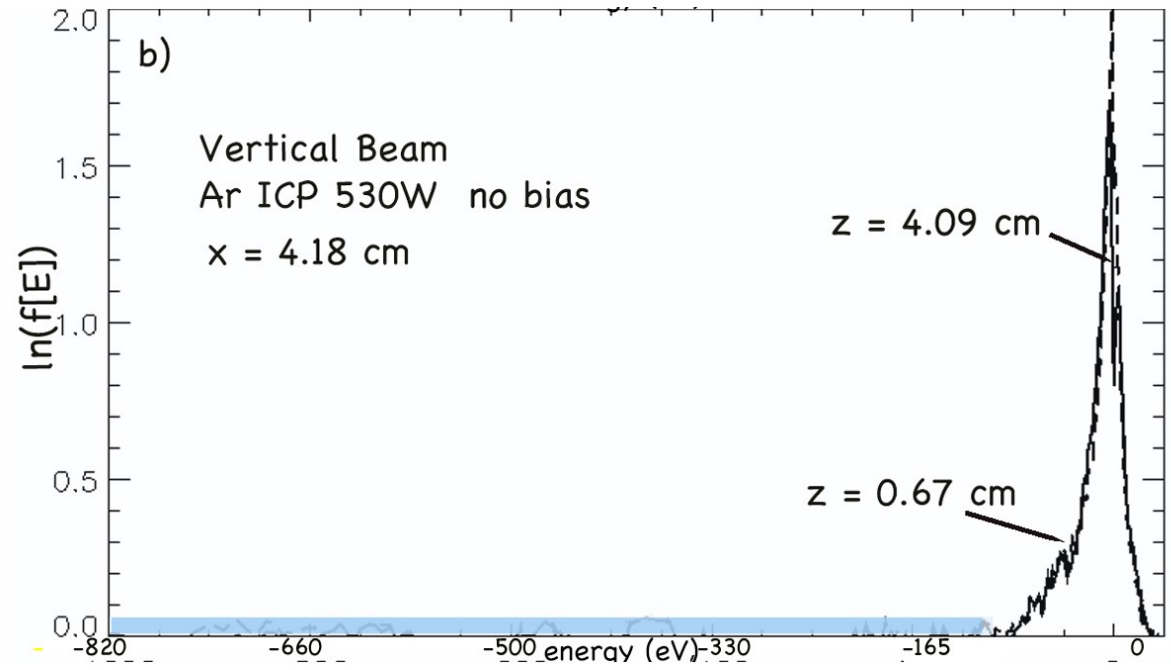

Figure 29: Normalized IEDs of vertical velocity (negative energy means downwards to the wafer), plotted on a logarithmic scale. The wafer was not biased. The semi-transparent blue rectangle indicates the noise level.

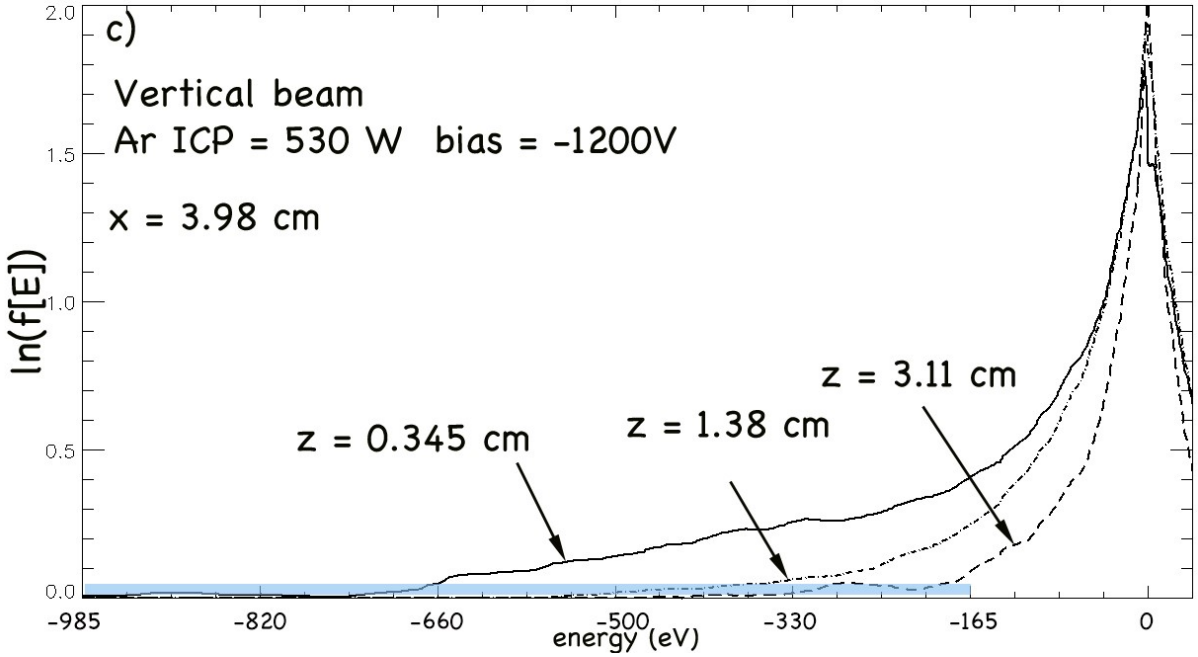

Figure 30: Normalized IEDs of vertical velocity plotted on a logarithmic scale. The wafer was biased at V_{pp} = -1200 V. LIF was taken at the most cathodic phase of the applied RF bias. The semi-transparent blue rectangle indicates the noise level.

a collisionless sheath in which ion flux is conserved. A phase delay between the applied bias voltage and the ion motion is also observed, illustrated in Figure 34. The maximum energy might be easier to detect at a phase other than the most cathodic.

For case (3) in the plasma afterglow, measurements are particularly difficult as there must be sufficient number of electrons to populate state 0 ($3d^2G_{9/2}$) with an excitation energy of 19.2 eV (Figure 20). Collecting a sufficient number of photons to be above noise requires that the electrons in the afterglow are still warm. It was experimentally determined that there was sufficient signal to perform LIF 30 μs after the ICP switched to low power (i.e. 20 μs after the initial bias pulse), and no later than that. The wafer bias pulse was turned on 10 μs after the ICP switched to low power.

$f_V(E)$ as a function of height in afterglow is shown in Figure 32 at x = 4.6 cm. The applied bias of V_{PP} = -1200 V is at the most cathodic phase. As with measurements when the ICP is on high power, $f_V(E)$ is dominated by a low energy component in the bulk plasma (z $\gg$ 0.5 cm). At distances less than 0.5 cm, there is gradual acceleration to about 175 eV. Upon entering the sheath proper ($<$ 0.3 cm), $f_V(E)$ has a high energy component peaked at 880 eV and extending to 985 eV. This value is near the expected

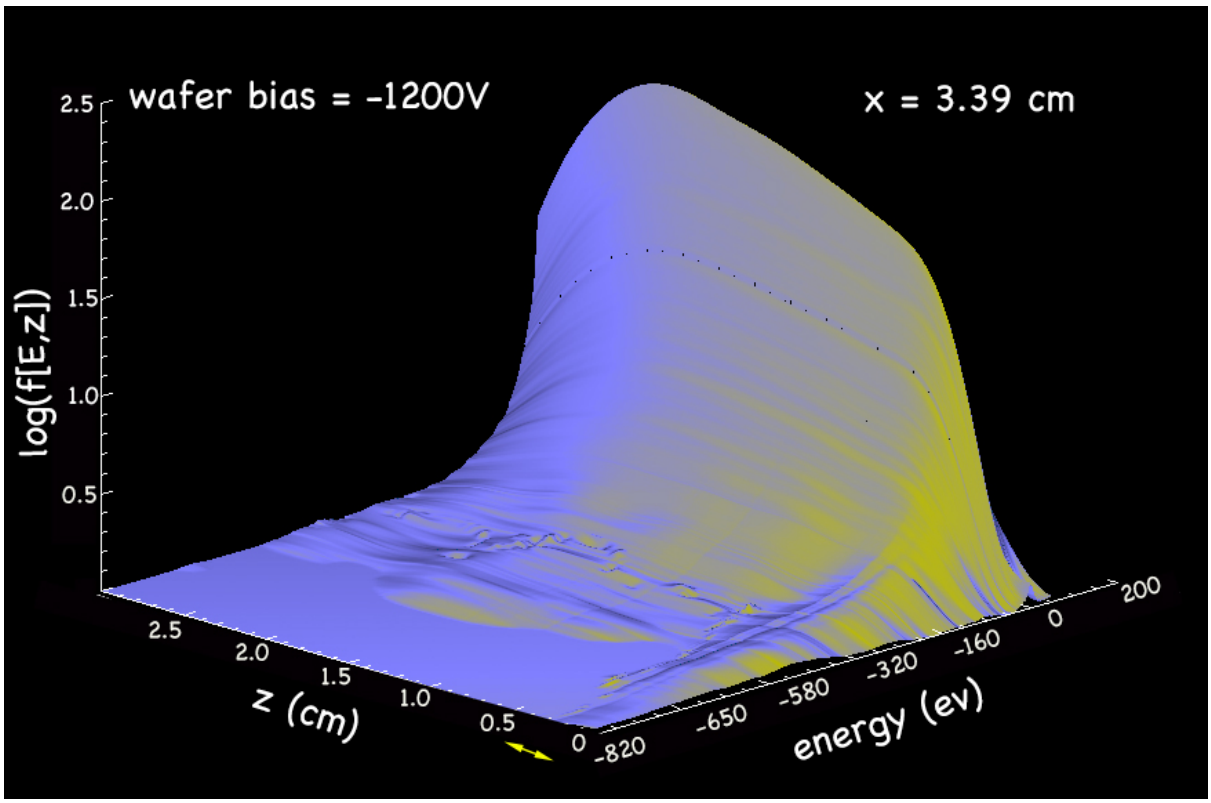

Figure 31: The log of $f_V(E)$ as a function of height z, at x = 3.39 cm and V_{pp} = -1200 V. A yellow double arrow indicates the approximate sheath width. This data is taken at the phase of the RF bias when the applied RF voltage was most negative.

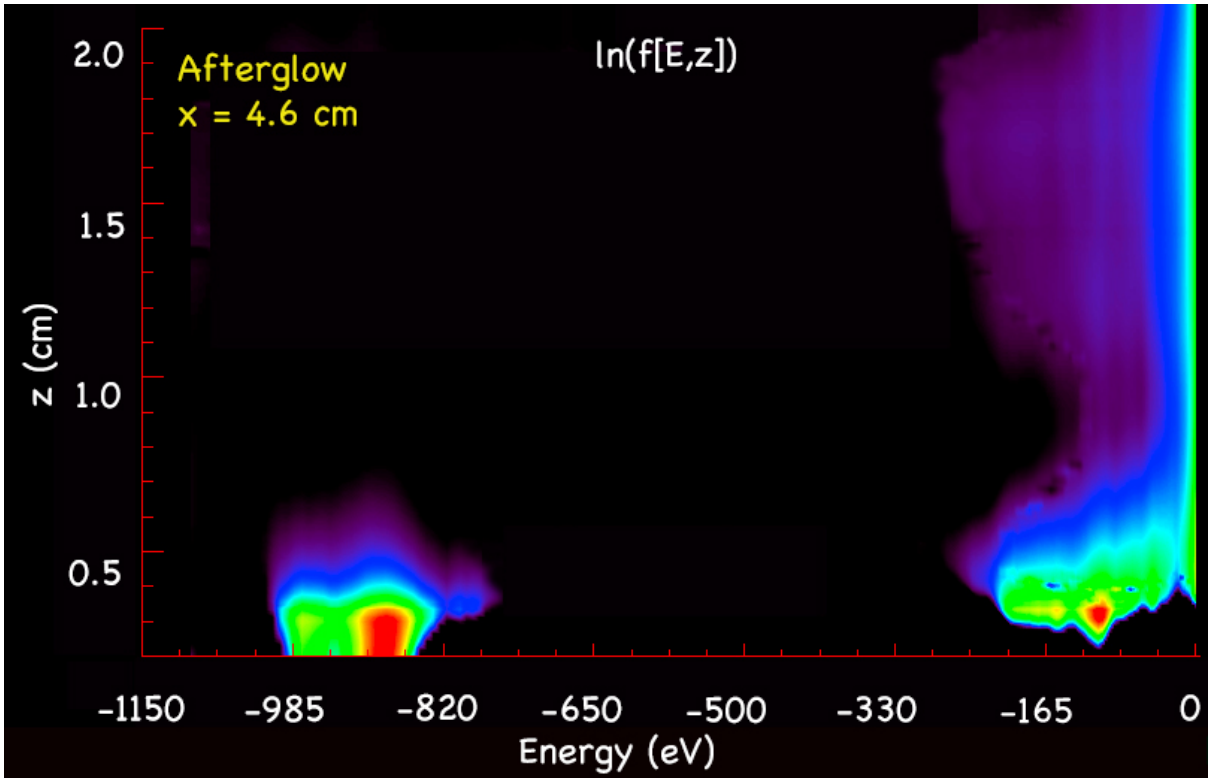

Figure 32: The log of $f_V(E)$ in afterglow as a function of height z,at x = 4.6 cm and V_{pp} = -1200 V. Normalized color bar is shown at left.

maximum energy of about 1 keV.

Compared to case (2), $f_V(E)$ in Figure 32 has a distinctive high energy feature. The fast ions in the sheath region are concentrated in a small band of energies close to the wafer bias, instead of having a smooth tail extending to high energy, as seen in $f_V(E)$ during ICP high power (Figure 31).

3.5.2 Sheath Variation

Apart from the energy-resolved data obtained at the most cathodic phase of the applied bias, the phase-resolved LIF signal was obtained at a fixed excitation laser wavelength.

An RF compensated Langmuir probe measured the background T_e to be 4 eV. The Bohm velocity in this case is $c_B = 3.1 \times 10^3$ m/s. We defined the sheath here by ion kinetics, i.e. the boundary at which ions enter at the Bohm velocity.

Figure 33 shows the LIF signal from an excitation wavelength of 611.6547 nm in the vertical direction, corresponding to $v_{ion} = 3.08 \times 10^3$ m/s. The time steps are 100 ns apart and cover one complete bias cycle (t = 0 is at the most cathodic phase).

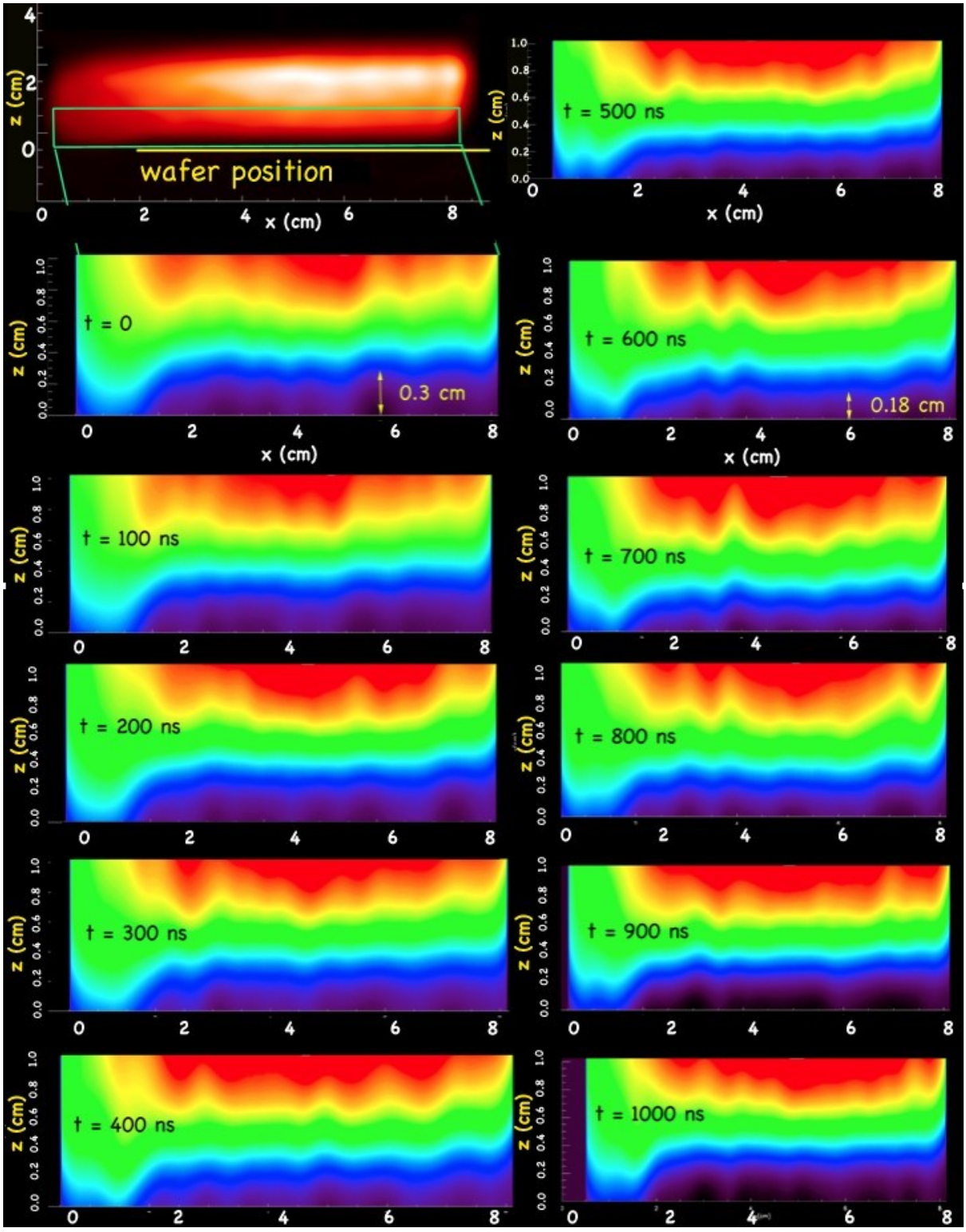

Figure 33: LIF signal at 611.6547 nm ($v_{ion} \approx c_B$) at 11 time steps, each 100 ns apart, covering one wafer bias cycle. t = 0 corresponds to the most cathodic phase of the applied bias. The top left panel shows the original photo, with a green box indicating the zoomed in field-of-view of the other panels. Arrows in panels t=0 and t=600 ns highlight the sheath thickness variation.

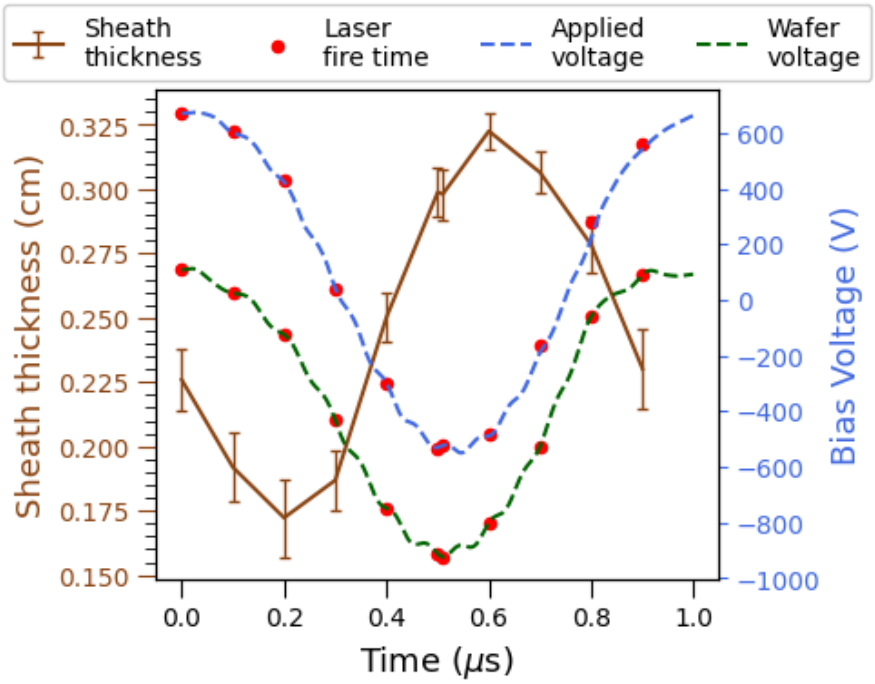

Figure 34: Sheath thickness as function of time (brown solid line) in one RF bias cycle from Figure 33. The applied bias voltage measured outside the chamber (blue dashed line) and the voltage on the wafer (green dashed line) are also plotted, with axis of values on the right. The red dots mark the instantaneous voltages when the laser fired.

The sheath is represented as the dark area where the LIF signal significantly drops and falls below noise level. The sheath edge at the most cathodic phase of the applied bias (t = 0) agrees well with the sheath seen in Figure 31. The bottom of the sheath shows some spatial oscillations. If these oscillations were not from systematic errors, they might be candidates of some instability effects. Recently, electrostatic flow-driven instability has been predicted and observed in presheath, which can cause ion-acoustic fluctuations [102]. However we failed to find a stable structure and wavelength associated with the oscillation we saw. Since the LIF data acquisition is phase-locked to the bias voltage and averaged over multiple pulses of plasma, information needed for investigating the sheath surface fluctuation may be distorted or lost during the averaging. Also, the LIF signal was extremely weak close to the sheath and further investigation on this with the current setup proved to be difficult.

The motion of the sheath along the RF cycle is clearly visible and its height varies from $\delta z = 0.32$ to 0.17 cm. The thickness of the sheath as a function of time in one RF

cycle is shown in Figure 34. The motion is observed to respond to the instantaneous potential change, yet not completely in phase with the wafer voltage.

Near a high bias voltage ($eV_{sh} \gg kT_e$), the sheath capacitance is [90]

$$C_{sh} = K{V_{sh}}^{-3/4} \tag{25}$$

where the constant term K is related to the electrode surface area A, electron temperature T_e and bulk plasma density n_0:

$$K \approx 0.327A\sqrt{en_0\epsilon_0}\,(kT_e/e)^{1/4}$$

In the low frequency regime and high bias potential, the sheath is resistive and the electron current is negligible ($I_i \gg I_d$) [90]. Using the equivalent circuit in Figure 26, the instantaneous sheath resistance R_{sh} can be estimated by V_{sh}/I_i. The time constant of the sheath circuit at the most cathodic part of the waveform is approximately $\tau_{sh} = R_{sh}C_{sh} = 0.023\mu$s in our experiment. This is far from sufficient to explain the delay we observed between the applied voltage and sheath expansion response. To account for the ion inertia effects, a more accurate description on the blocking capacitor C_b and its tuning network is possibly needed, yet unfortunately not accessible to us.

3.5.3 Bulk Drift and Ion Angles

The net drift speed is inferred by locating the peak of the velocity distribution function relative to λ_0 (E = 0 eV). The technique to determine the bulk drift is illustrated in Figure 35 where the vertical LIF signal shows a shift of the main peak to the blue, corresponding to ions drifting towards the wafer. The smaller peak to the red side is due to light reflected from the wafer and is symmetric with the main peak. In cases where ions drift upwards the largest peak is to the red side of λ_0.

The ion motion in case (1) and (3), near the edge of the wafer (x = 0 cm) and near the center (x = 15 cm) are shown in Figure 36 and Figure 37 respectively. The data in both plots indicates only the drift motion and does not include the high energy ions

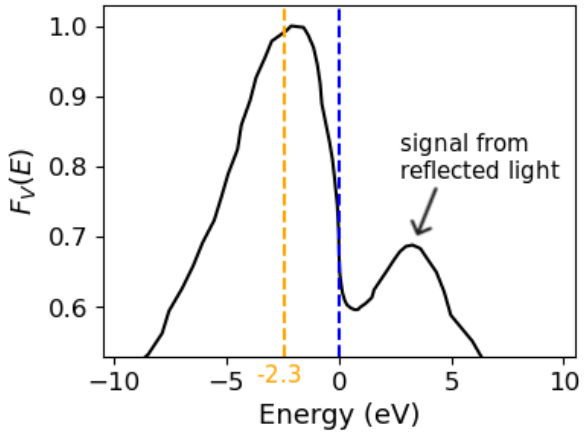

Figure 35: $f_V(E)$ at z = 11.3 mm, zoomed in on the peak that has a blue shift of 2.3 eV. The wafer is biased at -1200 V.

accelerated in the sheath. In case (3), the laser was triggered at one phase point in the coil current. In case (1), the laser was fired at the most cathodic part of the applied bias waveform, which is also phase locked to the coil current. For visual clarity, 1% of the arrows at randomly selected positions are drawn.

In region beyond the edge of the wafer (x < 0) over the electrostatic chuck, LIF measurements indicate net drift of Ar ions vertically upwards.

The background ion drifts have the largest vertical components when close to the surface of the wafer. They are far higher, of course, when the wafer is biased and the sheath is expanded. (e.g. Figure 30). With and without bias there is an abrupt change in the drift pattern near the wafer edge. When the wafer is unbiased the edge drifts are smaller. In this case the maximum drift of 6 eV is about three times the sound speed (based on T_e = 4 eV). In the biased case, very little upward drift is observable past the wafer edge. The ion drifts in the afterglow with and without bias is shown in Figure 38. Here the highest energy ions are included.

The plasma etching of HAR features requires that the angles of ions incident on the wafer are near normal (θ = 0 degree). The ion angle is experimentally obtained by

$$\theta = \tan^{-1}\left(\frac{\mathrm{v}_x}{\mathrm{v}_z}\right) = \tan^{-1}\left(\frac{\mathrm{E}_x}{\mathrm{E}_z}\right)^{1/2} \tag{26}$$

The total velocity close to the wafer is determined by the horizontal drift velocity v_x

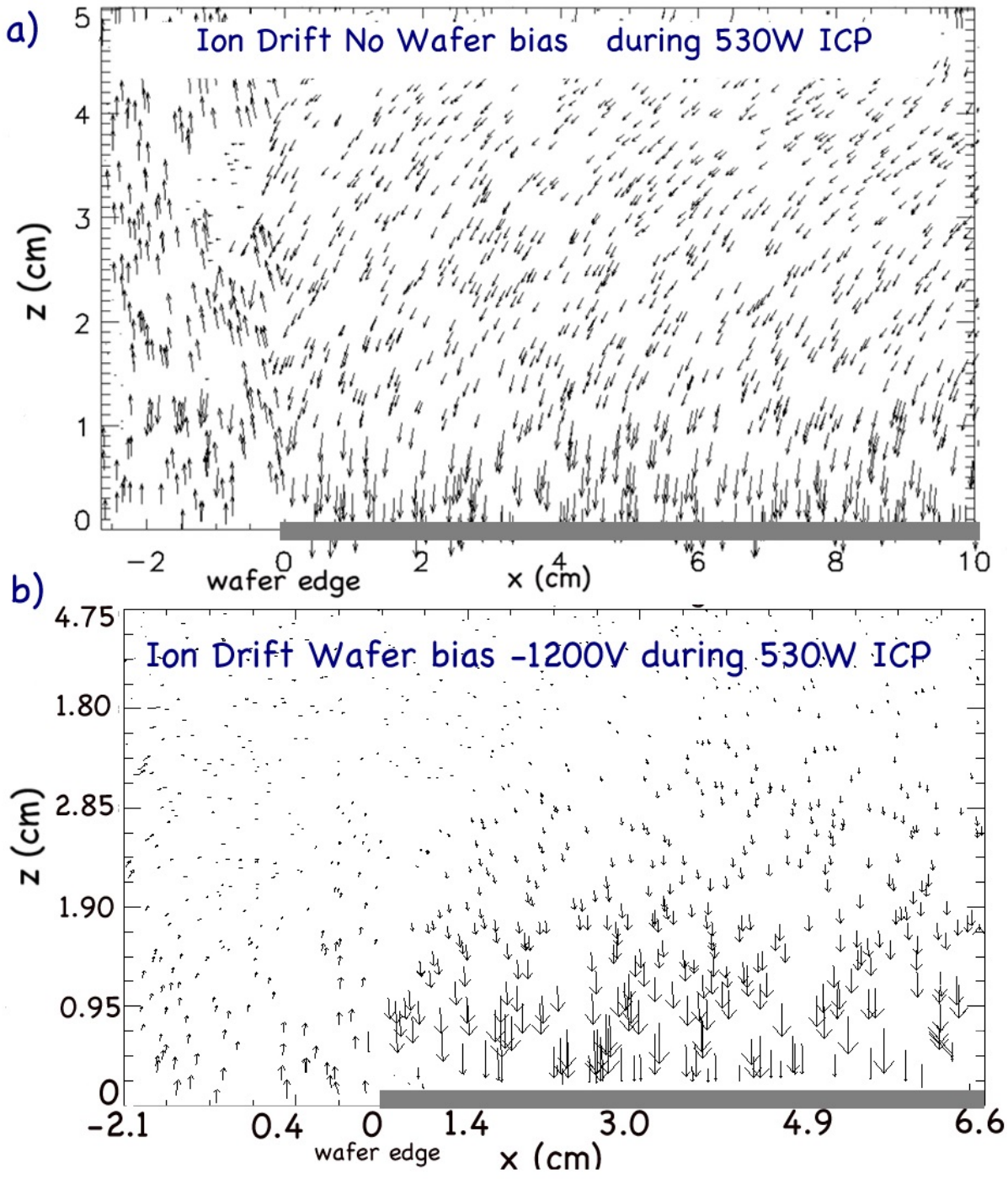

Figure 36: Ar ion drifts near and at the edge of the wafer (x = 0 cm) when it is unbiased (a) and (b) with a -1200V bias. The ICP antenna is at high state. The drifts are in energy (eV). The largest arrows correspond to 6 eV in both cases. The position of the wafer is indicated by the grey rectangles at the bottom.

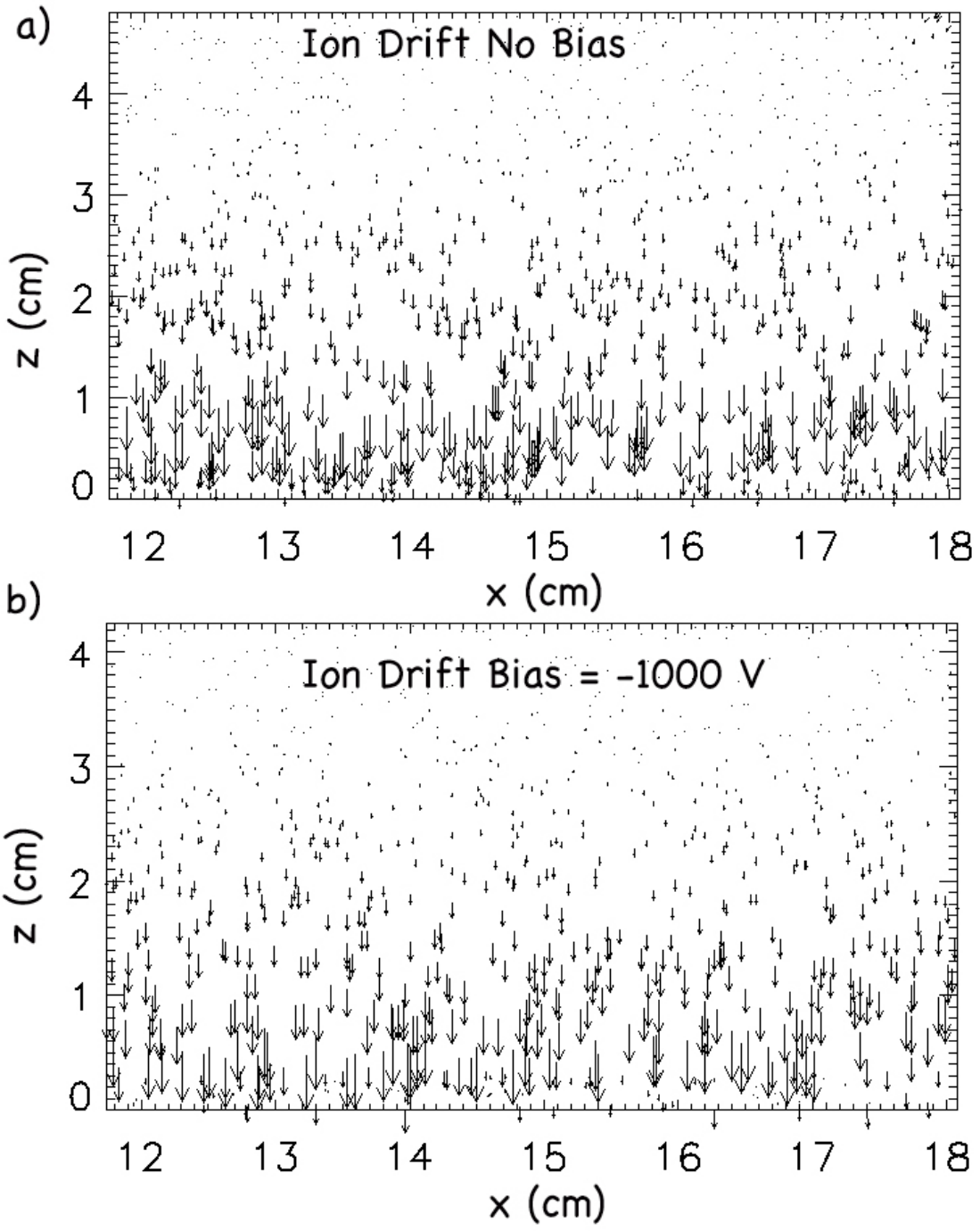

Figure 37: Ar ion drifts near and at the center of the wafer (x = 15 cm) when it is (a) unbiased and (b) with a -1000V bias. The ICP power is on high state. The drifts are in eV. The largest arrows correspond to 5 eV in both cases. Note the kilovolt ions in the sheath above the wafer are not included.

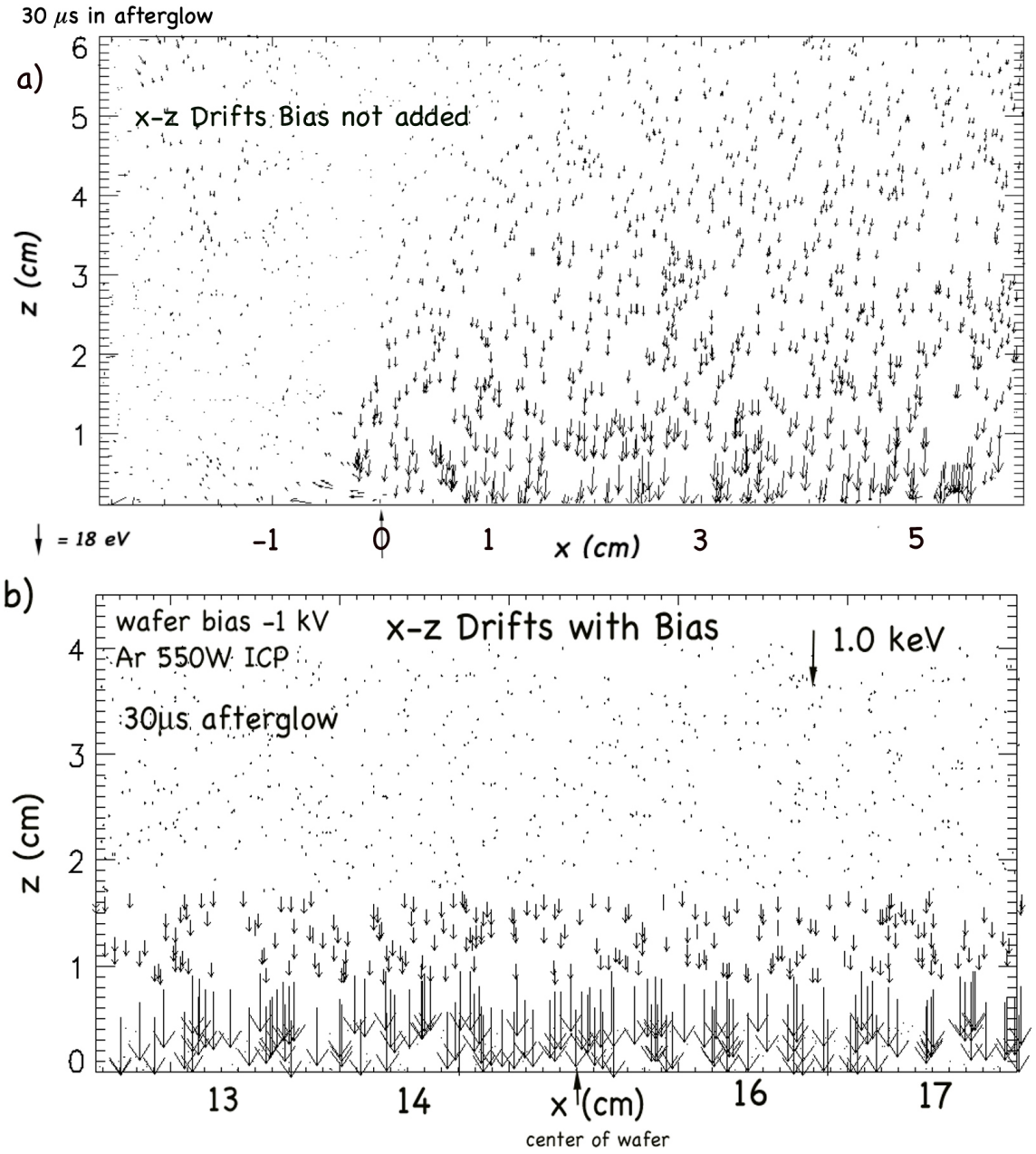

Figure 38: a) Ar ion drifts in the afterglow, (a) near the edge of the wafer (x = 0 cm) when it is unbiased, (b) at the center of the wafer (x = 15 cm) and with a -1200 V bias. The drifts are in eV. A small arrow on the side of each figure shows the magnitude of the largest drift. In (b) the ion drift near the wafer due to the wafer bias is included.

and the downward velocity -v_z imposed by the RF bias. For a -1200 V bias, $v_z = 5.4 \times 10^4$ m/s or 17.5 times the sound speed for 4 eV electrons.

A contour map of the ion angles in velocity space is shown in Figure 39. Away from the edge (x > 1 cm), ion angles just above the wafer in case (1) (Figure 39b) are at most $\theta \simeq 0.5$ degrees, which corresponds to a horizontal energy of order of 0.1 eV and vertical energy of 1 keV. For case (3) the incident angle is $\theta \simeq 0.2$ degrees across the surface (Figure 39a). In the bulk plasma, the ion angle is mostly zero for case (3) and about 0.25 for case (1).

To extend our measurement to an industry related (higher pressure) regime, computational investigations were conducted through a collaboration with Dr. Piskin, using the Hybrid Plasma Equipment Model (HPEM). [103]. The modules that were used are Electromagnetics Module (EMM), Electron Energy Transport Module (EETM), Fluid Kinetics Module (FKM), and Plasma Chemistry Monte Carlo Module (PCMCM). In the simulation, the wafer was divided into four equal pieces and IEADs were collected on the third innermost piece, 3-7 cm from the wafer edge. In addition to 0.5 mTorr, IEADs and sheath thickness are also investigated for 1 and 5 mTorr plasmas that are inaccessible to LIF measurement. The decrease in the pressure causes a reduction in the electron density, causing a larger skin depth and resulting in less inductive power coupling.

The cycle-averaged IEADs (note that experimental LIF data is not cycle-averaged) onto the wafer at z = 0 cm are plotted for three pressures over one bias cycle, in Figure 40a. The IEDs plotted in Figure 40b is angle-integrated from IEADs. Due to larger capacitive coupling at 0.5 mTorr, ions have higher energies with broader angle distributions. This indicates that at more industrial relevant operating pressures, IEADs are expected to be more bimodal and have even smaller incident angles than the LIF measurements made in 0.5 mTorr plasma.

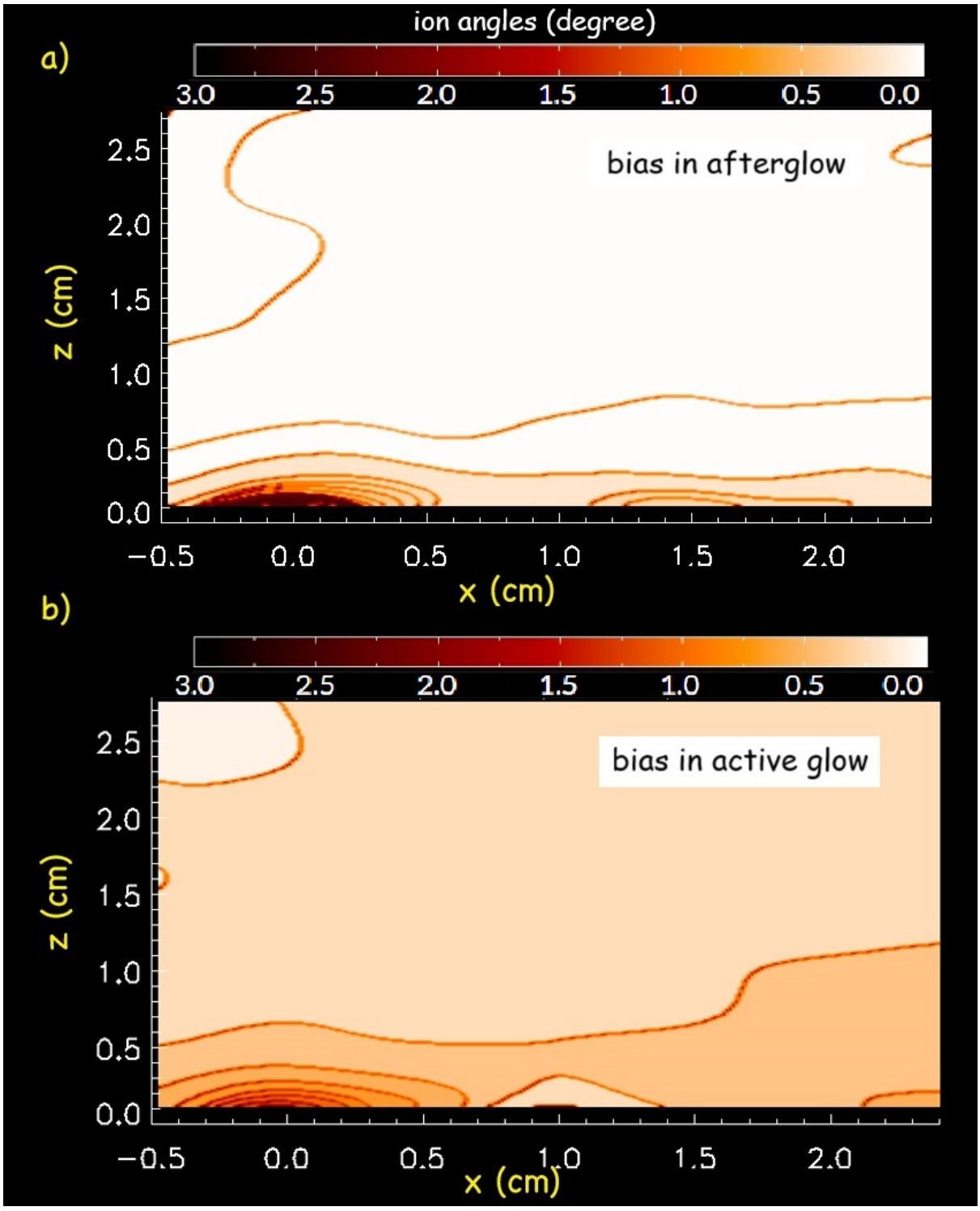

Figure 39: Contour map of downward (to the wafer) angles for ions as a function of x, the distance parallel to the wafer surface, a) for case (3) in the afterglow and b) for case (1). The wafer edge is at z = 0, x = 0. The angle displayed is respect to the normal to the wafer surface.

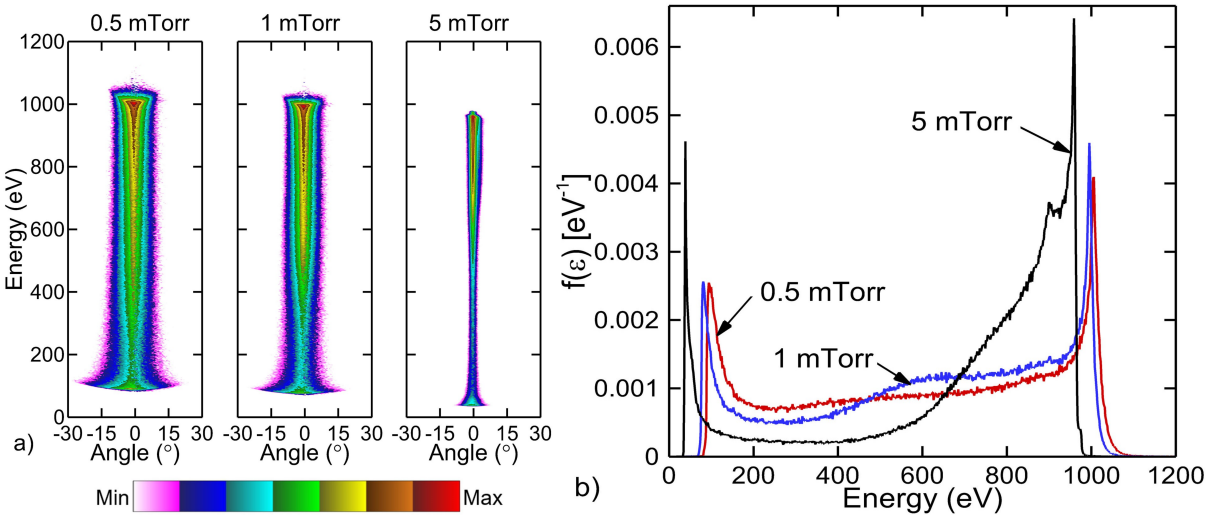

Figure 40: The cycle averaged (over 1 MHz) ion energy and angle distributions onto the wafer surface (z = 0 cm). (a) IEADs for pressures: 0.5, 1, and 5 mTorr. The plots are log-scaled over 3 decades. (b) IEDs, angle integrated from (a). From Qian et al [104].

4 Electrons and Negative Ions

4.1 Electrons and Negative Ions

At low pressure, electron distribution of argon plasma in a planar coil cylindrical reactor typically peaks at the axial center, as long as the chamber aspect ratio (R/L, where R is the radius and L the height) is not to small. The resulting plasma is a high density azimuthally symmetric ellipsoid at the chamber center, surrounded by lower density boundary. When electronegative gas such as oxygen is added to the argon discharge, negative ions are added to the charge balance equation. The relatively immobile negative ions are trapped in the bulk plasma by the ambipolar electric field. This may cause electron density profile to shift off-axis, and even pushed to the boundary. In this case, a toroidal shape electron distribution under the planar coil is often observed.

Electronegative plasmas are often characterized by the electronegativity α, defined in some literature as the ratio of negative ion density to positive ion density ($\alpha_{-/+} = n_-/n_+$), or in other literature as the ratio of negative ion density to electron density ($\alpha_{-/e} = n_-/n_e$). Since quasi-neutrality is often assumed except in the sheath, α is a measure on how many negative species in the bulk plasma are negative ions and how many are electrons.

In Ar/O_2 plasma, the main charged species are Ar^+, O_2^+, O^+, O^-, O_2^-, O_3^- and electrons. Quasi-neutrality holds between these species. In the pressure range of our interest (1 - 100 mTorr), computational studies show that O^- is the dominant negative specie in Ar/O_2 and pure O_2 plasma, followed by a small amount of O_2^- and negligible amount of O_3^- [105, 106]. The dominating presence of O^- and its loss mechanism in low pressure ICP has been experimentally confirmed in many previous work [30, 107, 108].

O^- is mainly created by dissociative attachment of the ground state O_2 and metastable state $O_2(a^1\Delta_g)$ oxygen molecule:

$$e + O_2 \rightarrow O(^3P) + O^-$$

$$e + O_2(a^1\Delta_g) \rightarrow O + O$$

and mainly lost through ion-ion neutralization with O^+ and detachment on the ground state atomic oxygen $O(^3P)$:

$$O^- + O^+ \rightarrow O(^3P) + O(^3P)$$
$$O(^3P) + O^- \rightarrow O_2 + e$$

A complete set of chemical reactions in Ar/O_2 is provided by Gudmundsson and Thorsteinsson [108].

A special region of interest for pulsed ICP is the transient transition phase between the two coupling modes. The coil power is coupled to the plasma either capacitively (E-mode) or inductively (H-mode). When operating in E-mode, plasma is sustained by the electrostatic field generated by the voltage drop from the powered coil. Electrons are heated by the expansion and collapse of the RF sheath. The E-mode usually happens in low plasma density or low RF input power. Plasma in H-mode is sustained by the electromagnetic field induced by the RF coil current. Electrons are heated by the oscillating field at the boundary, and transfer the energy across the chamber through collisions.

In pulsed operation, plasma usually undergoes a transition from low density E-mode to high density H-mode at the onset of each pulse. This transition can be visually identified, since photo emission from E-mode is usually much fainter due to the lower ionization rate, and the plasma concentrate near the coil. H-mode has stronger photo emission with plasma filling the entire chamber. The mode transition may cause hysteresis of the internal plasma parameters and overshoot on the external applied power due to the fast changing matching condition. Therefore, the ICP breakdown can be very unstable, and the temporal electron density profile may have a local overshoot [32, 34, 54].

4.2 Measurement Techniques on Electronegativity

One of the simplest and most commonly applied method to estimate electronegativity is by comparing saturation currents in electropositive plasma and electronegative plasma. The saturation current method is first proposed by Shindo *et al.* for measurement in Ar/SF_2 [109]. In an argon plasma, the ion saturation current I_+ and electron saturation

current I_{es} (ignoring the negative ion current) are

$$\begin{aligned} I_+(Ar) &\propto n_+(Ar)S\sqrt{\frac{T_e(Ar)}{M_+(Ar}} \\ I_{es}(Ar) &\propto n_e(Ar)S\sqrt{\frac{T_e(Ar)}{m_e(Ar}} \end{aligned} \tag{27}$$

where n_+ is the positive ion density, n_e is the electron density, S is the probe surface area and M_+ is the positive ion reduced mass.

Similarly, in an electronegative plasma with a discharge gas denoted by X,

$$\begin{aligned} I_+(X) &\propto n_+(X)S\Omega(X)\sqrt{\frac{T_e(X)}{M_+(X}} \\ I_{es}(X) &\propto n_e(X)S\sqrt{\frac{T_e(X)}{m_e(X}} \end{aligned} \tag{28}$$

where Ω is the correction factor to account for the change in effective sheath surface area and ion velocity at the sheath edge due to electronegativity. Combining the above equations and the quasi-neutrality condition, it can be obtained that

$$\alpha_{-/+} = \frac{n_-(X)}{n_+(X)} = 1 - \frac{I_+(Ar)}{I_+(X)}\frac{I_{es}(X)}{I_{es}(Ar)}\sqrt{\frac{M_+(Ar)}{M_+(X)}}\Omega(X) \tag{29}$$

Therefore electronegativity can be deduced by first measuring saturation currents in pure Argon, and then in varying ratios of argon to electronegative gas. Equation 29 is valid for a wide range of $\alpha_{-/+}$ less than 0.99. Above 0.99, contribution from negative ion to the saturation currents may become significant. For $\alpha < 0.6$, it was experimentally shown that Equation 29 provides measurements even without the correction term Ω.

The delicacy of using Langmuir probes in electronegative plasmas, especially oxygen plasma, was extensively discussed by Amemiya [29, 72, 110], prior to the emergence of the saturation current method. The Druyvesteyn method modified for negative ion diagnostics was used in Amemiya's experiments. This method requires the second derivative of the I-V curve (I'') to show two distinguishing energy peaks for electrons and negative ions, which turned out to be difficult in our system. For a cylindrical probe, the correc-

tion factor Ω was proposed to be $\Omega = \sqrt{2(t_+ + \eta_B)}\,[(1-\alpha)\exp -\eta_B + \alpha \exp(-\eta_B/t_-)]$, where t_+ and t_- are the positive and negative ion temperature normalized to T_e, η_B is the Bohm voltage normalized to kT_e.

Another commonly used method for obtaining electronegativity is photodetachment. The electrons can be temporarily stripped from the negative ion by laser with energy larger than the electron affinity. The increase in electrons after the laser pulse is a direct measurement of the negative ion population. The temporal electron profile can be detected by common diagnostics for electron density such as cavity ring-down spectroscopy, Langmuir probes and hairpin probes. Cavity ring-down spectroscopy is non-intrusive and more often used in high energy or compact system [111–113], while probe assisted photodetachment is popular for low temperature plasma in accessible chambers [76, 77, 114, 115].

Apart from direct measurement on negative ions, electronegativity can also be inferred from measurement of electron density and positive ion density [116]. While there are abundant methods to obtain space- and time-resolved electron density, diagnostics on positive ion density is relatively limited. Retarding field analyzer are often used for obtaining positive ion information including time-resolved energy distribution and density distribution, but the spatial resolution is usually low. The development on the floating harmonic probe technique brought some new possibilities on positive ion density measurement [117].

More recently, Sirse *et al.* proposed on applying negative DC bias pulses to a hairpin probe and examining the change in sheath properties around the probe [118]. The negative ion density and temperature can be deduced from the electron density overshoot at the end of the negative pulse. Pandey *et al.* extended this method to infer a variety of plasma parameters including electron temperature and plasma potential in a Ar/O_2 plasma [78].

4.3 Experimental Setup

The chamber pressure was kept at 10 mTorr, with a total gas flow of 20 sccm. The gas flow from the argon tank is controlled by a MKS Instruments 200 sccm mass flow controller. The gas flow from the oxygen tank is controlled by a Unit Instruments 20 sccm mass flow controller. The root mean square average input power was set at 500 W.

Electron density was measured by a hairpin probe moving in a 10 cm x 20 cm half cross-sectional plane. The length of the hairpin is approximately 2 cm, and the measured electron density was taken as the volume-averaged value centered at the middle of the hairpin tip. Electron temperature and plasma potential were measured by an RF compensated Langmuir probe moving in the same data plane. The specifics of the hairpin probe and RF compensated Langmuir probe are given in Chapter 2.

Negative ion density was measured by the saturation current method as well as probe assisted photodetachment. The RF compensated Langmuir probe covered the same data plane as the electron density measurement. To obtain the electron and ion saturation current, the probe was swept with a 200 μs voltage ramp. The negative ion density map was obtained from calculation using n_e and α at each location. M_+ in Equation 29 was estimated from calculation [119]. In the pressure range of our interest, O_2^+/O^+ ratio has an almost linear increase with the oxygen content.

A frequency-doubled 532 nm Nd:YAG laser (Spectra Physics Pro-230) was used for photodetachment event. The energy of the photon should be chosen so that it is above the detachment energy of the negative ions, but below ionization energy of the neutral species and the work function of the probe tip material (copper). These values are listed in table [76]:

The laser was directed from the laser room to the adjacent processing chamber room through a drilled hole on the wall and combinations of mirrors, as shown in Figure 41. The laser beam enters the reactor chamber through a Pyrex window and exit through the opposite port into a beam dump. The beam path is in radial direction at z = 5 cm. The chamber wall was anodized and was therefore black to make sure there are no electrons created on chamber wall by the stray laser light. The beam size at the entry of the Pyrex

Photon energy	2.33 eV
O^- detachment	1.46 eV
O_2^- detachment	0.44 eV
O_2 ionization	12.07 eV
O ionization	13.6 eV
Cu work function	4.7 eV

Table 2: Energy levels for the photodetachment experiment in oxygen plasma.

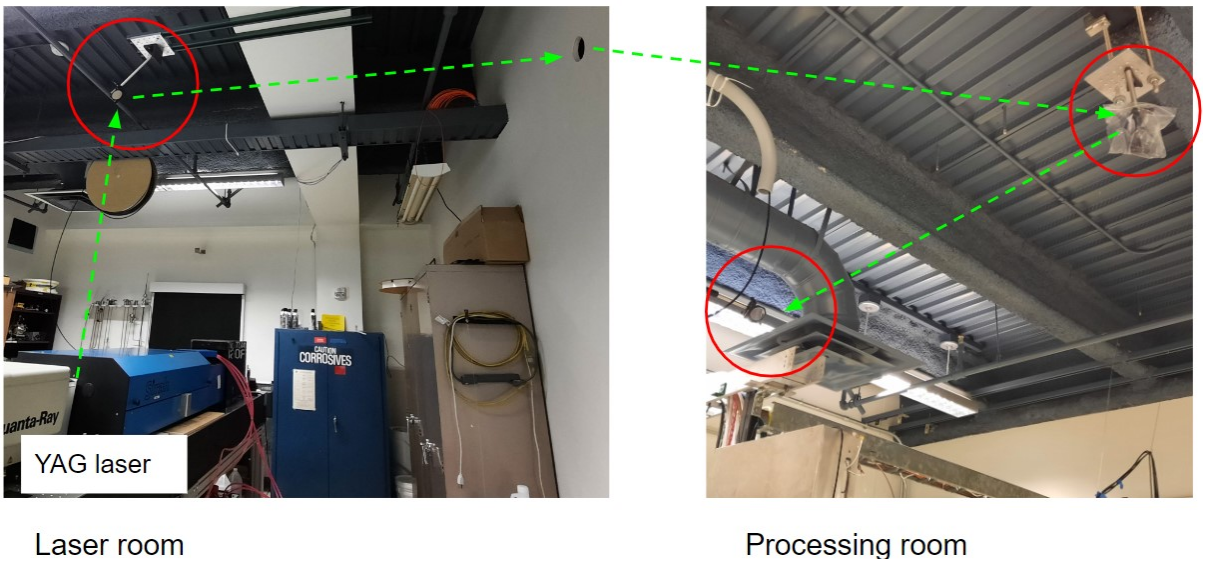

Figure 41: Photo of the equipment setup for photodetachment experiment. The beam path, shown as the dotted green arrows, goes across two room through a hole drilled on the wall. The reflective mirrors are circled in red.

window is 5 mm x 7 mm, which defines the resolution of our measurement. The geometry and the beam path inside the chamber is demonstrated in Figure 42.

The hairpin probe was placed directly in the beam path. The laser power was tuned so that the detachment detected by the probe was saturated. The growth in fraction of photodetachment usually shows an inverse exponential curve as a function of laser energy flux. The laser can operate solely on the oscillator or be amplified by the amplifier. At maximum oscillator and no amplifier, the laser output (29 mJ/cm^2) is on the low end of the saturation curve. When the amplifier was turned to just 10% of its maximum, the laser flux was 135 mJ/cm^2 upon entering chamber and the detachment was close to saturation.

While the photodetachment technique provides more accurate measurement on neg-

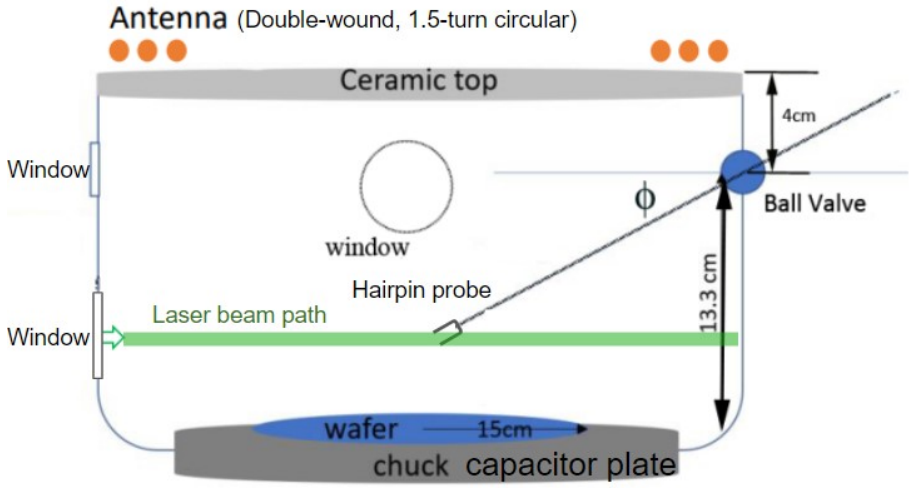

Figure 42: Schematics of the ICP chamber and photodetachment experiment (not to scale). The laser beam enters from the left window and exit the right window to a beam dump.

ative ion density, it is very limited due to the optical accessibility in our case. The measurement was confined to the beam path at z = 5 cm along the radial direction. This is close to the edge of the plasma. However, most of the negative ions are expected to be trapped in the plasma bulk, and can be more easily accessed by the Langmuir probe. The major uncertainty of the Langmuir probe technique comes from the positive ion reduced mass M_+ term in Equation 29. Without actual measurement on the positive specie composition, the assumed ratio of O_2^+/O^+ may be very inaccurate and greatly distort the result. We therefore calibrated the Langmuir probe result with the photodetachment result. Negative ion density was first estimated by electronegativity measured by Langmuir probe and electron density measured by hairpin probe (assume quasi-neutrality), and then calibrated by photodetachment result at z = 5 cm.

4.4 Results

Hairpin probe measurement on the electron density profile on the half rz plane is plotted in Figure 43 for three compositions of discharge gas. As previously defined, r = 0 is the axial center and z = 0 is the position of the wafer. The coil is approximately at r = 16.5 - 18.5 cm. Each column is related to a gas composition and each row is taken at the same

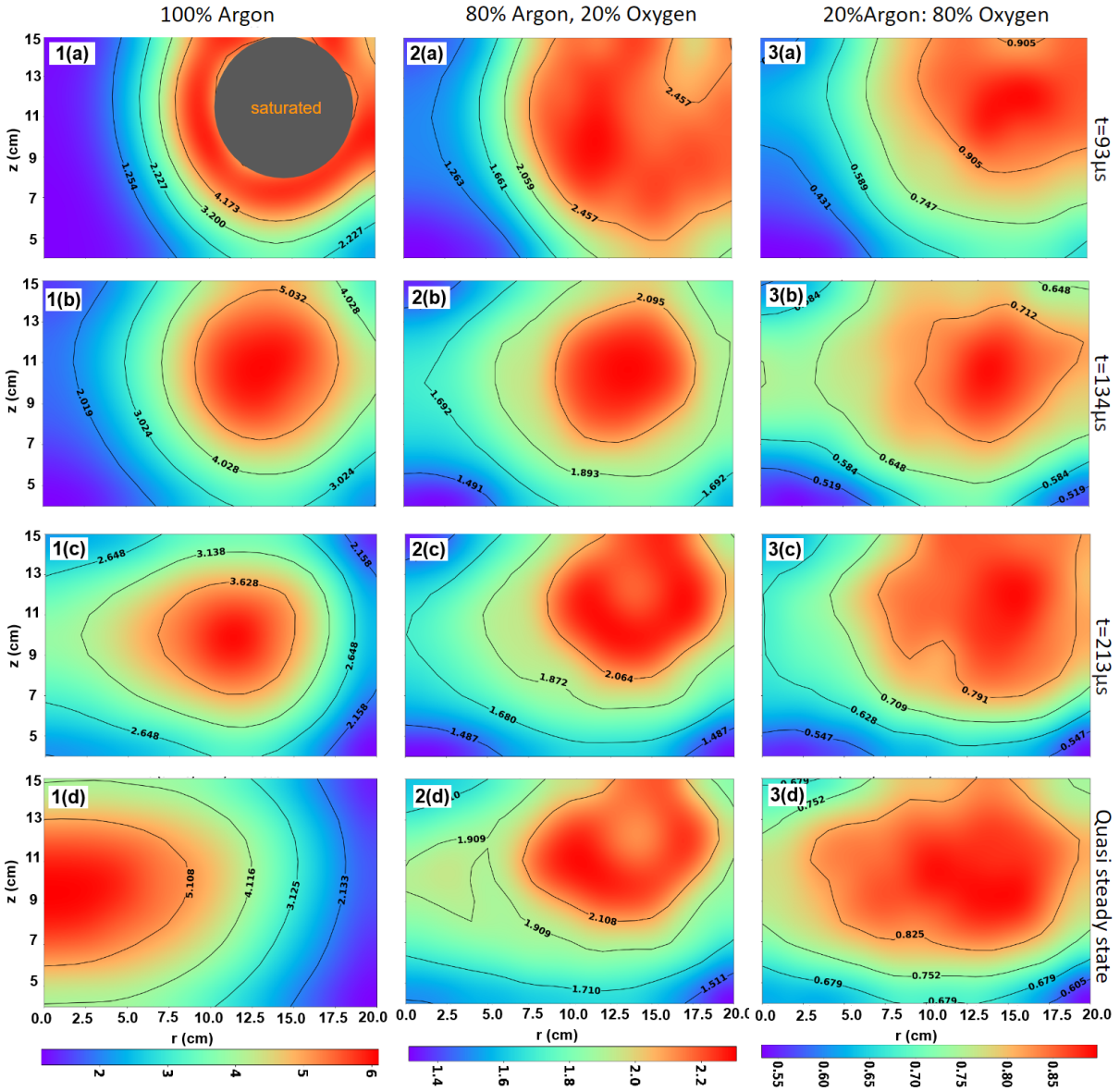

Figure 43: Temporal evolution of electron density ($\times 10^{10}$cm^{-3}) obtained by a hairpin probe at the onset of the pulse. 1(a-d): Ar; 2(a-d): 20% O_2 + 80% Ar; 3(a-d): 80% O_2 + 20% Ar. Row a-c are synchronized, and the timings are marked on the right. Row d is in quasi-steady state, which takes longer to reach in Ar. The timings for column 1, 2, 3 are t=1213 μs, 914 μs, 914 μs, respectively. Measurement is partly saturated in 1(a).

time regime. We specifically look at the early time development, from the initial plasma turn-on to the quasi-steady state.

Right after the RF current turns on, the plasma density peaks under the coil where the induced field is the strongest. External measurement on the applied power shows an overshoot up to 1300 W from the usual 500 W operation, and gets stabilized after 250 μs. The electron density due to this large overshoot exceeds the measurement range of the hairpin probe in Figure 431(a). Ion saturation current was collected by the RF compensated Langmuir probe at the same chamber location and time stamp. n_e inferred from I_{sat} is calibrated against the hairpin probe measurement at other spatial location, and shows a peak density of $7.5 \times 10^{10}\text{cm}^{-3}$ inside the Figure 431(a) saturation region. The density overshoot is 25% of the peak quasi-steady state density. The overshoot is suppressed in Ar/O_2 plasma, which shows a significantly smoother transition due to the reduced electron density and greater energy loss from the chemical reactions of oxygen.

During the temporal interval corresponding to Figure 43, plasmas evolve into the quasi-steady equilibrium state. After that the distribution of n_e do not show significant temporal modulation.

In pure argon plasma, electron density peak slowly drifts to the bulk plasma region at the center. In quasi-steady state, the electron density profile peaks on the axial axis r = 0 and z = 9.5 cm, which is closer to the top (total height is 17.2 cm). When oxygen is added into the chamber, electron density is significantly reduced over the entire plane due to higher collisional loss and dissociative attachment reactions. Rauf and Kushner showed that addition of just 2% oxygen can significantly quench the metastable argon and reduce the electron density [120]. In our obaservation, the peak density decreases from $6 \times 10^{10}\text{cm}^{-3}$ in Ar plasma to $2.3 \times 10^{10}\text{cm}^{-3}$ in 8:2 Ar/O_2 plasma. The density decrease from 8:2 Ar/O_2 to 2:8 Ar/O_2 plasma (peak $n_e = 0.9 \times 10^{10}\text{cm}^{-3}$) is less drastic. Han *et al.* explained this as a decrease of dissociation rate of oxygen molecules, which causes a more gentle decrease in electron density at high O_2 content [121].

The density map also shows that free electrons are depleted by the negative ions at the plasma center. The majority of the electrons remain under the coil, forming a toroidal

electron 'ring' on the top part of the chamber. The density profile in quasi-steady state are sampled at two axial lines and two radial lines. $n_e(z)$ at r = 0, 18 cm and $n_e(z)$ at z = 9, 14 cm are plotted in Figure 44. r = 0 cm is the axial center, where argon plasma electron density peaks. r = 18 cm is the radial line right under the coil. z = 9 cm is where argon plasma axially peaks, slightly above the center plane of the cylindrical chamber. z = 14 cm is close to the top ceramic lid. For visualization of the qualitative comparison, the density is normalized to the maximum on the line. In argon plasma, electron distribution has sharp density gradient pointing from center of the chamber to the boundary area. Even a small amount of oxygen input (4 sccm, 20% O_2) significantly change the plasma density profile. In Ar/O_2 plasma, electron density is more uniformly distributed in the entire chamber. The toroidal density peak is most obvious in the bottom left panel, where $n_e(r)$ increases from center to the coil. While the increase in oxygen content from 20% O_2 to 80% O_2 reduces the total electron density, it doesn't significantly change the relative profile.

Electronegativity $\alpha_{-/e} = n_-/n_e$ in 20% O_2 and 80% O_2 quasi-steady state plasma is plotted in Figure 45. We assumed quasi-neutrality $n_+ \approx n_- + n_e$ and estimated the negative ion density by $\alpha_{-/e} n_e$ The calculated negative ion density is plotted an Figure 46. In both cases, the plasma is more electronegative in the bulk region. Maximum $\alpha_{-/e}$ increases from 1.8 in 20% oxygen to 2.56 in 80% oxygen. In lower oxygen concentration, the negative ion density peaks around r = 10 cm. The negative ion distribution becomes more uniform as oxygen content increases, although the peak is still off-axis.

Yoon *et al.* computationally found that in 10 mTorr planar coil oxygen ICP, electron density profile maintains its maximum on axis, while negative ion density peaks closer to the coil [122]. This distribution is opposite to what we found. The RF frequency and geometry of the chamber may be the major cause of this difference, as their simulation was done for a tall chamber (R/L = 15 cm / 50 cm) with one turn coil. Heating and specie distribution in ICP are very sensitive to the geometry. Simulation with the effort to imitate our experimental condition shows that with the addition of 20% O_2, the electron density profile still peaks at the bulk plasma [54]. The difference may be due to the

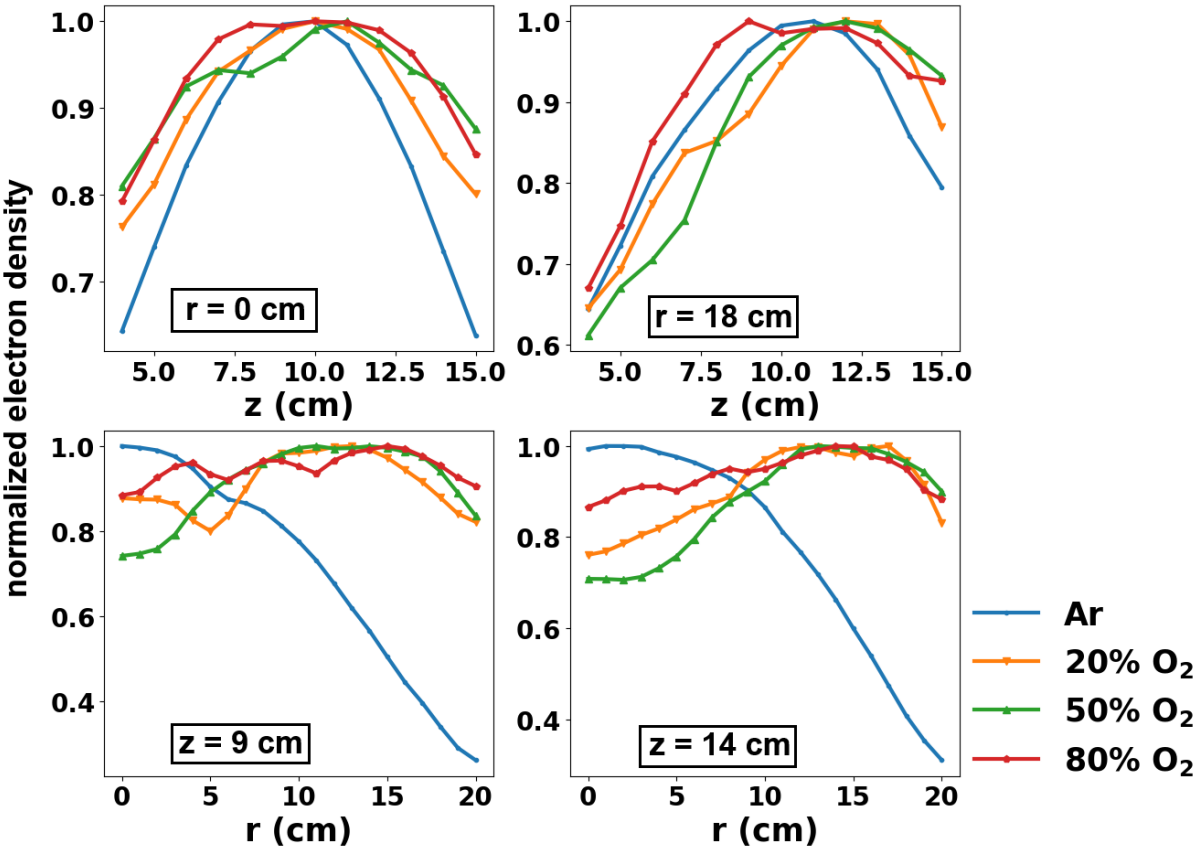

Figure 44: n_e as a function of z (top row) or r (bottom row), normalized to the maximum value on the trace. In clockwise direction: $n_e(z)$ at r = 0 cm (axial center), $n_e(z)$ at r = 18 cm (under the coil), $n_e(r)$ at z = 9 cm, $n_e(r)$ at z = 14 cm.

different power matching condition, since our reactor do not have an external matching network. To ensure that the result obtained was not due to insufficient inductive power, a test run on electron density was done in 700 W and 1 kW oxygen plasma. The density showed the similar profile to Figure 43.

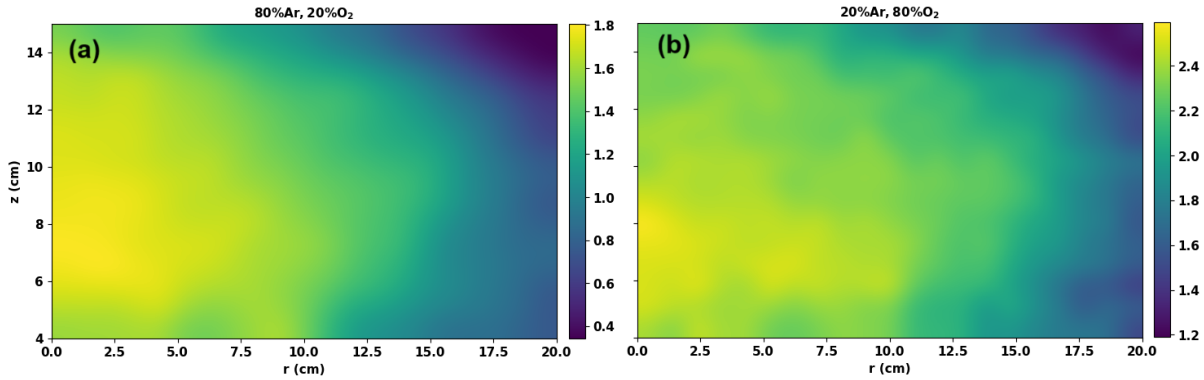

Figure 45: Electronegativity $\alpha_{-/e} = n_-/n_e$ in two ratios of gas. (a) Ar:O_2 = 8:2 (b) Ar:O_2 = 2:8.

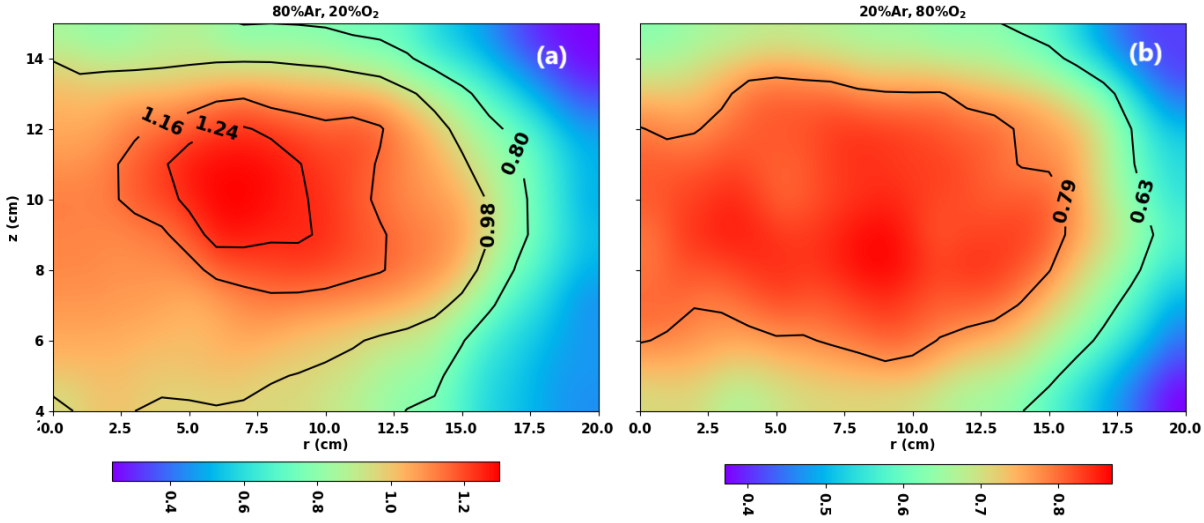

Figure 46: Negative ion density ($\times 10^9 \mathrm{cm}^{-3}$) calculated from measured n_e and $\alpha_{-/e}$, assuming quasi-neutrality. (a) Ar:O_2 = 8:2 (b) Ar:O_2 = 2:8.

5 Fields and Energy in Electronegative Plasma

5.1 EM Field and Heating Mechanism in ICP

Plasmas inside an ICP chamber are mainly sustained by the induced electromagnetic field. It is therefore of great research interest to investigate the fields and plasma profile with certain source geometries and operating conditions. Plasmas created in a cylindrical chamber powered by a planar coil on the top usually have azimuthal symmetry. The induced magnetic field, secondary induced electric field, and induced current are often assumed to have components:

$$\begin{aligned} \vec{B} &= B_r\hat{r} + B_z\hat{z} \\ \vec{E} &= E_\theta\hat{\theta} \\ \vec{J} &= J_\theta\hat{\theta} \end{aligned} \tag{30}$$

El-Fayoumi and Jones did a thorough review of the mathematical description of the EM fields inside a planar coil ICP chamber with no plasma, uniform plasma and non-uniform azimuthally symmetric plasma [123]. In a chamber without discharge gas, the magnetic field induced by the planar coil has a standing wave pattern similar to that produced by a solenoid. After plasma breakdown, the power is dissipated through various heating mechanism in the plasma. This can be experimentally shown as field line patterns evolving and propagating inside the plasma along the phase of the driving RF current.

The difficulty of theoretically describing the temporal-spatial distribution of field and power in low pressure, weakly ionized plasma at low driving frequency comes from the fact that collisionless energy transfer may be involved, and particle kinetics can be non-local [124]. Electrons and ions can react instantaneously to the field changes (as shown in Chapter 3), and may travel a macroscopic distance across the chamber during a single RF period. The fluid approach is often insufficient to describe low density ICP. The interactions of fields and currents can be computationally complicated, and at the same time highly sensitive to operating parameters and chamber geometry. Direct measurements

on fields and currents are therefore important for the characterization and prediction of the plasma dynamics.

In this experiment we mainly focused on H-mode (energy is transferred to the plasma through RF induced electromagnetic fields), since this is the major heating mechanism of pulsed ICP in the parameter space that we worked on. Experiments were triggered 9 ms after the pulse onset, when E-H transition had been long completed and quasi-equilibrium was certainly established.

The power deposition in a cylindrical ICP driven by a planar coil can be modeled as radial / axial decay of a transverse electric mode wave [125]. There is no major propagation in the electric field ($\hat{\theta}$) direction. Most power absorption happens within a characteristic decay length δ, generally comparable to the classical skin depth. The exact value of δ, however, is very sensitive to the multi-dimensional geometry, and depends on the heating mechanism at work. There are two major electron heating mechanism in H-mode plasma: collisional heating through Joule heating (ohmic heating), and collisionless heating through interactions with the electromagnetic field. Contribution from ion current is often ignored due to their low mobility.

When the plasma is collisional enough that the thermal electron motion is unimportant ($\nu_{en} \gg \omega_{rf}$, ν_{en} is the electron-neutral collision frequency, ω_{rf} is the driving RF frequency), Joule heating is the dominating mechanism. The relation between the current and the electric field is local and can be described by Ohm's law: $\vec{J} = \sigma_p \vec{E}$, where $\sigma_p = e^2 n_e / m_e(\nu_{en}^2 + i\omega_{rf})$ is the plasma conductivity (n_e is the plasma density). The phase lag between the current and the field is less than 90° so that the transferred power $\vec{J} \cdot \vec{E}$ remains positive [126]. With the assumption of Equation 30, the power deposited through collisional heating is [125]

$$P_c = \int_V \frac{1}{2} \mathrm{Re}\left(\vec{J} \cdot \vec{E}\right) = \frac{e^2 E_\theta^2 \delta}{4 m_e} \frac{\nu_{en}}{\nu_{en}^2 + \omega_{rf}^2} n_e \tag{31}$$

When the plasma is only weakly collisional ($\nu_{en} \ll \omega_{rf}$), the charged particles may traverse the electric field and gain energy along the path before significant amount of collision events. If the electron transit time through the power absorption region is short

compared to the driving RF period, the electrons may get a velocity kick from the field before the field changes to the opposite sign. The net effect will be an positive energy transfer from the field to the electrons [127]. In this regime, the conventional Ohm's law no longer holds true. The current can be solved by rewriting the Ohm's law equation with a non-local conductivity tensor $\vec{\sigma_p}(\vec{x},t)$: $\vec{J}(\vec{x},t) = \iint \vec{\sigma_p}(\vec{x}-\vec{x'},t-t') \cdot \vec{E}(\vec{x'},t')\ \mathrm{d}\vec{x'}\ \mathrm{d}t'$, and treating the electron oscillations due to RF field as perturbations to the electron distribution function [127, 128]. Other analytical approaches include adding a viscosity term in the electron momentum equation to account for the non-local effect [129]. In practice, however, as the chamber geometry and plasma condition becomes increasingly complicated in recent development, these quantities are more often evaluated through computer simulations.

Two unique features of collisionless heating are the non-monotonic spatial distribution of the field due to anomalous skin effect, and the possible existence of negative power absorption region. The anomalous skin effect is generally observed in highly conducting system where the electron mean free path becomes comparable or larger than the classical skin depth. The thermal electron motion is able to transfer current from the classical skin layer deep into the plasma, resulting in a non-monotonic spatial decay of the electromagnetic field [130, 131]. The thermal motion may also cause the current to become more than 90° out of phase with the electric field. This leads to negative $J \cdot E$ regions, where energy returns from the plasma to the field. Godyak made the first observation of negative power absorption in ICP for a driving frequency of 13.56 MHz and 6.78 MHz at 10 mTorr, but did not see the effect at 3.39 MHz [132]. Han *et al.* observed regional negative power absorption experimentally and computationally for a driving frequency of 2 MHz [51] in the same machine that this thesis was based on, although the effect was less pronounced than those at higher frequency [133].

It should be noted that the plasma density profile can be significantly different from the power deposition profile. In a large R/L ICP reactor such as our machine, the plasma density profile is almost independent from the power deposition profile at low pressure. Moreover, planar coil geometry is good at maintaining a peak-on-axis density profile

over a wide range of operating conditions. In low pressure collisional regime, the plasma density profile is governed by diffusion equations. The power deposition can be coupled to the particle balance equation to provide the magnitude of the density profile. At higher pressure where particle transport is hindered, the heating may become more localized, and the power deposition profile has more effect on the density profile [125, 134, 135].

5.2 Power Absorption in Electronegative Plasma

The addition of electronegative gas change the plasma properties and consequently the field distribution. The influence of negative ions can be very prominent in capacitive power coupling, since electrons are heated through sheath dynamics and electric field reversal, both of which heavily depends on plasma electronegativity [34]. In H-mode, power absorption is affected by negative ions due to the change in plasma transport and chemistry. Continuity equation set should be extended to include negative ion species. New terms should be introduced to the energy balance to account for processes such as dissociative attachment and recombination [122]. These all add to the complexity of the system.

As shown in Chapter 4, electronegativity shifts the electron density peak away from the axis, as the negative ions dominate the bulk center. The plasma conductivity is therefore changed. Vass *et al.* found in a 27.12 MHz oxygen CCP simulation that with increasing electronegativity, collisional power absorption becomes more predominant because the lower electron density leads to the higher plasma resistivity in the bulk, and the shift of electron density maxima from the center create non-monotonic spatial gradient that attenuates the pressure gradient [136].

Compared to argon plasma, electrons are more likely to lose their energy in the chemically reactive electronegative plasma. Research focusing on electron energy distribution in oxygen plasma spark further understanding on electron heating with electronegativity. Lee *et al.* compared the EEDF in capacitive and inductive oxygen discharge. They concluded that collisional heating is inefficient to heat up the low energy electrons from the inelastic reactions in oxygen plasma core, and the penetration of inductive fields is

essential in this case [137]. In a following experiment, they suggested that the presence of negative ions in the plasma core reduce the ambipolar electric field strength that confines the electrons. As a result, cold electrons can be efficiently heated with even a small inductive field penetrated to the core [138]. Liu *et al.* also reported on a rapid decrease of low energy electrons with increasing O_2 concentration [139]. Despite lower electron density, many investigations reported that the electron energy distribution becomes more Maxwellian [121, 137].

Experiments using time resolved optical emission spectroscopy have shown that in H-mode ICP, the excitation rates of Ar and O_2 have different phase-dependent patterns. Wegner *et al.* showed that while the argon excitation rate has strong axial symmetry and little modulation over the RF cycle, oxygen excitation rate is more localized to the power source and has well separated pattern by each half RF cycle. Electron heating is more efficient when the maximum RF voltage is supplied, and the excitation rate seems to have deeper axial penetration during one of the half cycle [140]. Tadokoro *et al.* similarly reported a greater degree of temporal modulation on excitation rate, as well as spatial non-uniformity, in O_2 plasma than in Ar plasma [141, 142].

There has been some experimental and a great deal of theoretical work on EEDF and optical emission of the metastable states, which only gives indirect information on field and energy transfer in the plasma. Modelling and measurement of oxygen plasma usually focus on specie distribution and global power absorption. To author's knowledge, multidimensional local measurement on induced field and inductive power deposition, especially in an electronegative plasma, is rare and deserves more study.

This chapter is a continued study from Han's previous measurements in pure argon plasma [60]. Experiments in this section extend the measurement to Ar/O_2 plasma and discussed the effects of electronegativity on field distribution and power deposition.

5.3 Experimental Setup

The chamber pressure was set at 10 mTorr, with a total gas flow of 20 sccm. The gas flow from the argon tank is controlled by a MKS Instruments 200 sccm mass flow controller,

while the gas flow from the oxygen tank is controlled by a Unit Instruments 20 sccm mass flow controller. The input power, monitored at the terminal outside the plasma chamber, was kept fixed at 500 W (root mean square average).

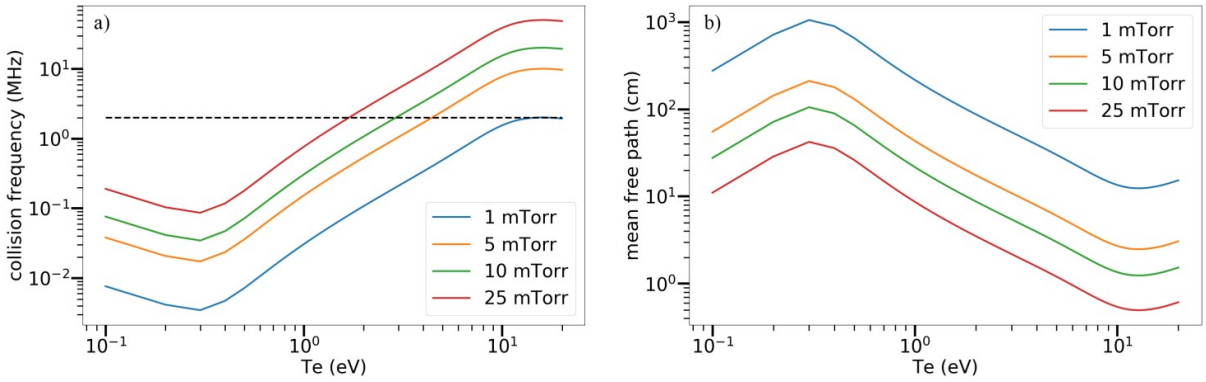

Figure 47: (a) Electron-neutral collisional frequency and (b) mean free path as a function of electron temperature, at four different gas pressure. The driving frequency 2 MHz is highlighted in (a) as the black dashed line. Data is calculated from COP database. The plot is adapted from Han's thesis [60].

Most processing plasma operate in a mixed regime where collisionless and collisional effect may both be present. Calculation of ν_{en} at four different pressures in our chamber is plotted in Figure 47. For 10 mTorr pressure and 4 eV electrons temperature, ν_{en} is only few times larger than $\omega_r f$. We expect the electron heating to be mostly ohmic, but the contribution from collisionless effect can not be ignored.

Bdot probe data was collected in different Ar/O_2 gas mixture: 80% Ar + 20% O_2, 60% Ar + 40% O_2, 20% Ar + 80% O_2 and pure O_2. Azimuthal symmetry of the plasma in this chamber was previously established by Han for various operating RF power and pressure [60]. The probe motion covered a 10 cm x 20 cm half cross-sectional plane, at increment of 0.5 cm. The specifics and calibration of the Bdot (magnetic) probe is given in Chapter 2.

Since the 3-axis Bdot probe rotates inside the chamber, it is necessary to do a transformation on the collected data to reconstruct the magnetic field geometry in Cartesian coordinate. We initially set up the probe so that the shaft is horizontal, the tip is at $r = 0$, and the three orthogonal loops 1, 2, 3 are facing the direction of $\hat{x}$, $\hat{y}$, $\hat{z}$ respectively. The three loops were designed and built in such a way that the cross interference

is minimized. The three pick up signals were amplified through three separate channels of a $\times 100$ differential amplifier, before being digitized by a 8-channel 2 GHz Teledyne LeCroy oscilloscope. The RF coil voltage and current, measured at the terminal of the power source, were simultaneously recorded. Most of the data sets include several RF cycles, typically spanning ~ 5 μs. The time resolution is typically 2 ns. At each probe position, the data collected was averaged over 50 shots on the oscilloscope.

The probe moved in a Cartesian grid inside the chamber, as detailed in Chapter 2. For $\dot{B}_1$, $\dot{B}_2$, $\dot{B}_3$ collected by the three loops at chamber position (x, y, z), we did the following transformation:

$$\phi = \tan^{-1}(y/x), \quad \theta = \tan^{-1}\left(z/\sqrt{x^2+y^2}\right)$$
$$\dot{B}_x = B_1 \cos\theta\cos\phi - B_2 \sin\phi - B_3 \sin\theta\cos\phi$$
$$\dot{B}_y = B_1 \cos\theta\sin\phi + B_2 \cos\phi - B_3 \sin\theta\sin\phi$$
$$\dot{B}_z = B_1 \sin\theta + B_3 \cos\theta$$

Data collection is mostly on the cross sectional plane, so y is fixed at 0 for most of the time. B_2 is usually more than 10 times smaller than B_1 and B_3. We directly translated our measurement on the half plane to cylindrical coordinate, which is more conventionally used for this type of setup: $B_r = B_x$, $B_\theta = B_y$, $B_z = B_z$.

After the transformation on geometry, the coil-induced magnetic field $\vec{\boldsymbol{B}}$ was reconstructed through integration of the raw probe data ($\dot{B}_r$, $\dot{B}_\theta$, $\dot{B}_z$) over time. The integration was performed on the 1D time series data using scipy.integrate.cumtrapz python function, and looped over all probe positions.

The secondary current, induced by $\vec{\boldsymbol{B}}$, can be obtained by taking the curl of $\vec{\boldsymbol{B}}$ in space. Since B_y is small, we mainly investigated the azimuthal component of the current:

$$J_\theta(r,z) = -\frac{1}{\mu_0}\left[\frac{\partial B_r}{\partial z} + \frac{\partial B_z}{\partial r}\right] \tag{32}$$

The curl was computed by numpy.gradient function. The array input was the 2D

magnetic field array sliced at one time stamp. The time evolution was obtained by looping the calculation over all time stamps.

The induced electric field in aximuthal direction was calculated using Faraday's law, assuming cylindrical symmetry:

$$\oint E_\theta(r,z)dl = \iint \frac{\partial B_z}{\partial t} dS \tag{33}$$

Power dissipated in the plasma from inductive coupling was defined and evaluated as the product of the current density and electric field density:

$$P_{ind} = \vec{J} \cdot \vec{E} = J_\theta E_\theta \tag{34}$$

The total input power P_{tot} should equal to P_{ind} plus the power from capacitive coupling P_cap and the power lost P_{loss}. For the coil operating at 500 W, the resistive loss was measured to be 70 W. This value was obtained from driving the coil at 500 W with no plasma in the chamber and directly reading the power meter of the generator.

There may exist second harmonic currents orthogonal to J_θ due to curvature of the magnetic field produced by the planar coil and nonlinear electron inertia [143]. These nonlinear effects were observed to be more significant with decreasing gas pressure and decreasing driving frequency. In any case, they only account for less than 15% of the first order current (J_θ), and even less for the total power dissipation since energy scales as current squared [144]. In this section, we only focused on azimuthal current. Investigation on J_r and J_z has been previously done by Han [60], who confirmed that these quantities were negligible in terms of energy balance.

5.4 Results

5.4.1 Field and Current

The amplitude of the induced magnetic field $|B| = \sqrt{B_r^2 + B_z^2}$ shows monotonic spatial decay. Anomalous skin effect, characteristic of predominant collisionless heating, is not

observed. The power absorption should be mostly due to ohmic heating. Figure 48 plots the decay of the field in radial position (48(a)) and axial position (48(b)). As previously defined, $z = 0$ is the wafer position and $r = 0$ is the center of the chamber. For better comparison, the amplitude is normalized to the maximum amplitude B_0 measured at the point closest to the coil (r = 18 cm, z = 15 cm). (48(a)) is fixed at z = 15 cm, 2 cm below the ceramic top. (48(b)) is fixed at r = 18 cm, a vertical column directly under the coil. Due to the geometry of the planar coil (large radial spread) and the size of the chamber (diameter is larger than height), the decay in 48(b) seems sharper than (48(a)).

The axial decay in all gases have exponential shape. The radial decay is largely exponential, except the flattened part between 16 - 20 cm due to the spread of the coil. In both direction, magnetic field decay the quickest in Ar. With the addition of oxygen, the magnetic field penetrate deeper into the plasma. The penetration depth slightly increases as oxygen content increases, although this increase seems to be almost saturated beyond 80% O_2.

The actual decay is rather a two dimensional process, graphed as a color map in Figure 49 for Ar, 20% O_2 and 80% O_2. The 2/e and 1/e contour lines are also plotted as a reference. While the 2/e contour line doesn't change much, 1/e contour line clearly spreads out to the plasma volume as oxygen content increases. The power absorption mostly happens inside the e-folding depth (distance from the coil to the 1/e magnitude contour line). In pure argon, the e-folding depth of the magnetic field amplitude is ~ 5 to 7 cm in $\hat{r} + \hat{z}$ direction. This is increased to ~ 10 cm in 80% Ar 20% O_2. In 20% Ar 80% O_2, the e-folding contour line is broad enough to extend to the other half of the rz plane. This ensures more uniform heating in radial direction and result in the smoother spatial gradient in electron density, as shown in Chapter 4.

The azimuthal direction induced current J_θ in increasing concentration of oxygen gas is plotted in Figure 50 and 51. The color maps visualize the cross section of the toroidal current rings formed around the magnetic field line. The panels from top to bottom cover one complete RF cycle. The 0π (first row panels) starts at the minimum of the coil current.

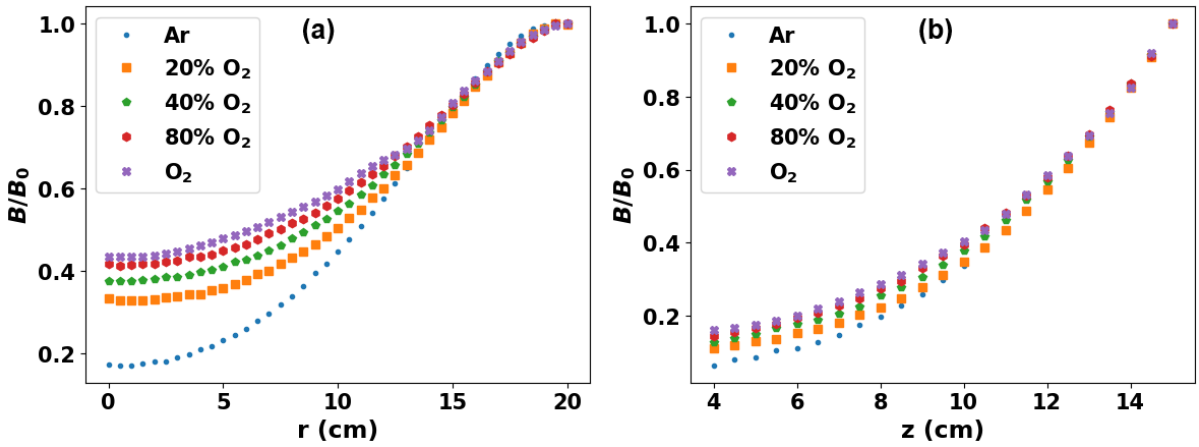

Figure 48: Normalized magnitude of the induced magnetic field (a) as a function of radial position, at z = 15 cm (closest data acquisition point to the coil) (b) as a function of axial position, at r = 18 cm (under the coil).

J_θ reverses its direction every half RF cycle. Apart from the alternating flow direction, the cross-sectional density pattern of J_θ also changes along the RF cycle. In pure argon discharge, the peak of the induced J_θ concentrates under the coil at phase = 0, and penetrates toward the center of the chamber during a quarter cycle. Due to the sharp spatial gradient of the induced magnetic field, the current also has larger amplitude. With the addition of oxygen, electrons are depleted in the electronegative core, increasing the plasma resistivity in the bulk region. As a result, the peak of the induced current stays in the boundary layer. In O_2, the propagation of the current pattern is almost straightly downward.

El-Fayoumi *et al.* directly measured the total induced J_θ in a similar chamber setup, using a Rogowski coil that encircled the entire current on rz plane [145]. The total induced J_θ is reported to lag the planar coil current by 160°, and have an amplitude that was 20% of the coil current amplitude. In another investigation done by the same group in the same plasma chamber, induced J_θ was calculated from Bdot probe measurement using Equation 32, similar to our approach. The total induced J_θ was calculated through integrating the J_θ contours over the cross sectional area, and showed a phase lag of $-151°$ and amplitude of 43% coil current amplitude. The disparity in the measurement suggests that the amplitude and phase of J_θ is very sensitive to the plasma parameter and matching condition of the circuit.

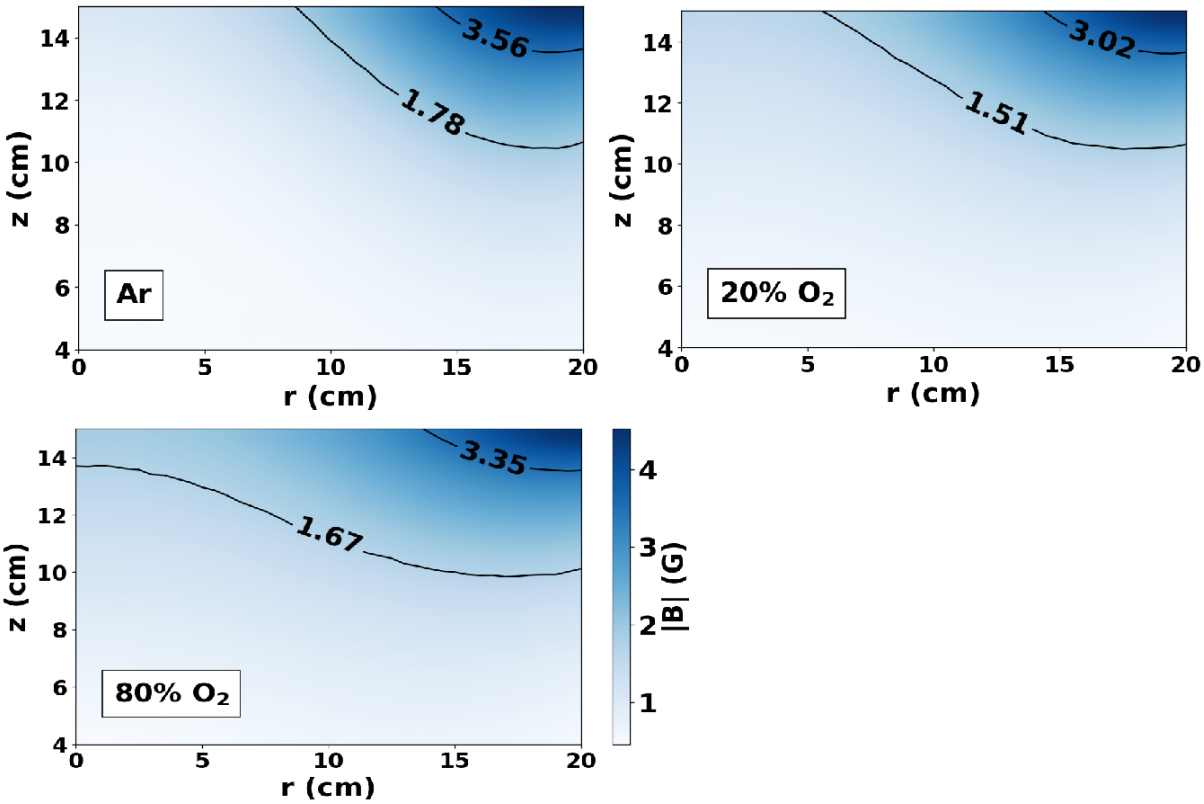

Figure 49: Magnitude of the induced magnetic field in Ar (upper left), 20% O_2 (upper right) and 80% O_2 (lower left). The 2/e and 1/e contour lines are also plotted.

We compared the amplitude and phase of J_θ in different concentrations of oxygen. The time sequence of J_θ during one RF cycles is plotted in Figure 52(a). The data is summed over the entire data acquisition plane, which is approximately the total induced current since below the data acquisition plane (close to the wafer) the current amplitude is minimal. In pure argon plasma, the total induced J_θ shows a phase difference of 180° (0.25 μs) with respect to the coil current. As oxygen content increases, the phase shifts further away. The amplitude of J_θ in pure oxygen plasma is 1/3 of the amplitude in pure argon plasma.

In general, the addition of oxygen, even at lower concentration, significantly change the current distribution and its temporal evolution along the phase of the driving RF. The magnetic field has smoother gradient as oxygen content increases, resulting in a smaller current density across a wider spatial distribution. The pattern of the cross-sectional current density agrees well with the result in Chapter 4, where electron density was shown to be concentrated under the coil and quenched in the bulk center when oxygen

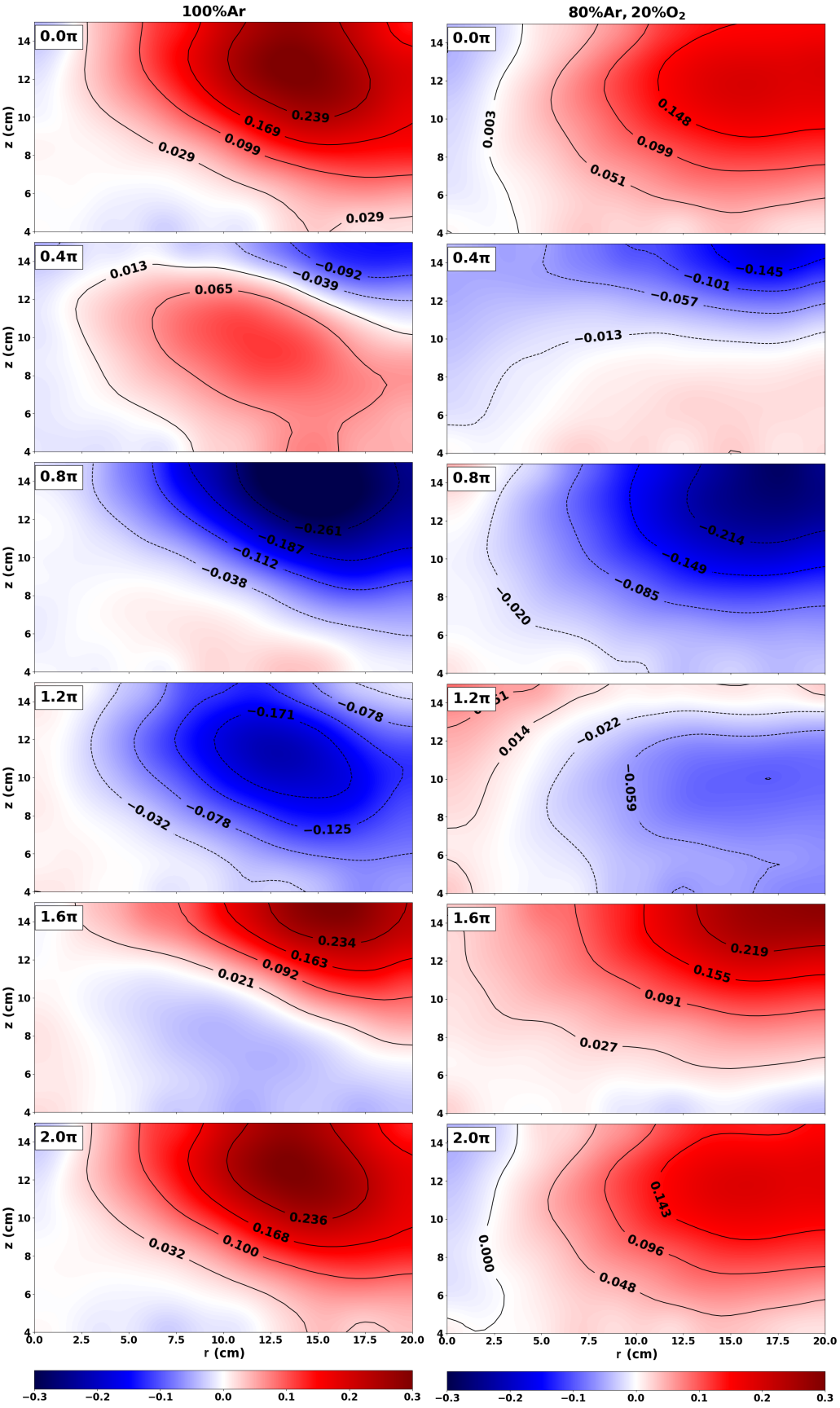

Figure 50: Induced J_θ (A/cm^2) during one RF cycle in quasi-steady state, in pure Ar (left) and 20% O_2 (right). RF phase proceeds from top (+0) to bottom (+2π).

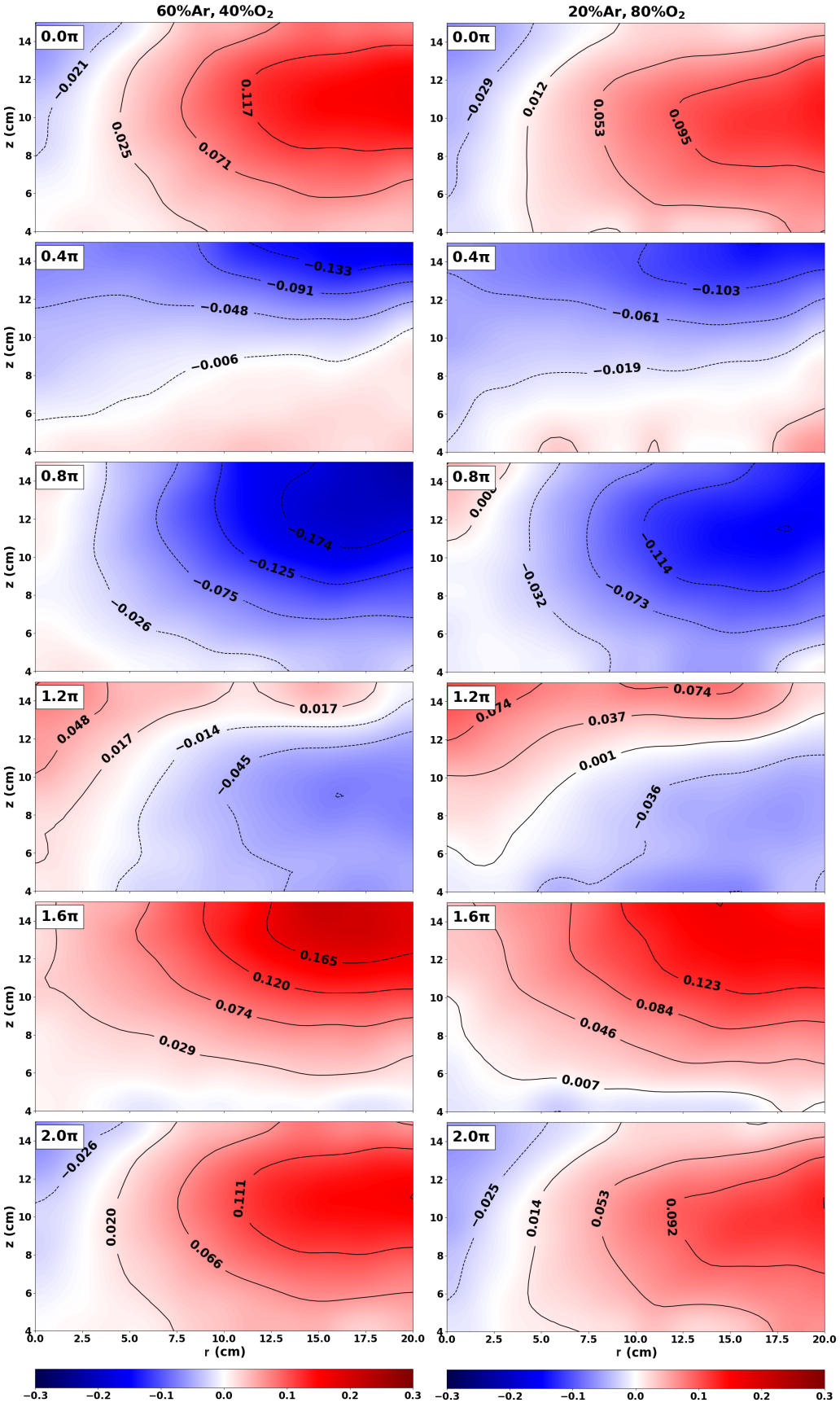

Figure 51: Induced J_θ (A/cm^2) during one RF cycle in quasi-steady state, in 60% O_2 (left) and 80% O_2 (right). RF phase proceeds from top (+0) to bottom (+2π).

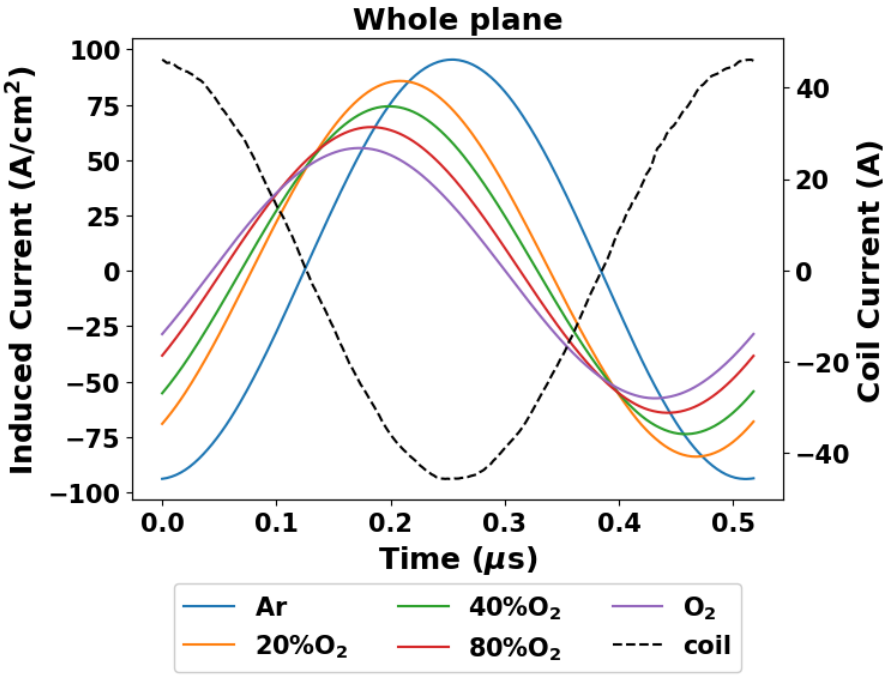

Figure 52: Time sequence of induced J_θ (color coded solid lines, left axis) during one RF cycles, summed over the whole data acquisition plane. The coil current synchronous to the probe measurement is plotted in black dashed line (right axis).

was added. In pure argon, the spatial distribution of J_θ shows a propagation towards the bulk center where the electron density peaks. The density gradient is steep in radial direction since the field penetration is shallower and the chamber is bigger in radial dimension. In oxygen containing discharge, current pattern propagate almost straightly downward from the coil, due to the reduced electron density and therefore increased plasma resistivity at the center.

5.4.2 Inductive Power Deposition

Inductive power density averaged over one RF cycle is plotted in Figure 53, for cases of pure argon and pure oxygen. Power deposition mostly concentrates under the coil, not aligned with the peak-on-axis plasma density profile. The pattern of the cycle averaged inductive power deposition are generally similar in different ratio of Ar/O_2, except that the inductive power penetrates deeper into the oxygen containing plasma, and the gradient of the power density is smoother in oxygen. When summed over the whole data plane, the total inductive power density is lower in oxygen, indicating a higher capacitive

power. Figure 53 is in accordance with Tuszewski's calculation and measurement that induced magnetic field penetrates deeper into the plasma in oxygen gas, although their experiments are conducted in a more collisional regime than ours [146, 147].

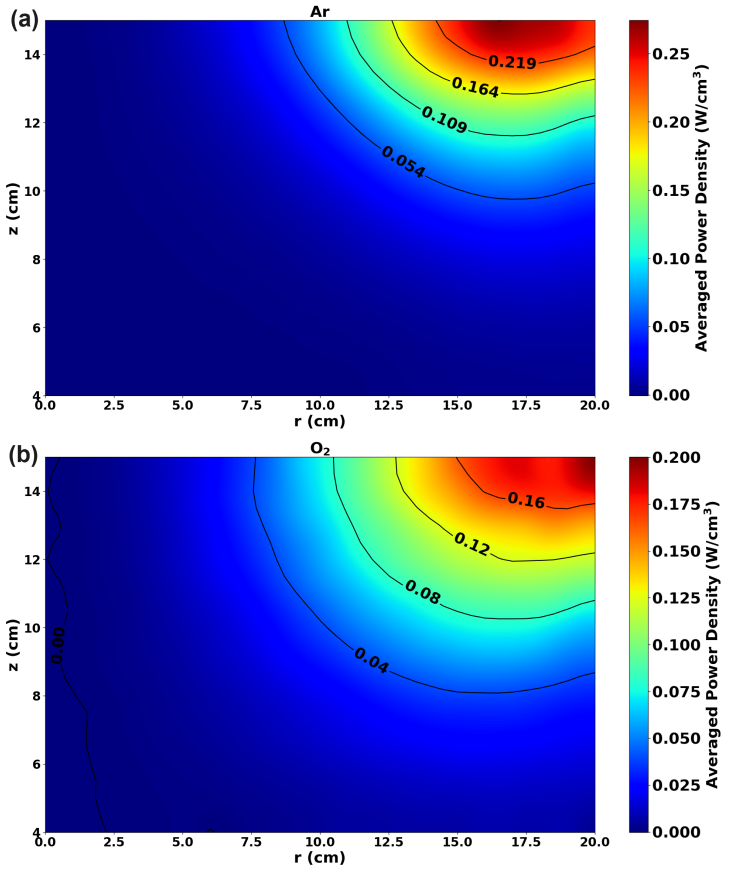

Figure 53: Averaged Power density (W/cm^3) over one RF cycle, (a) in pure argon plasma and (b) in pure oxygen plasma.

Gudmundsson and Lieberman calculated the 1D power absorption depth of oxygen plasma in a similar setting (planar coil ICP, 10 mTorr, R = 15.24 cm, L = 7.62 cm) to be between 2 cm to 2.5 cm for an absorbed power of 300 W to 500 W [148]. The 1/e contour line (0.08 W/cm^3) in Figure 53(b) shows a much deeper penetration. Tuszewski considered the effect of induced magnetic field and included the often neglected magnetic term into the fluid calculation. They found a much smoother radial profile for field magnitude in 5 mTorr oxygen discharge. The e-folding depth of the magnetic field magnitude is around 5 cm in their 5 mTorr, 2 MHz, 150 W argon discharge, comparable to our observation.

Electron temperatures T_e in argon and oxygen plasma measured by an RF compen-

sated Langmuir probe is plotted in Figure 54 for reference. In argon, Electron temperature is comparatively uniform across the plasma volume. T_e has an average value of ~ 3.6 at the bulk center, and slightly increase by roughly 0.4 eV close to the boundary, at r = 12.5 - 17 cm. In oxygen, the heating from the coil becomes obvious and match the power deposition profile.

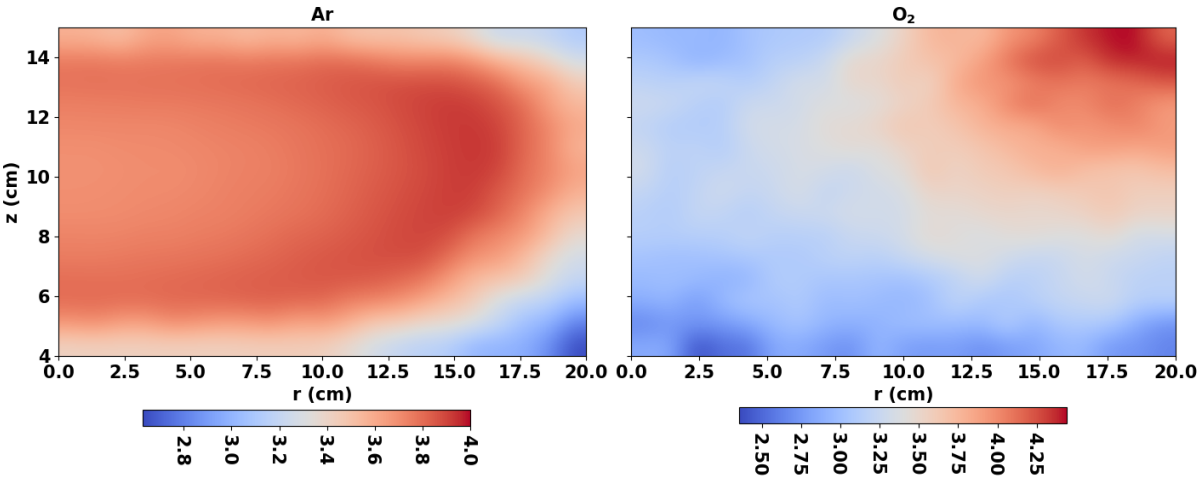

Figure 54: Electron temperature (eV) in Ar plasma (left) and O_2 plasma.

While the averaged power density shows similar patterns with different penetration depth, phase-resolved power density shows very different profiles with the addition of oxygen. Figure 55 compares the instantaneous power density in pure argon and pure oxygen plasma. Ar/O_2 mixtures fall between the two cases. In argon plasma, power density penetrates to the center of the plasma, while with oxygen involved the power density is more concentrated close to the wall. With oxygen gas in the system, the plasma core is electronegative and the electron density peaks at the edge of the plasma instead of at the center, as shown in Chapter 4. Therefore it is expected to see more deposition at the boundary region.

Pattern in Figure 55(b) also suggests that in oxygen containing plasma, there might be more power lost to the chamber wall. However, features shown in the last row of panels are very small compared to the major part of the power deposition (less than 10%), and therefore do not significantly alter the pattern of the averaged power profile in Figure 53.

Negative power absorption was observed in instantaneous power deposition profile, but the magnitude is extremely small in all gases ($< 3\%$ on average). In argon, the observation

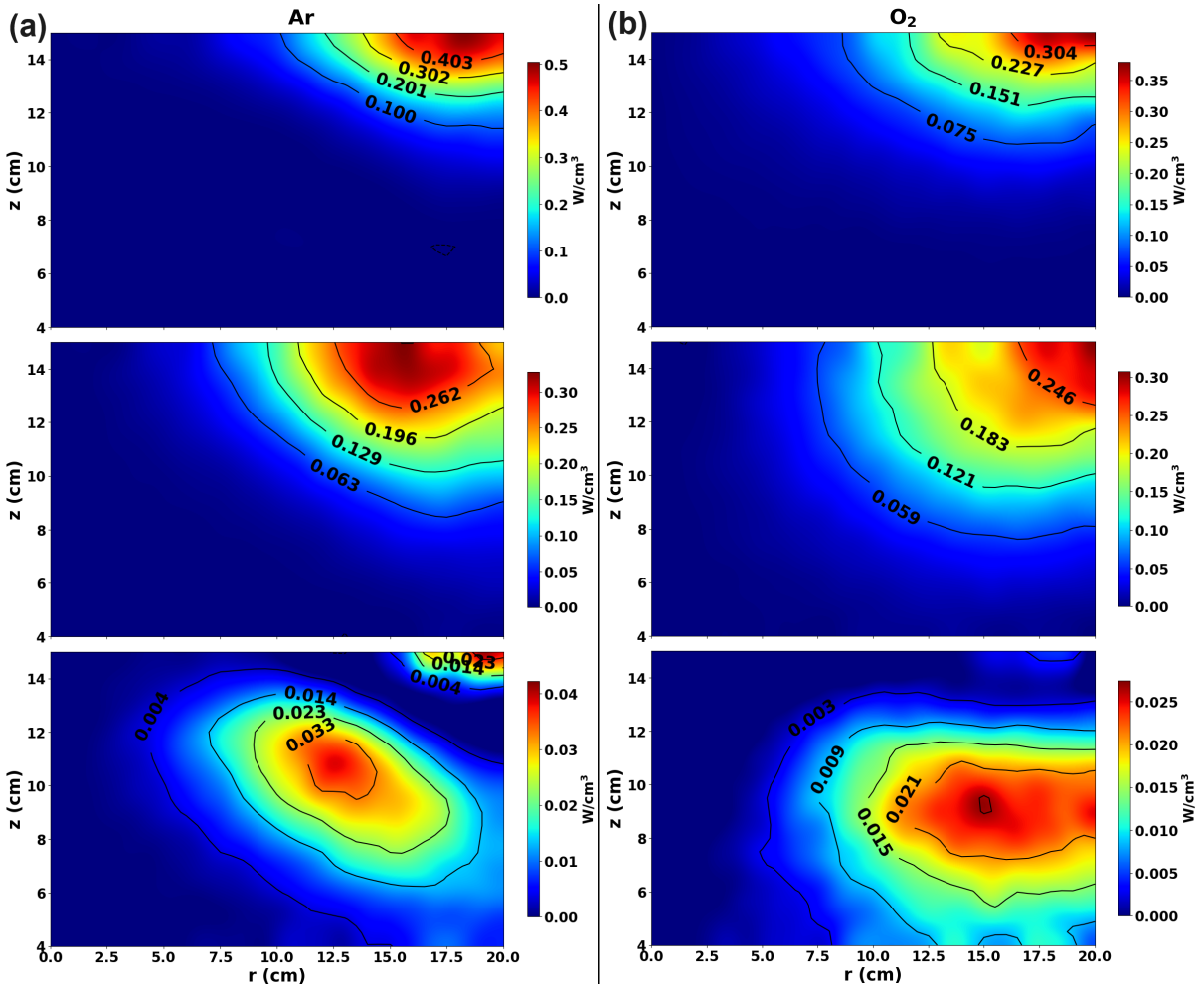

Figure 55: Time progression of instantaneous power density (W/cm^3) during half of an RF cycle, (a) in pure argon plasma and (b) in pure oxygen plasma. Note that the panels are chosen so that they cover the whole process of deposition. Due to the different phase lag in Ar and O_2, the panels in (a) and (b) are not synchronized. The timings of the panels are chosen for the best visual comparison.

agrees with the previous finding [51]. The effect was slightly more pronounced in oxygen containing plasma in the region close to the ceramic top, away from the planar coil (z = 12 - 15cm, r = 2 - 10 cm). Figure 56 shows an example of negative power absorption in O_2 plasma with an exaggerated visual effect. In high oxygen content, the induced field has relatively good penetration to this region, while the electron density is low. As a result, non-local effects are enhanced in this region. On a phase-averaged scale, however, the negative power absorption is negligible.

Power density as a function of time and axial/radial position is plotted in Figure 57 for argon plasma and Figure 58 for oxygen plasma. The surface plots span over one RF

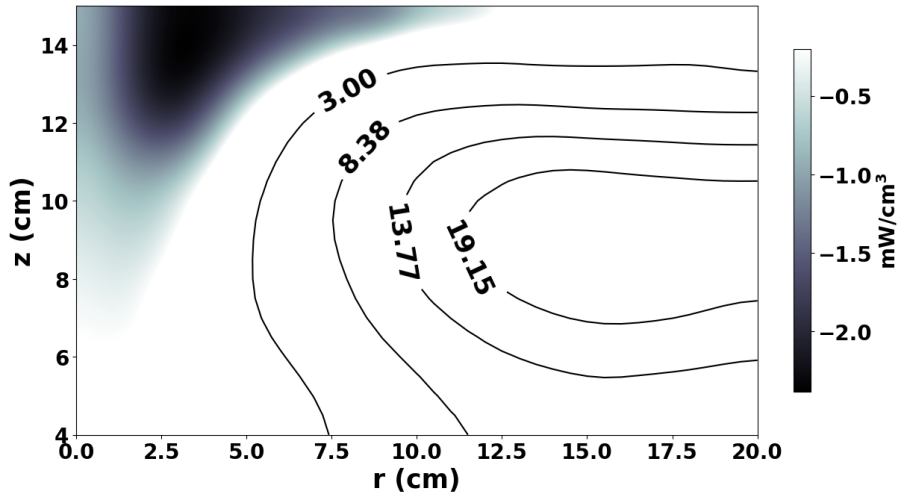

Figure 56: Negative power absorption region in O_2, sampled at the phase where the effect is the most prominent. The positive power contour is also plotted for reference.

driving cycle. Figure 57(a) has the typical shape of a power density profile in ICP with density variation in axial direction, in accordance with previous observations [149].

Generally, the power density profile peaks at the position closest to the coil (z = 16 cm, r = 16.5 - 18.5 cm), and decays into the plasma. The decay is much steeper in argon than in oxygen. In argon, the two power density peaks are largely symmetric, as the electrons are accelerated twice per RF cycle regardless of the direction of the electric field. However, obvious difference is observed between the first peak and the second peak, especially in 58(b). This asymmetry becomes more prominent with increasing O_2 content. For comparison, radial power profile in 20% O_2 and 80% O_2 is graphed in Figure 59. The asymmetry is generally localized close to the coil.

The asymmetry of energy transfer during each half cycle is more of a characteristic of capacitive coupling. In E-mode, electrons gain energy once per RF cycle through sheath expansion and collapsing. During E-H transition, inductive coupling develops and the electrons start to obtain energy from the other half of the RF cycle as well. The gradual development of a second peak in optical emission during the transition from E-mode to H-mode was demonstrated in oxygen plasma by Wegner *et al.* [140] and hydrogen plasma by Abdel-Rahman *et al.* [150] The relation between the asymmetric heating and the asymmetric inductive power density is not completely clear. The instantaneous change in electron temperature / plasma conductivity due to the asymmetric heating may play

a role. Our observation suggests that there is an increase in capacitive coupling under the coil with the increasing O_2 concentration, and that the inductive power deposition profile can be significantly affected and shows phase modulation.

The change in capacitive power in O_2 is also evident in the voltage profile of our RF driving source. While the coil current always had smooth sinuisoidal waveform as plotted in Figure 52 (dotted line), the applied square wave voltage showed significant ripple signal at each falling edge when oxygen was present in the plasma. The impedance matching with electronegative plasma is more complicated and demanding than the argon plasma. The step response became increasingly unstable with increasing oxygen concentration, and possibly further enhance the asymmetry of the two power deposition peaks.

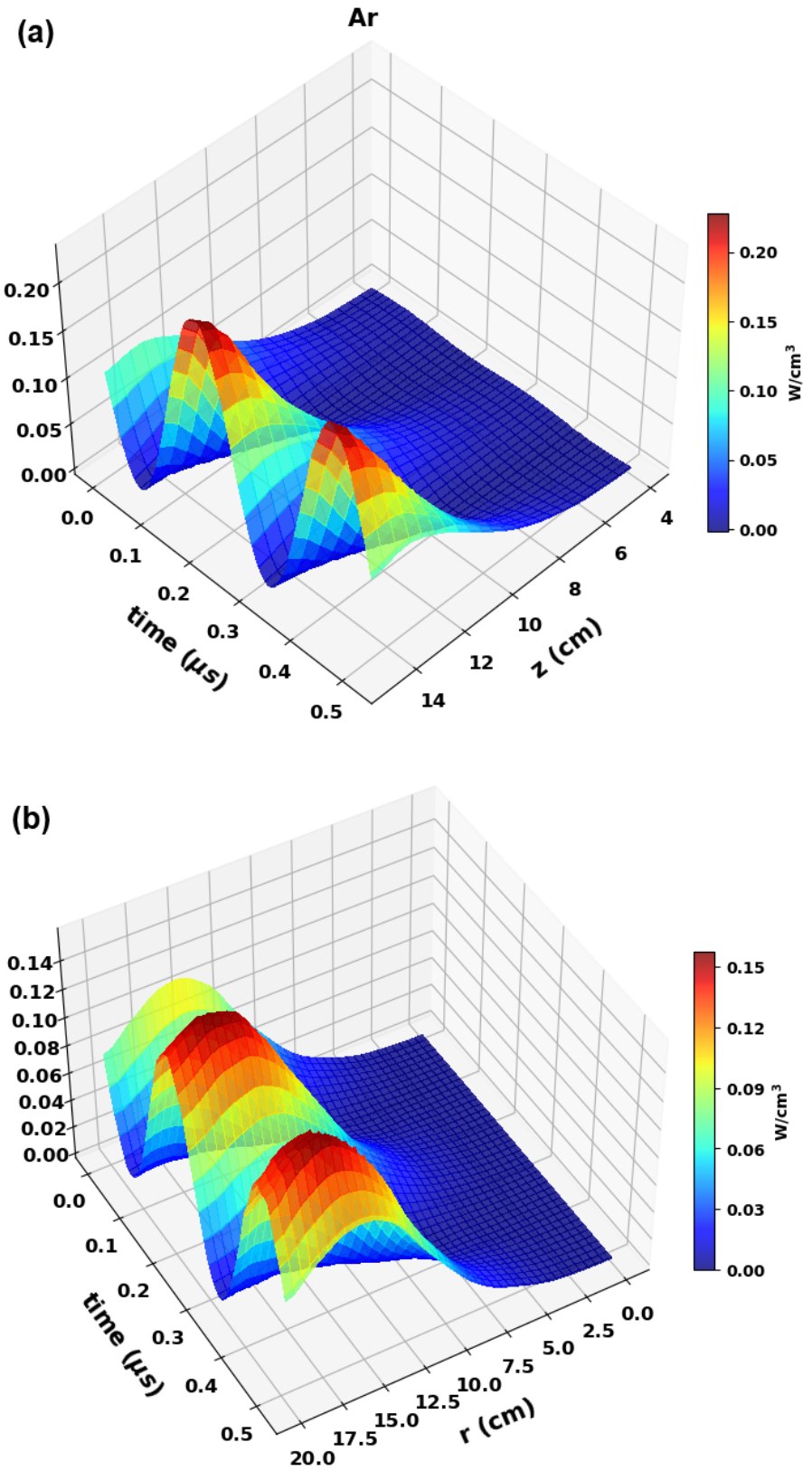

Figure 57: Power density in Ar plasma during one RF cycle (a) at different axial position and (b) at different radial position. In panel (a) the power density is averaged over all radial position for each axial position. Vice versa in panel (b). In both panels, t=0 corresponds to the maximum of coil current.

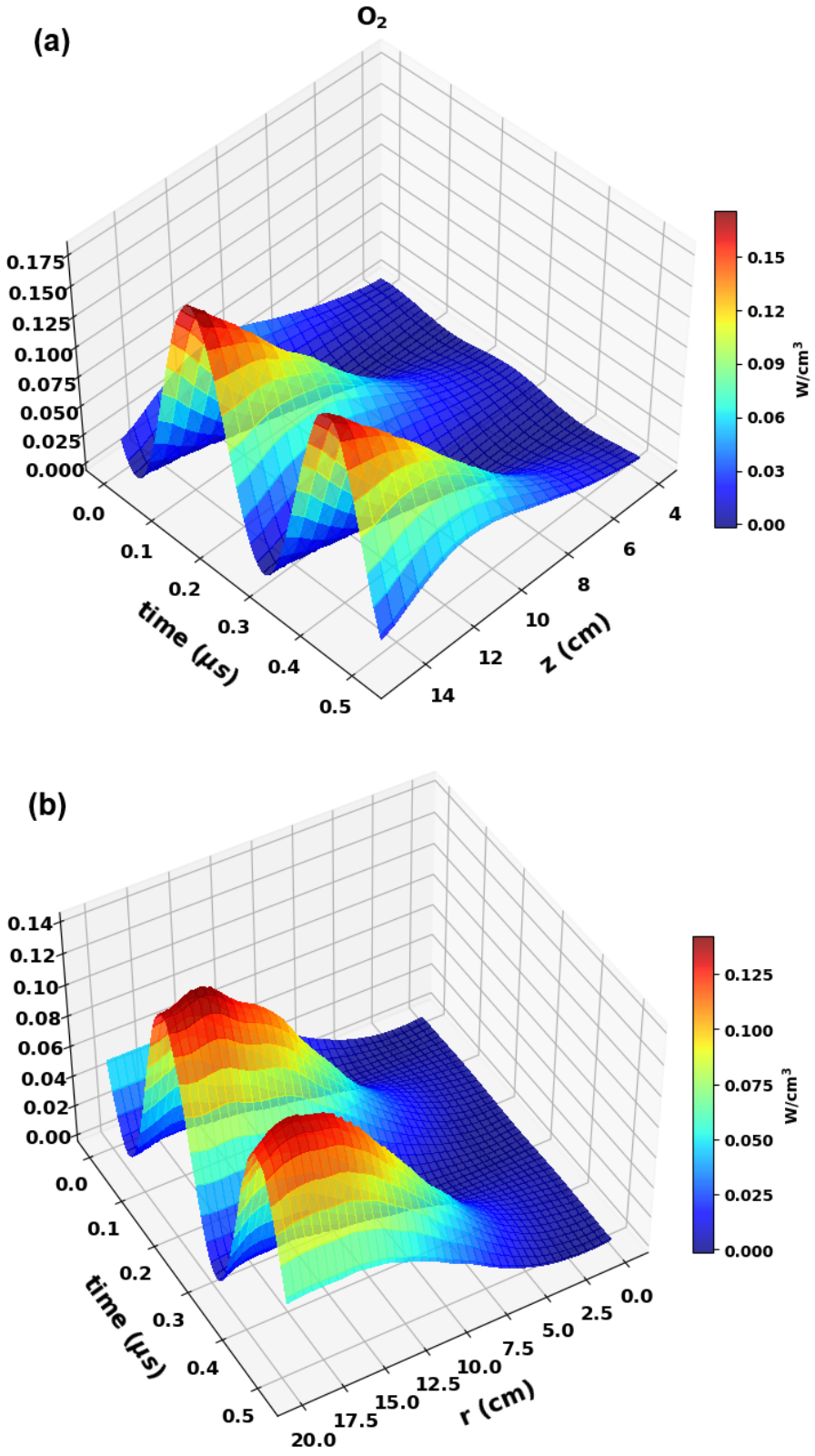

Figure 58: Power density in Ar plasma during one RF cycle (a) at different axial position (b) at different radial position. The plots were obtained similarly to Figure 57.

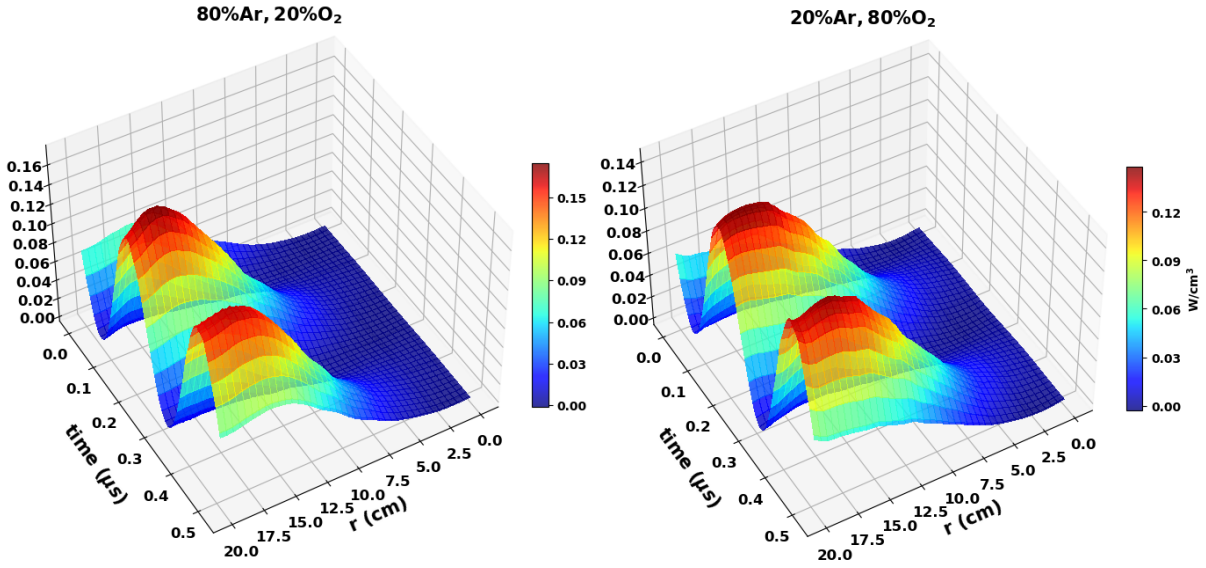

Figure 59: Power density in 80% Ar 20% O_2 plasma during one RF cycle at different radial position, averaged over z.

6 Conclusion

The thesis presents a comprehensive investigation on a pulsed ICP etch tool using Ar/O_2 gas mixture. Argon is the the most commonly used noble gas in industrial applications. O_2 is an exemplary electronegative gas that is widely used for surface processing in semiconductor industry. ICP systems are highly sensitive to various operating conditions such as chamber geometry, applied power, gas pressure, etc. Electronegative gas discharge produces negative ions and therefore further complicates the system. The kinetics are usually multi-dimensional, and the plasma parameters temporally evolve during pulsed operation. The diagnostics and measurement described in this thesis aimed to characterize the plasma in a cylindrical ICP etch tool powered by a planar coil, with high spatial resolution and temporal resolution. Key features such as ion energy and sheath dynamics were studied. Important parameters including electron density, negative ion density, electromagnetic field distribution and power deposition were reported for different mixing ratio of argon and oxygen gas.

For a precise, uniform and repeatable etch result, fine control over the plasma profile is necessary. The recent development on ICP etch tools separates the parameter space of the device into two parts. The source power applied to the entire reactor controls the plasma generation and plasma density. The bias power applied on the wafer controls the ion energy that etch the wafer surface. The source and the bias can be decoupled, and their effects in an ICP can be relatively independent when the frequencies are different. It therefore makes sense to separate the experimental investigations into two regions: the bulk plasma which has important interactions with the planar coil on the top; the plasma sheath which is in contact with the wafer placed at the bottom of the chamber.

Phase-resolved LIF experiment were performed on the thin plasma volume above the Si wafer. A fast CCD camera captured the 2D LIF signal with a spatial resolution of 0.018 cm $\times$ 0.018 cm / pixel. Two dimensional mapping of the argon ion energy distribution and drift velocity were achieved by sending the laser horizontally along the wafer, and then vertically towards the wafer.

Data was collected with a 1 MHz sinuisoidally biased or unbiased wafer, during the

plasma glow or in the plasma afterglow, and the different cases were compared. A direct measurement on the voltage of the wafer shows large negative DC self-bias which is desirable to accelerate the positive ions. The sheath thickness was measured. The sheath dynamics closely followed the instantaneous bias waveform with a phase shift.

In all cases of bias conditions, ions were cold in horizontal direction. When the wafer was not biased, the vertical IEDs has a single peak located at the bulk drift velocity when the wafer was not biased. When the wafer bias was turned on during the afterglow, the vertical IEDs were bimodal distributions with two well separated peaks: a low energy peak at the thermal drift velocity, and a high energy peak approaching the wafer bias potential. When the bias was turned on during the plasma glow, the vertical IED had a long tail with a continuum of particles with energies up to the bias voltage. An analysis on the angles of the bulk drift and high energy ions shows that in the afterglow, high energy ions have smaller incident angles and strike the wafer more uniformly near the edge of the wafer. A simulation model extended the experimental results at 0.5 mTorr to the industry relevant regime at higher pressure.

In the bulk region of the plasma, plasma parameters were measured and compared in different ratios of Ar/O_2 gas. Electron density on half of the rz plane (azimuthal symmetry was assumed) was measured by a hairpin probe, and partly by an RF compensated Langmuir probe in the region that saturated the hairpin probe. Electronegativity parameter $\alpha = n_-/n_e$ on the same data plane were measured by the saturation current method using the RF compensated Langmuir probe and photodetachment technique assisted with the hairpin probe.

Electron densities show significantly different spatial distribution in pure argon plasma and oxygen containing plasma. In quasi-steady state pure argon plasma, electron distribution is not affected by the coil geometry and forms a ellipsoid shape close to the center of the chamber. The total density was significantly reduced when oxygen was added. Electron density profile shifts its peak and formed a ring shape under the coil. A temporal investigation on the electron density distribution at the onset of the pulse during the E-H transition phase shows that Ar/O_2 plasmas have significantly smoother

transitions than pure Ar plasma.

Direct measurement of electronegativity confirmed that the plasma core is predominantly electronegative. The peak electronegativity was generally found at the center of the chamber. With the increasing oxygen content, negative ions are more uniformly distributed across the chamber.

The distribution of electrons and negative ions merits the further discussion on the induced field distribution inside the chamber. Propagation of electromagnetic field, induced current and power deposition were obtained from Bdot probe measurement on the half rz plane. Magnetic field lines and current density pattern show significant modulation by the addition of oxygen, in good agreement with the electron density distribution measurement. The field penetrates deeper with the addition of oxygen, resulting in smoother spatial gradient in electron density. The density patterns of the azimuthal current during half RF cycle were also compared.

The phase-averaged inductive power density $J_\phi E_\phi$ shows deeper deposition towards the plasma volume in oxygen compared to pure argon. A phase-resolved investigation shows similar pattern comparison as seen for current density. An interesting finding is that the power density in oxygen plasma during the first cycle and the second cycle is asymmetric in the region under the coil. The asymmetric is increasingly prominent as the oxygen content increases.

Further study should focus on a greater variety of operating conditions and other industry relevant electronegative gases such as Cl_2 and SF_6. LIF measurement can be performed with non-sinuisoidal wafer bias, which gathers much interest recently in the industry. Different combinations of power source frequency and bias frequency are also essential to the ICP operation and their resulting effect on plasma parameters deserve more experimental study.

References

[1] V. Donnelly and A. Kornblit, "Plasma etching: yesterday, today and tomorrow", J. Vac. Sci. Technol **A 31(5)**, 050825-1-050825–48 (2013).

[2] K. Nojiri, *Dry etching technology for semiconductors*, trans. by Y. Ikezi. Original work published 2012 (Springer Cham, New York, 2014) Chap. 2, p. 17.

[3] J. W. Coburn, "Plasma-assisted etching", Plasma Chem Plasma Process **2**, 1–41 (1982).

[4] D. J. Economou, "Pulsed plasma etching for semiconductor manufacturing", J. Phys. D: Appl. Phys. **47**, 303001 (2014).

[5] K. J. Kanarik, S. Tan, W. Yang, I. L. Berry, Y. Pan, and R. A. Gottscho, "Universal scaling relationship for atomic layer etching", J. Vac. Sci. Technol. A **39**, 010401 (2020).

[6] B. Wu, A. Kumar, and S. Pamarthy, "High aspect ratio silicon etch: A review", J. Appl. Phys. **108**, 051101 (2010).

[7] K. J. Kanarik, T. Lill, E. A. Hudson, S. Sriraman, S. Tan, J. Marks, V. Vahedi, and R. A. Gottscho, "Overview of atomic layer etching in the semiconductor industry", J. Vac. Sci. Technol. A **33**, 020802 (2015).

[8] S. Banna, A. Agarwal, G. Cunge, M. Darnon, E. Pargon, and O. Joubert, "Pulsed high-density plasmas for advanced dry etching processes", J. Vac. Sci. Technol A **30**, 040801 (2012).

[9] S. Rauf and M. J. Kushner, "Nonlinear dynamics of radio frequency plasma processing reactors powered by multifrequency sources", IEEE Transactions on Plasma Science **27**, 1329–1338 (1999).

[10] A. Mishra, K. N. Kim, T. H. Kim, and G. Y. Yeom, "Synergetic effects in a discharge produced by a dual frequency–dual antenna large-area ICP source", Plasma Sources Sci. Technol. **21**, 035018 (2012).

[11] N. Sirse, A. Mishra, G. Y. Yeom, and A. R. Ellingboe, "Electron density modulation in a pulsed dual-frequency (2/13.56 MHz) dual-antenna inductively coupled plasma discharge", J. Vac. Sci. Technol. A **34**, 051302 (2016).

[12] P. Jiang, D. J. Economou, and C. B. Shin, "Effect of power modulation on radical concentration and uniformity in a single-wafer plasma reactor", Plasma Chem Plasma Process **15**, 383–408 (1995).

[13] R. A. Gottscho, C. W. Jurgensen, and D. J. Vitkavage, "Microscopic uniformity in plasma etching", J. Vac. Sci. Technol. B **10**, 2133–2147 (1992).

[14] C. G. N. Lee, K. J. Kanarik, and R. A. Gottscho, "The grand challenges of plasma etching: a manufacturing perspective", J. Phys. D: Appl. Phys. **47**, 273001 (2014).

[15] P. Subramonium and M. J. Kushner, "Pulsed inductively coupled plasmas as a method to recoup uniformity: Three-dimensional modeling study", Appl. Phys. Lett. **85**, 721–723 (2004).

[16] S. Samukawa, K. Noguchi, J. I. Colonell, K. H. A. Bogart, M. V. Malyshev, and V. M. Donnelly, "Reduction of plasma induced damage in an inductively coupled plasma using pulsed source power", J. Vac. Sci. Technol. B **18**, 834–840 (2000).

[17] K. Hashimoto, "Charge Damage Caused by Electron Shading Effect", Jpn. J. Appl. Phys. **33**, 6013 (1994).

[18] X. V. Qin, Y.-H. Ting, and A. E. Wendt, "Tailored ion energy distributions at an rf-biased plasma electrode", Plasma Sources Sci. Technol. **19**, 065014 (2010).

[19] T. Faraz, Y. G. P. Verstappen, M. A. V. A. Marcel, N. J. Chittock, J. E. Lopez, E. Heijdra, W. J. H. van Gennip, W. M. M. Kessels, and A. J. M. Mackus, "Precise ion energy control with tailored waveform biasing for atomic scale processing", J. Appl. Phys. **128**, 213301 (2020).

[20] F. Krüger, H. Lee, S. K. Nam, and M. J. Kushner, "Voltage waveform tailoring for high aspect ratio plasma etching of SiO2 using Ar/CF4/O2 mixtures: Consequences of low fundamental frequency biases", Phys. Plasmas **31**, 033508 (2024).

[21] D.Flamm, “Mechanisms of silicon etching in fluorine- and chlorine-containing plasmas”, Pure Appl. Chem **62**, 1709–1720 (1990).

[22] S. A. Vitale, H. Chae, and H. H. Sawin, “Silicon etching yields in F_2, Cl_2, Br_2 and HBr high density plasmas”, J. Vac. Sci. Technol. A **19**, 2197–2206 (2001).

[23] B. J. Lee, A. Efremov, and K.-H. Kwon, “Plasma parameters, gas-phase chemistry and Si/SiO_2 etching mechanisms in $HBr + Cl_2 + O_2$ gas mixture: effect of HBr/O_2 mixing ratio”, Vacuum **163**, 110–118 (2019).

[24] K.Racka-Szmidt, B. Stonio, J. Żelazko, M. Filipiak, and M. S. Mariusz, “A review: inductively coupled plasma reactive ion etching of silicon carbide”, Materials **15**, 10.3390/ma15010123 (2022).

[25] R. N. Franklin, “Electronegative plasmas—why are they so different?”, Plasma Sources Sci. Technol. **11**, A31 (2002).

[26] M. Bacal and H. J. Doucet, “Generation of negative ion-rich plasma in electronegative gases (oxygen)”, Vacuum **24**, 595–600 (1974).

[27] E. Stoffels, W. W. Stoffels, D. Vender, M. Kando, G. M. W. Kroesen, and F. J. de Hoog, “Negative ions in a radio-frequency oxygen plasma”, Phys. Rev. E **51**, 2425–2435 (1995).

[28] D. Vender, W. W. Stoffels, E. Stoffels, G. M. W. Kroesen, and F. J. de Hoog, “Charged-species profiles in electronegative radio-frequency plasmas”, Phys. Rev. E **51**, 2436–2444 (1995).

[29] H. Amemiya, “Diagnostics of negative ions using probe and laser in plasmas (oxygen discharge)”, Vacuum **58**, 100–116 (2000).

[30] C. S. Corr and S. Gomez and W. G. Graham, “Discharge kinetics of inductively coupled oxygen plasmas: experiment and model”, Plasma Sources Sci. Technol. **21**, 055024 (2012).

[31] J. Schulze, T. Gans, D. O'Connell, U. Czarnetzki, A. R. Ellingboe, and M. M. Turner, "Space and phase resolved plasma parameters in an industrial dual-frequency capacitively coupled radio-frequency discharge", J. Phys. D: Appl. Phys. **40**, 7008 (2007).

[32] D. O'Connell, K. Niemi1, M. Zaka-ul-Islam, and T. Gans, "Space and phase resolved optical emission in mode transitions of radio-frequency inductively coupled plasmas", J. Phys.: Conf. Ser. **162**, SECOND INTERNATIONAL WORKSHOP ON NON-EQUILIBRIUM PROCESSES IN PLASMAS AND ENVIRONMENTAL SCIENCE 23–26 8ust 2008, Belgrade and Novi Sad, Serbia, 012011 (2009).

[33] A. Mishra and M. H. Jeon and K. N. Kim and G. Y. Yeom, "An investigation of the temporal evolution of plasma potential in a 60 mhz/2 mhz pulsed dual-frequency capacitively coupled discharge", Plasma Sources Sci. Technol. **21**, 055006 (2012).

[34] Y. Mitsui and T. Makabe, "Review and current status: e h mode transition in low-temperature icp and related electron dynamics", Plasma Sources Sci. Technol. **30**, 023001 (2021).

[35] C. Wild and P. Koidl, "Ion and electron dynamics in the sheath of radio-frequency glow discharges", J. Appl. Phys. **69**, 2909–2922 (1991).

[36] D. Gahan, B. Dolinaj, and M. B. Hopkins, "Retarding field analyzer for ion energy distribution measurements at a radio-frequency biased electrode", Rev. Sci. Instrum. **79**, 033502 (2008).

[37] G. Cunge, M. Darnon, J. Dubois, P. Bezard, O. Mourey, C. Petit-Etienne, L. Vallier, E. Despiau-Pujo, and N. Sadeghi, "Measuring ion velocity distribution functions through high-aspect ratio holes in inductively coupled plasmas", Appl. Phys. Lett. **108**, 093109 (2016).

[38] A. Hallil, O. Zabeida, M. R. Wertheimer, and L. Martinu, "Mass-resolved ion energy distributions in continuous dual mode microwave/radio frequency plasmas in argon and nitrogen", J. Vac. Sci. Technol. A **18**, 882–890 (2000).

[39] M. A. Sobolewski, Y. Wang, and A. Goyette, "Measurements and modeling of ion energy distributions in high-density, radio-frequency biased discharges", J. Appl. Phys. **91**, 6303–6314 (2002).

[40] D. O'Connell, R. Zorat, A. R. Ellingboe, and M. M. Turner, "Comparison of measurements and particle-in-cell simulations of ion energy distribution functions in a capacitively coupled radio-frequency discharge", Phys. Plasmas **14**, 103510 (2007).

[41] A. Baby1, C. M. O. Mahony, P. Lemoine, and P. D. Maguire, "Acetylene–argon plasmas measured at an rf-biased substrate electrode for diamond-like carbon deposition: ii. ion energy distributions", Plasma Sources Sci. Technol. **20**, 015004 (2011).

[42] A. O'Keefe and D. A. G. Deacon, "Cavity ring-down optical spectrometer for absorption measurements using pulsed laser sources", Rev. Sci. Instrum. **59**, 2544–2551 (1988).

[43] D. McCarren and E. Scime, "Continuous wave cavity ring-down spectroscopy for velocity distribution measurements in plasma", Rev. Sci. Instrum. **86**, 103505 (2015).

[44] D. N. Hill, S. Fornaca, and M. G. Wickham, "Single frequency scanning laser as a plasma diagnostic", Rev. Sci. Instrum. **54**, 309–314 (1983).

[45] N. Moore, W. Gekelman, and P. Pribyl, "Ion energy distribution function measurements by laser-induced fluorescence in a dual radio frequency sheath", Jour. Vac. Soc. and Technol **A 32(2)**, 012303 (2016).

[46] R. A. Stern and I. J. A. Johnson, "Plasma ion diagnostics using resonant fluorescence", Phys. Rev. Lett. **34**, 1548 (1975).

[47] Y. Wang, M. Kushner, N. Moore, W. Gekelman, and P. Pribyl, "Space and phase resolved ion energy and angular distributions in single and dual-frequency capacitively coupled plasmas", Jour. Vac. Soc. and Technol. **A 31(6)**, 265001 (2013).

[48] B. Jacobs, W. Gekelman, P. Pribyl, and M. Barnes, "Temporally resolved ion velocity distributions within a radio-frequency plasma sheath", Phys. Plasnmas **18**, 053503 (2011).

[49] B. Jacobs, W. Gekelman, P. Pribyl, and M. Barnes, "Phase-resolved measurements of ion velocity in a radio-frequency sheath", Phys. Rev. Letts. **105**, 075001 (2010).

[50] M. Goeckner, J. Goree, and T. Sheridan, "Laser induced fluorescence characterization of a multidipole filament plasma", Phys. Fluids B **3**, 2913 (1991).

[51] J. Han, P. Pribyl, W. Gekelman, and A. Paterson, "Three-dimensional measurements of fundamental plasma parameters in pulsed icp operation", Phys. Plasmas **27**, 063509 (2020).

[52] S. Rauf, J. Kenney, Z. Chen, K. Bera, A. Agarwal, A. Balakrishna, and K. Collins, "Modeling of Plasma Processing Equipment—Current Trends and Challenges", AIP Conference Proceedings **1333**, 1019–1026 (2011).

[53] H. C. Kim, F. Iza, S. S. Yang, M. Radmilović-Radjenović, and J. K. Lee, "Particle and fluid simulations of low-temperature plasma discharges: benchmarks and kinetic effects", J. Phys. D: Appl. Phys **38**, R283 (2005).

[54] T. Piskin, Y. Qian, P. Pribyl, W. Gekelman, and M. J. Kushner, "E–H transitions in Ar/O2 and Ar/Cl2 inductively coupled plasmas: Antenna geometry and operating conditions", J, Appl. Phys **133**, 173302 (2023).

[55] S. Lanham, J. Polito, Z. Xiong, U. R. Kortshagen, and M. J. Kushner, "Pulsed power to control growth of silicon nanoparticles in low temperature flowing plasmas", J, Appl. Phys **132**, 073301 (2022).

[56] C. Qu, Y. Sakiyama, P. Agarwal, and M. J. Kushner, "Plasma-enhanced atomic layer deposition of SiO2 film using capacitively coupled Ar/O2 plasmas: A computational investigation", J. Vac. Sci. Technol. A **39**, 052403 (2021).

[57] S.-M. Jung, J. Jang, W. Cho, H. Cho, J. Jeong, Y. Chang, J. Kim, Y. Rah, Y. Son, J. Park, M.-S. Song, K.-H. Kim, J.-S. Lim, and K. Kim, "Three dimensionally stacked nand flash memory technology using stacking single crystal si layers on ild and tanos structure for beyond 30nm node", in Iedm tech. dig. (2006), pp. 37–40.

[58] S. I. Shim, J. Jang, and J. Song, "Trends and future challenges of 3d nand flash memory", in Proceedings of 2023 ieee international memory workshop, monterey, ca, usa (2023).

[59] J. W. Han, S. H. Park, M. Y. Jeong, K. S. Lee, K. N. Kim, H. J. Kim, J. C. Shin, S. M. Park, S. H. Shin, S. W. Park, K. S. Lee, J. H. Lee, S. H. Kim, B. C. Kim, M. H. Jung, I. Y. Yoon, H. Kim, S. U. Jang, K. J. Park, and Y. K. K. et al., "Ongoing evolution of dram scaling via third dimension -vertically stacked dram", in Proceedings of 2023 ieee symposium on vlsi technology and circuits, kyoto, japan (2023).

[60] J. Han, "Study of fundamental plasma properties in an inductively coupled plasma device", Doctoral Dissertation (University of California, Los Angeles, 2020).

[61] D. Leneman and W. Gekelman, "A novel angular motion vacuum feedthrough", Rev. Sci. Instrum. **72**, 3473–3474 (2001).

[62] F. F. Chen, *Lecture notes on langmuir probe diagnostics*, 2003.

[63] V. A. Godyak and V. I. Demidov, "Probe measurements of electron-energy distributions in plasmas: what can we measure and how can we achieve reliable results?", J. Phys. D: Appl. Phys. **44**, 233001 (2011).

[64] S. Ghosh, P. K. Chattopadhyay, J. Ghosh, and D. Bora, "Rf compensation of single langmuir probe in low density helicon plasma", Fusion Engineering and Design **112**, 915–918 (2016).

[65] C. L. Onga, O. H. China, M. Nisoab, and B. Paosawatyanyangc, "Langmuir probe measurement in a radio frequency inductively coupled argon plasma", Jurnal Fizik Malaysia **25**, 97–102 (2004).

[66] A. Azooz, Y. Al- Jawaady, and Z. Ali, "Langmuir probe rf plasma compensation using a simulation method", Comput. Phys. Commun **185**, 350–356 (2014).

[67] R. R. J. Gagné and A. Cantin, "Investigation of an rf plasma with symmetrical and asymmetrical electrostatic probes", J. Appl. Phys. **43**, 2639–2647 (1972).

[68] V. A. Godyak and R. B. Piejak, "Probe measurements of the space potential in a radio frequency discharge", J. Appl. Phys. **68**, 3157–3162 (1990).

[69] F. F. Chen, "Time-varying impedance of the sheath on a probe in an rf plasma", Plasma Sources Sci. Technol. **15**, 773 (2006).

[70] I. Sudit and F. F. Chen, "Rf compensated probes for high-density discharges", Plasma Sources Sci. Technol. **3**, 162–168 (1994).

[71] A. A. Kudryavtsev, V. I. Demidov, C. A. D. Jr., S. F. Adams, and K. Y. Serditov, "Probe measurements in electronegative plasmas: modeling the perturbative effects of the probe-holder", Contributions to Plasma Physics **49**, 373–380 (2009).

[72] H. Amemiya, "Plasmas with negative ions-probe measurements and charge equilibrium", J. Phys. D: Appl. Phys. **23**, 999 (1990).

[73] J. Bredin, P. Chabert, and A. Aanesland, "Langmuir probe analysis of highly electronegative plasmas", Applied Physics Letters **102**, 154107 (2013).

[74] R. B. Piejak, V. A. Godyak, R. G. B. M. Alexandrovich, and N. Sternberg, "Radiofrequency discharge benchmark model comparison", J. Appl. Phys. **95**, 3785 (2004).

[75] B. L. Sands, N. S. Siefert, and B. N. Ganguly, "Design and measurement considerations of hairpin resonator probes for determining electron number density in collisional plasmas", Plasma Sources Sci. Technol. **16**, 716 (2007).

[76] J. Conway, N. Sirse, S. K. Karkari, and M. M. Turner, "Using the resonance hairpin probe and pulsed photodetachment technique as a diagnostic for negative ions in oxygen plasma", Plasma Sources Sci. Technol. **19**, 065002 (2010).

[77] J. W. Bradley, R. Dodd, S.-D. You, N. Sirse, and S. K. Karkari, "Resonance hairpin and langmuir probe-assisted laser photodetachment measurements of the negative ion density in a pulsed dc magnetron discharge", J. Vac. Sci. Technol. A **29**, 031305 (2011).

[78] A. K. Pandey, J. K. Joshi, and S. K. Karkari, "Inferring plasma parameters from the sheath characteristics of a dc biased hairpin probe", Plasma Sources Sci. Technol. **29**, 015009 (2020).

[79] S. L. GMBH, *Mix. rhodamine b / 101*, `https://www.sirah.com/accessories/dyes/dye-mix-rhodamine-b-101/#hrr-532/` (visited on 08/07/2024).

[80] B. W. Jacobs, "Phase-resolved measurements of ion dynamics in radio frequency plasma sheaths by laser-induced fluorescence", Doctoral Dissertation (University of California, Los Angeles, 2010).

[81] O. Tudisco, A. L. Fabris, C. Falcetta, L. Accatino, R. D. Angelis, M. Manente, F. Ferri, M. Florean, C. Neri, C. Mazzotta, D. Pavarin, F. Pollastrone, G. Rocchi, A. Selmo, L. Tasinato, F. Trezzolani, and A. A. Tuccillo, "A microwave interferometer for small and tenuous plasma density measurements", Rev. Sci. Instrum. **84**, 033505 (2013).

[82] E. E. Scime, R. F. Boivin, J. L. Kline, and M. M. Balkey, "Microwave interferometer for steady-state plasmas", Review of Scientific Instruments **72**, 1672–1676 (2001).

[83] S.-H. Seo, "The line integrated density measurement by using a frequency sweep interferometer", Fusion Engineering and Design **190**, 113501 (2023).

[84] M. Lieberman and A. Lichtenberg, *Principals of plasma discharges and materials processing*, edited by E. Beutler, M. A. Lichtman, B. W. Coller, and T. S. Kipps (John Wiley and Sons, New York, 1994) Chap. 5, p. 165.

[85] J. Upadhyay, J. Peshl, S. Popović, A. .-M. Valente-Feliciano, and L. Vušković, "Effect of self-bias on cylindrical capacitive discharge for processing of inner walls of tubular structures—Case of SRF cavities", AIP Advances **8**, 085008 (2018).

[86] J.-H. Kim, Y.-H. Shin, and K.-H. Chung, "Study on self-bias voltage induced on the substrate by r.f. bias power in a high density plasma", Thin Solid Films **435**, Proceedings of the Joint International Plasma Symposium of the 6th APCPST, the 15th SPSM and the 11th Kapra Symposia, 288–292 (2003).

[87] J. W. Coburn and E. Kay, "Positive-ion bombardment of substrates in rf diode glow discharge sputtering", Journal of Applied Physics **43**, 4965–4971 (1972).

[88] T. Panagopoulos and D. J. Economou, "Plasma sheath model and ion energy distribution for all radio frequencies", J. Appl. Phys. **85**, 3435–3443 (1999).

[89] S. B. Wang and A. E. Wendt, "Sheath thickness evaluation for collisionless or weakly collisional bounded plasmas", IEEE Trans. Plasma Sci. **27**, 1358 (1999).

[90] E. Kawamura, V. Vahedi, M. A. Lieberman, and C. K. Birdsall, "Ion energy distributions in rf sheaths; review, analysis and simulation", Plasma Sources Sci. Technol. **8**, R45 (1999).

[91] A. Metze, D. W. Ernie, and H. J. Oskam, "Application of the physics of plasma sheaths to the modeling of rf plasma reactors", J. Appl. Phys. **60**, 3081–3087 (1986).

[92] P. Benoit-Cattin and L.-C. Bernard, "Anomalies of the Energy of Positive Ions Extracted from High-Frequency Ion Sources. A Theoretical Study", J. of Appl. Phys. **39**, 5723–5726 (1968).

[93] R. J. Belen, S. Gomez, M. Kiehlbauch, and E. S. Aydil, "In situ measurement of the ion incidence angle dependence of the ion-enhanced etching yield in plasma reactors", J. Vac. Sci. Technol. A **24**, 2176–2186 (2006).

[94] I. Seong, J. Lee, S. Kim, Y. Lee, C. Cho, J. Lee, W. Jeong, Y. You, and S. You, "Characterization of an etch profile at a wafer edge in capacitively coupled plasma", Nanomaterials **12**, 3963 (2022).

[95] D. Marger and H. Schmoranzer, "Precision lifetime measurements of ar ii 4p doublet levels", Phys. Letts. A **146**, 502–506 (1990).

[96] F. Chu, R. Hood, and F. Skiff, "Measurement of wave particle interaction and metastable lifetime using laser induced fluorescence", Phys. Plasmas **26**, 042111 (2019).

[97] P. Diomede, M. Nikolaou, and D. J. Economou, "Voltage waveform to achieve a desired ion energy distribution on a substrate in contact with plasma", Plasma Sources Sci. Technol. **20**, 045011 (2011).

[98] E. A. Edelberg and E. S. Aydil, "Modeling of the sheath and the energy distribution of ions bombarding rf-biased substrates in high density plasma reactors and comparison to experimental measurements", J. Appl. Phys. **86**, 4799–4812 (1999).

[99] P. A. Miller and M. E. Riley, "Dynamics of collisionless rf plasma sheaths", J. of Appl. Phys. **82**, 3689–3709 (1997).

[100] O. Dutuit, C. Alcaraz, D. Gerlich, P. M. Guyon, J. Hepburn, C. Métayer-Zeitoun, J. B. Ozenne, M. Schweizer, and T. Weng, "A state-selected study of $Ar^+(^2P_{3/2,1/2})$ + O^2 charge transfer at collision energies below 4 ev using synchrotron radiation and guided beam techniques", Chem. Phys. **209**, 177–194 (1996).

[101] D. Benyoucef and M. Yousfi, "Ar^+/Ar, O_2^+/O_2 and N_2^+/N_2 elastic momentum collision cross sections: calculation and validation using the semi-classical model", Plasma Sci. Technol. **16**, 588 (2014).

[102] R. Hood, S. D. Baalrud, R. L. Merlino, and F. Skiff, "Laser-induced fluorescence measurements of ion fluctuations in electron and ion presheaths", Physics of Plasmas **27**, 053509 (2020).

[103] M. J. Kushner, "Hybrid modelling of low temperature plasmas for fundamental investigations and equipment design", J. Phys. D: Appl. Phys **42**, 194013 (2009).

[104] Y. Qian, W. Gekelman, P. Pribyl, T. Piskin, and A. Paterson, "Ion motion above a biased wafer in a plasma etching reactor", Physics of Plasmas **31**, 063507 (2024).

[105] C. Lee, D. B. Graves, M. A. Lieberman, and D. W. Hess, "Global model of plasma chemistry in a high density oxygen discharge", J. Electrochem. Society **141**, 1546 (1994).

[106] J. T. Gudmundsson, I. G. Kouznetsov, K. K. Patel, and M. A. Lieberman, "Electronegativity of low-pressure high-density oxygen discharges", J. Phys. D: Appl. Phys. **34**, 1100 (2001).

[107] H. M. Katsch, C. Manthey, and H. F. Döbele, "Charge carrier dynamics in a pulsed inductive rf discharge in oxygen", Plasma Sources Sci. Tech. **12**, 475 (2003).

[108] J. T. Gudmundsson and E. G. Thorsteinsson, "Oxygen discharges diluted with argon: dissociation processes", Plasma Sources Sci. Tech **16**, 399 (2007).

[109] M. Shindo, S. Uchino, R. Ichiki, S. Yoshimura, and Y. Kawai, "Measurements of the negative ion density in SF6/Ar plasma using a plane electrostatic probe", Review of Scientific Instruments **72**, 2288–2293 (2001).

[110] H. Amemiya, B. M. Annaratone, and J. E. Allen, "The collection of positive ions by spherical and cylindrical probes in an electronegative plasma", Plasma Sources Sci. Technol. **8**, 179 (1999).

[111] K. Tsumori and M. Wada, "Diagnostics tools and methods for negative ion source plasmas, a review", New Journal of Physics **19**, 045002 (2017).

[112] H. Nakano, K. Tsumori, M. Shibuya, S. Geng, M. Kisaki, K. Ikeda, K. Nagaoka, M. Osakabe, Y. Takeiri, and O. Kaneko, "Cavity ringdown technique for negative-hydrogen-ion measurement in ion source for neutral beam injector", Journal of Instrumentation **11**, C03018 (2016).

[113] M. Barbisan, R. Pasqualotto, R. Agnello, M. Pilieci, G. Serianni, C. Taliercio, V. Cervaro, FRossetto., and A. Tiso, "Development and first operation of a cavity ring down spectroscopy diagnostic in the negative ion source SPIDER", Review of Scientific Instruments **92**, 053507 (2021).

[114] G. A. Hebner and I. C. Abraham, "Characterization of electron and negative ion densities in fluorocarbon containing inductively driven plasmas", Journal of Applied Physics **90**, 4929–4937 (2001).

[115] M. Hasani, Z. Marvi, and J. Beckers, "Probing negative ions and electrons in the afterglow of a low-pressure oxygen radiofrequency plasma using laser-induced photodetachment", Journal of Physics D: Applied Physics **54**, 495202 (2021).

[116] J.-B. Lee, S.-H. Seo, and H.-Y. Chang, "Time evolution of electronegativity in a pulsed inductively coupled oxygen plasma", Thin Solid Films **518**, Proceedings of the 2nd International Conference on Microelectronics and Plasma Technology – ICMAP 2009, 6573–6577 (2010).

[117] M. Zanáška, Z. Turek, Z. Hubička, M. Čada, P. Kudrna, and M. Tichý, "Floating harmonic probe for diagnostic of pulsed discharges", Surface and Coatings Technology **357**, 879–885 (2019).

[118] N. Sirse, S. K. Karkari, and M. M. Turner, "Probing negative ion density and temperature using a resonance hairpin probe", Plasma Sources Sci. Technol. **24**, 022001 (2015).

[119] J. T. Gudmundsson, T. Kimura, and M. A. Lieberman, "Experimental studies of o2/ar plasma in a planar inductive discharge", Plasma Sources Sci. and Tech. **8**, 22 (1999).

[120] S. Rauf and M. J. Kushner, "Argon metastable densities in radio frequency Ar, Ar/O2 and Ar/CF4 electrical discharges", Journal of Applied Physics **82**, 2805–2813 (1997).

[121] X. Han, X. Wei, H. Xu, W. Zhang, Y. Li, Y. Li, and Z. Yang, "Investigation on the parameter distribution of ar/o2 inductively coupled plasmas", Vacuum **168**, 108821 (2019).

[122] H. J. Yoon, T. H. Chung, and D. C. Seo, "Two-dimensional fluid simulation and langmuir probe measurement of a planar inductively coupled oxygen plasma", Japanese J. Appl. Phys. **38**, 6890 (1999).

[123] I. M. El-Fayoumi and I. R. Jones, "Theoretical and experimental investigations of the electromagnetic field within a planar coil, inductively coupled rf plasma source", Plasma Sources Sci. Technol. **7**, 162 (1998).

[124] U. Kortshagen, C. Busch, and L. D. Tsendin, "On simplifying approaches to the solution of the boltzmann equation in spatially inhomogeneous plasmas", Plasma Sources Science and Technology **5**, 1 (1996).

[125] V. Vahedi, M. A. Lieberman, G. DiPeso, T. D. Rognlien, and D. Hewett, "Analytic model of power deposition in inductively coupled plasma sources", Journal of Applied Physics **78**, 1446–1458 (1995).

[126] S.-H. Seo, C. Chung, and H.-Y. Chang, "Review of heating mechanism in inductively coupled plasma", Surface and Coatings Technology **131**, Proceedings of the 2nd Asian-European International Conference on Plasma surface Engineering, 1–11 (2000).

[127] M. M. Turner, "Collisionless heating in radio-frequency discharges: a review", J. Phys. D: Appl. Phys. **42**, 194008 (2009).

[128] S. Rauf and M. J. Kushner, "Model for noncollisional heating in inductively coupled plasma processing sources", J. Appl. Phys. **81**, 5966–5974 (1997).

[129] G. J. M. Hagelaar, "Effective-viscosity approach for nonlocal electron kinetics in inductively coupled plasmas", Phys. Rev. Lett. **100**, 025001 (2008).

[130] M. M. Turner, "Collisionless electron heating in an inductively coupled discharge", Phys. Rev. Lett. **71**, 1844–1847 (1993).

[131] V. I. Kolobov and D. J. Economou, "The anomalous skin effect in gas discharge plasmas", Plasma Sources Sci. and Tech. **6**, R1 (1997).

[132] V. A. Godyak and V. I. Kolobov, "Negative power absorption in inductively coupled plasma", Phys. Rev. Lett. **79**, 4589–4592 (1997).

[133] Z. F. Ding, B. Sun, and W. G. Huo, "Characteristics of anomalous skin effect and evolution of power absorption regions in a cylindrical radio frequency inductively coupled plasma", Phys. Plasmas **22**, 063504 (2015).

[134] R. A. Stewart, P. Vitello, D. B. Graves, E. F. Jaeger, and L. A. Berry, "Plasma uniformity in high-density inductively coupled plasma tools", Plasma Sources Sci. Tech. **4**, 36 (1995).

[135] L. J. Mahoney, A. E. Wendt, E. Barrios, C. J. Richards, and J. L. Shohet, "Electron-density and energy distributions in a planar inductively coupled discharge", J. Appl. Phys. **76**, 2041–2047 (1994).

[136] M. Vass, S. Wilczek, T. Lafleur, R. P. Brinkmann, Z. D., and J. Schulze, "Electron power absorption in low pressure capacitively coupled electronegative oxygen radio frequency plasmas", Plasma Sources Science and Technology **29**, 025019 (2020).

[137] M.-H. Lee, H.-C. Lee, and C.-W. Chung, "Comparison of pressure dependence of electron energy distributions in oxygen capacitively and inductively coupled plasmas", Phys. Rev. E **81**, 046402 (2010).

[138] M.-H. Lee, H.-C. Lee, and C.-W. Chung, "Effect of adding small amount of inductive fields to O2, Ar/O2 capacitively coupled plasmas", J. Appl. Phys. **111**, 093301 (2012).

[139] W. Liu, D.-Q. Wen, S.-X. Zhao, F. Gao, and Y.-N. Wang, "Characterization of o2/ar inductively coupled plasma studied by using a langmuir probe and global model", Plasma Sources Sci. Tech. **24**, 025035 (2015).

[140] T. Wegner, C. Küllig, and J. Meichsner, "Electron heating during e-h transition in inductively coupled rf plasmas", Plasma Sources Sci. Tech. **24**, 044001 (2015).

[141] M. Tadokoro, H. Hirata, N. Nakano, Z. L. Petrovic, and T. Makabe, "Time resolved optical emission spectroscopy of an inductively coupled plasma in argon and oxygen", Phys. Rev. E **57**, R43–R46 (1998).

[142] M. Tadokoro, A. Itoh, N. Nakano, Z. L. Petrovic, and T. Makabe, "Diagnostics of an inductively coupled plasma in oxygen", IEEE Transactions on Plasma Science **26**, 1724–1732 (1998).

[143] A. Smolyakov, V. Godyak, and A. Duffy, "On nonlinear effects in inductively coupled plasmas", Physics of Plasmas **7**, 4755–4762 (2000).

[144] V. A. Godyak, R. B. Piejak, and B. M. Alexandrovich, "Observation of second harmonic currents in inductively coupled plasmas", Phys. Rev. Lett. **83**, 1610–1612 (1999).

[145] I. M. El-Fayoumi and I. R. Jones, "Measurement of the induced plasma current in a planar coil, low-frequency, rf induction plasma source", Plasma Sources Sci. Technol. **6**, 201 (1997).

[146] M. Tuszewski, "Enhanced radio frequency field penetration in an inductively coupled plasma", Phys. Rev. Lett. **77**, 1286–1289 (1996).

[147] M. Tuszewski, "Inductive electron heating revisited", Phys. Plasmas **4**, 1922–1928 (1997).

[148] J. T. Gudmundsson and M. A. Lieberman, "Model and measurements for a planar inductive oxygen discharge", Plasma Sources Sci. Tech. **7**, 1 (1998).

[149] M. M. Turner, "Collisionless electron heating in an inductively coupled discharge", Phys. Rev. Lett. **71**, 1844–1847 (1993).

[150] M. Abdel-Rahman, V. S.-v. der Gathen, and T. Gans, "Transition phenomena in a radio-frequency inductively coupled plasma", J. Phys. D: Appl. Phys. **40**, 1678 (2007).